Computational Prediction of Stall Aerodynamics and Evaluation of Ground Effect for a Generic Transport Aircraft

Mohamed Sereez

A Thesis submitted in partial fulfillment requirements for the
Degree of Doctor of Philosophy in
Aeronautical Engineering

School of Engineering and Sustainable Development
De Montfort University
United Kingdom
December 2018

Abstract

Flight safety of modern transport aviation depends to a large extent on the skills of the pilot in dealing with manual aircraft control in critical flight situations. According to Boeing's document " Statistical Summary of Commercial Jet Airplane Accidents, Worldwide Operations (1959-2016)" about 89 percent of all fatal accidents in aviation take place due to Loss of Control-In Flight (LOC-I), Controlled Flight into or Toward Terrain (CFIT), and Runway Excursion (RE). The major contribution to flight fatalities is related to LOC-I situations when pilots are unable to handle control of an aircraft during an onset of aerodynamic stall at high angles of attack provoking almost unrecoverable flight conditions. The second contributor to critical flight accidents is related to RE situations during landing and take-off phases of flight. It is now generally accepted that the reduction in flight accidents can be achieved via improved training of line pilots using modern flight simulators, which are now used for regular pilot training in normal flight conditions. Pilot training in extended flight envelope will soon become mandatory following new regulations from FAA, ICAA and EASA. Training of pilots for upset prevention and recovery in LOC-I critical conditions need flight simulators upgraded with aerodynamic models covering extended flight envelope including high angles of attack with separated flow conditions. Flight accidents with RE require improved modeling of aerodynamics in close proximity to the ground considering cross-wind conditions.

Data for aerodynamic models for normal and extended flight conditions are traditionally obtained from wind tunnel tests using different methods such as static, forced oscillation and rotary balance tests. The role of Computational Fluid Dynamics (CFD) methods in generating aerodynamic data for extended flight envelope has a significant potential in improving fidelity of aerodynamics models and reducing the cost of such models. Wind tunnel test results at high angles of attack are sensitive to the level of flow turbulence in the tunnel and aeroelastic vibrations of the aircraft model, while computational simulation predictions are highly sensitive to the selection of turbulence model closing the Unsteady Reynolds Averaged Naiver-Stokes (URANS) equations. This Thesis is mostly focused on computational prediction of static stall hysteresis, ground effect and ice accretion effect on aerodynamics of flight which leads to upset of aircraft in the extended flight envelope. The ultimate motive is to generate reliable aerodynamic data which can be used to develop flight models that can be used to train pilots for loss of control of aircraft in critical flight situations.

For my future kids

Acknowledgments

Firstly, thank you God for giving me this opportunity to complete a PhD in a challenging but definitely an inspiring field.

I would like to massively thank my Fiance Nahu, for being so patient and supportive during these long years. Without her continuous motivation and non-stop support I could not have succeeded to finish this research degree. Thank you for being there at all times.

A big thanks goes to my very close friends Turki and Shaahid who have always been there for me and guided me in life with their wisdom and support. Also, my house mates Mahmoud and Bushra were very helpful and my gratitude goes to them from the bottom of my heart.

I could never thank my parents enough for their continuous support and guidance. They supported me so much during my degree and my masters and believed in me that I can achieve more. Thank you so much for being there whenever I needed.

I owe a great deal of endless thanks to my supervisor Pof. Mikhail Goman. Thank you for being so helpful and teaching me endless techniques to succeed in academics and personal life. In this context, my thanks goes to my additional supervisors Dr. Nikolay and Dr. Xin Kai Li for their guidance and input throughout the time of my degree. Thank you all.

Last but not the least, thank you De Montfort University for giving me the Vice-Chancellor's High flyers Scholarship and funding my PhD during these 3 years.

Contents

1 Introduction **15**
- 1.1 Findings of the Thesis . . . 17
- 1.2 Publications . . . 18

2 Principles of Flight and Fluid Dynamics **20**
- 2.1 Flight Dynamics . . . 20
- 2.2 Fluid Dynamics . . . 25
  - 2.2.1 Navier-Stokes Equations . . . 25
  - 2.2.2 Mathematical Classification of Flows . . . 26
  - 2.2.3 Numerical Components for Solving N-S Equations . . . 27
  - 2.2.4 Characteristics of Numerical Solution Methods . . . 28
  - 2.2.5 Finite Difference Method . . . 29
  - 2.2.6 Finite Element Method . . . 31
  - 2.2.7 Finite Volume Method . . . 31
  - 2.2.8 Application of the Numerical Framework settings to CFD . . . 33
  - 2.2.9 Turbulence Models . . . 33

3 OpenFOAM **40**
- 3.1 Introduction . . . 40
  - 3.1.1 User Control and Interfaces . . . 40
  - 3.1.2 Solvers . . . 40
- 3.2 Numerical Methods . . . 41
  - 3.2.1 Spatial Discretization . . . 42
  - 3.2.2 Temporal Discretization . . . 42
  - 3.2.3 Boundary conditions . . . 43
- 3.3 Validation of OpenFoam for Aerodynamics . . . 44
  - 3.3.1 CFD results for NACA - 0012 airfoil at Re = 6 million against Experimental results . . . 44
  - 3.3.2 CFD results for NACA - 4412 airfoil at Re = 6 million against Experimental results . . . 45
  - 3.3.3 Turbulent Flow past Cylinder at Re = 100,000 . . . 47
- 3.4 Contribution to OpenFOAM . . . 49
  - 3.4.1 transientSimpleFoam - Unsteady flow solver with Adapative Time Stepping . . . 49
  - 3.4.2 transientSimpleDyFoam - Unsteady Large Courant flow solver with Dynamic Mesh Movement . . . 50

3.4.3 hysteresisFoam - incorporates pre-history of pressure 52
3.4.4 GMRES and Bi-Conjugate Stabilized Matrix Solver 53
3.4.5 Modified Baldwin-Lomax model 54
3.4.6 K-Omega SST Vorticity Model 54
3.4.7 Spalart-K-Omega Hybrid model 55
3.4.8 Dynamic Mesh Solver with prescribed α change 55
3.4.9 Need for new/modified implementations 55

4 Aerodynamic Stall Hysteresis 57
4.1 Experimental results 66
4.1.1 NACA 0018 at Low Reynolds Flow conditions 66
4.1.2 Phenomenological bifurcation model of static hysteresis . . . 69
4.1.3 TsAGi-9140 Airfoil at Moderately High Reynolds Flow conditions 72
4.2 Static hysteresis in flow past Hawk Model 73
4.3 Computational Results 75
4.3.1 NACA 0012 at Low Reynolds Flow conditions using Modified Baldwin Lomax turbulence model 76
4.3.2 NACA 0018 at Low Reynolds Flow conditions using Modified BL and S-A turbulence model 79
4.3.3 TsAGi-9140 airfoil at Moderately Higw Reynolds Flow conditions 86
4.4 Concluding Remarks on Static Aerodynamic Hysteresis 90

5 Ice Accretion effect on Aerodynamics of Flight 92
5.1 Analysis of NACA 4412 airfoil with ice accretion using XFOIL and ANSYS Fluent 99
5.2 Analysis of icing in Boeing-737 wing cross-sections using CFD methods 101
5.3 Analysis of 3D Boeing 737 wing with non-symmetric ice distribution 102
5.4 Phenomenological model for ice accretion 104
5.5 Concluding Remarks on Ice Accretion Effect 105

6 Ground Effect Aerodynamcis 106
6.1 NACA 4412 airfoil with Flap in close proximity to ground 111
6.2 Ground Effect Analysis of Common Research Model(CRM-NASA) . 113
6.2.1 CFD simulation of ground effect aerodynamics 114
6.2.2 Airplane lateral-directional dynamics in close proximity to the ground 123

7 Concluding Remarks and Future Work 129
7.1 Summary of Research 129
7.2 Future Work 131
7.3 Contributions 132

8 Appendix **139**
8.1 Source codes that are frequently used in OpenFOAM 139

List of Figures

2.1 Moments and rates [6]. 21
2.2 Co-ordinate systems for flight in a vertical plane [6]. 21
2.3 Lift force coefficient vs. angle of attack (α) [6]. 22
2.4 Block diagram of a control system for flight [7]. 23
2.5 Cartesian grid discretized for finite difference method 1d(top) and 2d(bottom). 29
2.6 Different schemes used in approximations of derivatives. [8] 30
2.7 Typical arrangement of control volume (CV) and nodes in Finite volume Method. [8] 31
2.8 Discretization in finite volume method for a 2D cartesian grid [8] . . 32
2.9 LES/DNS turbulent motion(left) and time-dependent velocity fluctuations(right)[8]. 38

3.1 Control volume [20]. 41
3.2 Control volume in the boundary reprinted from [20]. 43
3.3 OpenFOAM SST model vs. Experimental results for NACA-0012 airfoil at $Re = 6\ million$. 45
3.4 Computational Domain for NACA 4412 airfoil CFD simulation. . . 45
3.5 Blocking and Grid for structured meshing of NACA 4412 airfoil CFD simulation. 46
3.6 Results for NACA 4412 airfoil at $Re = 6million$ compared against experiment from Abott. 46
3.7 Contours of Velocity for NACA 4412 airfoil at $Re = 6million$ top left $\alpha = 0°$, top right $\alpha = 5°$ and bottom $\alpha = 8°$. 47
3.8 Computational setup for flow past cylinder at $Re = 100,000$. 47
3.9 Convergence of force coefficients, URANS, S-A model, PISO $Re = 100,000$. 48
3.10 Streamline visualization of fully developed flow past the cylinder, URANS, S-A model, PISO $Re = 100,000$. 48
3.11 Contours of velocity at $time = 1.2s$ for maximum lift coefficient [left] and $time = 1.25s$ for minimum lift coefficient [right] URANS, S-A model, PISO $Re = 100,000$. 48
3.12 Convergence of lift force for PISO vs. Unsteady SIMPLE algorithm $Re = 100,000$. 49

4.1 Smoke visualization of static hysteresis for Lisamann airfoil presented in [25]. 58

4.2 PIV visualization of $\alpha = 14°$ return branch from [26]. 58
4.3 Wind tunnel test results for NACA 0018 airfoil in static hysteresis reported in [27]. 59
4.4 Static hysteresis for NACA 0015 wing presented in [28]. 59
4.5 Shrinking of hysteresis loop due to wind tunnel noise presented in [30]. 60
4.6 CFD simulation of static hysteresis past NACA 0012 airfoil from [4]. 60
4.7 Computational simulation of static hysteresis in the transonic flow regime from [31]. 61
4.8 Semi empirical prediction model for static hysteresis from [32]. . . . 62
4.9 Dynamic Hysteresis loops in flow past CRM aircraft model from [33]. 63
4.10 Low order modelling of dynamic hysteresis from [34]. 63
4.11 Visualization of results of dynamic hysteresis from [34]. 64
4.12 Flapping wing aerodynamics predicted by Lattice Boltzmann methods from [41]. 64
4.13 Normal force coefficient from [42]. 65
4.14 Pitching moment coefficient from [42]. 66
4.15 Straight wing with NACA-0018 airfoil fitted in the low-turbulence TsAGI T-124 wind tunnel (left plot), Force balancing scheme for measuring aerodynamic loads (right plot). 67
4.16 Dependence of the NACA0018 wing lift coefficient on angle of attack from static tests and continuous sweep motion (left), the angle of attack, lift and pitching moment coefficients time dependencies in continuous sweep motion (right). $V = 40m/s, Re = 700,000$. 67
4.17 Dynamic loops in the NACA0018 wing lift coefficient during periodic changes of angle of attack with different amplitudes and frequencies: $f = 0.5Hz$ on the left, $f = 2.0Hz$ on the right. $V = 40m/s, Re = 700,000$. 68
4.18 Bifurcation model of static hysteresis with two stable branches separated by unstable branch. 70
4.19 Comparison of experimental results from different sources for $Re = 300k$. 71
4.20 The TsAGI-9140 airfoil geometry. [46] 72
4.21 Considered leading edge modifications for the TsAGI-9140 airfoil. [46] 72
4.22 The lift coefficient for the clean and modified TsAGI-9140 airfoils ($M = 0.15$, $Re \approx 5 \times 10^6$) [46]. 73
4.23 Rig configuration, 2DOF - approx Hawk model. [47] 74
4.24 Static hysteresis in lift force measured in rig arm pitch angle for Hawk Model. [47] 74
4.25 Static hysteresis in lift force measured in elevator deflection angle for Hawk Model.[47] 75
4.26 Static hysteresis in onset of aerodynamic asymmetry in roll and yaw for Hawk Model.[47] 75

4.27 NACA-0012 2D airfoil at Re = 1 million, CFD and experimental results. . . . 77
4.28 NACA-0012 2D airfoil at Re = 6 million, CFD and experimental results. . . . 77
4.29 Convergence at $\alpha = 5$ degrees(top) and oscillation amplitudes for low angles of attack - Baldwin-Lomax original model and modified BL model(bottom). . . . 78
4.30 Contours of velocity at $\alpha = 15$ degrees for original(top) and modified version(bottom)of Baldwin-Lomax model. . . . 79
4.31 Computational domain for the 2-D simulation. . . . 80
4.32 Close up view of grid for NACA 0018 airfoil. . . . 81
4.33 Static Hysteresis Loops - CFD and Experimental - NACA 0018 - 2D , Re = 700,000. . . . 82
4.34 Flow field images of NACA0018 at $Re = 0.7 \times 10^6$ and $\alpha = 18°$, top left- modified BL model, top right - SA model and bottom plot shows SA model with lower Turbulent Schmidt number 83
4.35 flow stream patterns for NACA 18 at Re = 700,000 at multiple solutions using Baldwin-Lomax model. . . . 84
4.36 Streamlines of flow for NACA 0018 at $\alpha = 20° = 20$ degrees DES-SA Vs. Modified Baldwin-Lomax model. . . . 85
4.37 Mesh generated for clean TsAGi-9140 airfoil. . . . 87
4.38 Mesh generated for 1.5% LE modified TsAGi-9140 airfoil. . . . 87
4.39 Mesh generated for 2% LE modified TsAGi-9140 airfoil. . . . 87
4.40 Experiment and CFD results for clean TsAGi-9140 airfoil. . . . 88
4.41 CFD results for TsAGi-9140 airfoil at $Re = 5 \times 10^6$. . . . 89
4.42 Experiment and CFD results for 2 percent modified TsAGi-9140 airfoil at $Re = 5 \times 10^6$. . . . 89

5.1 Shear layer and vortex shedding distribution for a horn shape ice deposited airfoil from [56]. . . . 93
5.2 CFD and experimental data for horn shape iced airfoil from [56]. . . 94
5.3 Wind tunnel results for NASA GTM model with and without ice from [58]. . . . 94
5.4 Rime Ice shapes for Boeing 737 wing root airfoil [61]. . . . 95
5.5 Grids generated for rime ice shapes for Boeing 737 wing root airfoil [61]. . . . 96
5.6 Results obtained for rime Ice shapes for Boeing 737 wing root airfoil [61] 96
5.7 Grid generated for 3d iced wing [61]. . . . 97
5.8 Aerodynamic coefficients obtained for clean and iced 3D wing [61]. 97
5.9 visualization of flow streamlines at y = 3.6526m and $\alpha = 11$ degrees [61]. . . . 98
5.10 Icing shape 1 (top) and icing shape 2(bottom) installed on NACA 4412 airfoil. . . . 99
5.11 XFoil results for NACA 4412 airfoil in clean and iced condition. . . 100

5.12 Fluent vs. XFoil results for NACA 4412 airfoil in clean and iced condition. 101
5.13 Superimposed Airfoil cross sections of Boeing 737 wing. 101
5.14 Horn ice shape installed on Boeing 737 root airfoil 102
5.15 Results for clean and iced conditions with horn ice shape for $Re = 15 \times 10^6$ and $M = 0.3$ using Shear Stress Transport(SST) model. . 102
5.16 B-737 3D clean wing(orange) and iced wing (green). 103
5.17 cross section view of the generated grid for the B737 wing. 103
5.18 CFD results for the 3D wings in clean and iced conditions at $Re = 15 \times 10^6$ and $M = 0.3$ using Shear Stress Transport(SST) model. . . 104
5.19 Phenomenological modelling of ice accretion effect on the lift coefficient. 104

6.1 Schematic for double element racing car wing in ground effect from [65]. 107
6.2 C_L results for double element wing in ground effect from [65]. . . . 107
6.3 Instantaneous vorticity contours for a flapping insect wing from [39]. 109
6.4 Compressible ground effect aerodynamics from [68]. 110
6.5 *Heaving pitching foil in ground effect from [69].* 110
6.6 Generated grid for simulations of static and dynamic hysteresis in ground effect. 111
6.7 Lift coefficient C_L against α at $Re = 6 \times 10^6$ for NACA 4412 airfoil in Ground Effect. 112
6.8 Visualization of streamlines superimposed on velocity (left) and pressure(right) contours for NACA 4412 airfoil. 112
6.9 Dynamic loops at reduced frequency of $k = 0.2$ for lift coefficient C_L against α at $Re = 6 \times 10^6$ NACA 4412 airfoil w/o flaps in Ground Effect. 113
6.10 Full configuration of the Common Research Model (CRM). 114
6.11 Slice view for the grids far away from ground, front top and side view. 115
6.12 Slice view of symmetry plane of the grid for $h/c = 1$, close proximity to ground. 116
6.13 Generated meshes and flight settings at different α and ϕ for $h = 0.5\bar{c}$. 116
6.14 Streamlines showing vortices's behind the aircraft for no ground effect, $\alpha = 0^\circ$ and $\phi = 0^\circ$. 118
6.15 Pressure contours showing vortices's behind the aircraft for $h = 1\bar{c}$ $\alpha = 0^\circ$ and $\phi = 0^\circ$. 118
6.16 Pressure distribution on CRM model and inserted plane behind aircraft at $h = 0.5\bar{c}$, $\alpha = 8^\circ$ and $\phi = 4^\circ$. 119
6.17 streamlines imposed on pressure contours for CRM model and inserted plane behind aircraft at $h = 0.5\bar{c}$, $\alpha = 8^\circ$ and $\phi = 8^\circ$. . . . 119
6.18 streamlines imposed on pressure contours for CRM model and inserted plane behind aircraft at $h = 0.5\bar{c}$, $\alpha = 8^\circ$ and $\phi = 12^\circ$. . . . 119
6.19 Effect of bank angle on aerodynamic coefficients C_L, C_D, C_m, C_l, C_n at $h = 0.5\bar{c}$, $\alpha = 8^\circ$. 120

6.20 Isometric wireframe view of the surface Grid F11-GTM model. . . . 122
6.21 Scan plane cut through volume mesh for F11-GTM model. 122
6.22 Simulation results for lift coefficient, F11-GTM model. 122
6.23 Simulation results for Pitching moment, F11-GTM model. 123
6.24 Root-loci of eigenvalues of the longitudinal and lateral-directional dynamics modes at different altitudes above the runway $h = 4.0\bar{c}$, $h = 2.5\bar{c}$ and $h = 1.0\bar{c}$, top plot - $\alpha = 3^\circ$ and bottom plot - $\alpha = 8^\circ$. . 125
6.25 Airplane responses to doublet aileron control input $\delta_a = \pm 25^0$ at different altitudes above the runway obtained in 6-DOF simulation. 126
6.26 Airplane responses to doublet rudder control input $\delta_r = \pm 35^0$ at different altitudes above the runway obtained in 6-DOF simulation. 126
6.27 Trim control inputs required in landing approach with nonzero sideslip and bank angles ($\alpha = 8^\circ$, $\beta = 10^\circ$, $\phi = 4^\circ$). 127

Nomenclature

Ma	=	Mach number
p	=	static pressure
q	=	dynamic pressure
Re	=	Reynolds number
S	=	strain rate
t	=	physical time
α	=	angle of attack
β	=	side slip angle
Φ	=	bank angle
Γ	=	diffusion coefficient
ν	=	kinematic viscosity
μ	=	dynamic viscosity
μ_t	=	turbulent viscosity
ν_t	=	turbulent viscosity (alternative)
$\hat{v}_t$	=	modified Turbulent viscosity
σ	=	plain stress
τ	=	shear stress
k_L	=	laminar Kinetic Energy
k	=	turbulent Kinetic Energy
ϵ	=	turbulent Dissipation rate of k
ω	=	specific Dissipation rate of k
Ω	=	vorticity
$\|\Omega\|$	=	vorticity Magnitude
$\|S\|$	=	strain rate Magnitude
L, D, M	=	lift, drag and pitching moment
C_L, C_D, C_M	=	lift, drag and pitching moment coefficient
C_N, C_X, C_Z	=	normal, axial and Z moment coefficient
C_l, C_y	=	roll and yaw moment coefficient
CoM, CoG, CoP	=	center of moment, gravity and pressure
C_{ref}, S_{ref}	=	reference chord length and reference area
C_P	=	pressure coefficient
C_f	=	skin friction coefficient

Acronyms

AR	=	Aspect Ratio
BL	=	Baldwin-Lomax
CFD	=	Computational Fluid Dynamics
CRM	=	Common Research Model
EOM	=	Equations of Motion
GTM	=	Generic Transport Model
LE, TE	=	Leading and Trailing Edge
NS	=	Navier-Stokes
ODE	=	Ordinary Differential Equation
$OpenFOAM$	=	Open Field Operations and Manipulations
PDE	=	Partial Differential Equation
$RANS$	=	Reynolds Averaged Navier-Stokes
SA	=	Spalart-Allmaras
SST	=	Shear Stress Transport
$URANS$	=	Unsteady Reynolds Averaged Navier-Stokes

Chapter 1

Introduction

Loss of Control in Flight (LOC-I) is the main cause of flight accidents according to statistics published by Boeing [1]. These accidents are happening due to airplane upsets with onset of separated flow conditions, deterioration of airplane stability and control characteristics in the extended flight envelope. Another extreme of the flight envelope is take-off and landing conditions. Abnormal Runway Contact (ARC) and Runway Excursion (RE) holds the second place for flight fatalities [1]. The later falls into category of Departure and Landing flight accidents. Approach and Landing Accident Reduction (ALAR) is the primary goal of Flight Safety Foundation (FSF) [2].

The current pilot training does not include experience of flying in the critical flight regime with upset of aircraft. Pilot training for the extended flight envelope and LOC-I situations is challenging using aircraft in flight. It is now generally accepted that flight simulators can be used instead of conventional methods to train pilots for the critical flight regime. However, it is also noted that appropriate mathematical models representing aerodynamic loads and moments in stall conditions, ice accretion, and the close proximity to the ground which may lead to loss of control in flight are currently not incorporated in pilot training using flight simulators. The available data from various wind tunnel tests need critical analysis and calibration for a full scale aircraft at cruise conditions ($Re \approx 50 \times 10^6$) allowing adequate aerodynamic modelling in the extended flight envelope. For this purpose complementary use of Computational Fluid Dynamics (CFD) methods is very important for creating reliable aerodynamic models for flight simulation [3].

The prediction of aerodynamics associated with aerodynamic stall hysteresis, ground effect and other complicated phenomena is extremely sensitive to various factors in both experiments and computational simulations. CFD simulations based on the Reynolds Averaged Navier-Stokes (RANS) equations itself is subject to various factors such as the type of solver, numerical approximations, turbulence models, ability to remember prehistory and quality of the grid that is being used for the simulation. These factors influence the capability to predict aerodynamic behavior of an aircraft in the extended flight envelope. In other words, the current CFD methods need validation and development in order to be a more reliable candidate to be used to generate data for flight simulators which can then be used to train pilots to recover from hazardous situations. The data generated using

improved CFD models can also be used to alter the design process of aircraft enabling ultra-resilient vehicles to be built. Analysis of the challenges in CFD simulations for complex flight phenomena such as stall hysteresis, ground effect and ice accretion are discussed as follows.

Static aerodynamic hysteresis was mostly investigated in wind tunnel tests at moderately low Reynolds number flow conditions. To the author's best knowledge, there is only one paper [4] in which static hysteresis was investigated using CFD simulations. The capture of the lower branch of static hysteresis (with fully separated flow conditions and much lower lift coefficient, C_L) loop is very sensitive to the choice of the turbulence model. The turbulence model defines and estimates how fast the turbulent vortices are produced, diffused and destroyed. The coefficients or constants to define these parameters in most of the turbulence models are believed to be well tuned in the pre-stall or attached flow region. Therefore, the accuracy of computational simulation in capturing static aerodynamic hysteresis loops with fully separated and bistable flow structures is negatively affected. In this Thesis, a major importance was given to the capture of static hysteresis for two dimensional airfoils at moderately low and high Reynolds numbers. Flow past a NACA 0018 airfoil was simulated at $Re = 300,000$ and $Re = 700,000$ with a numerical setup that allowed the pre-history of the flow field. The NACA 0018 airfoil was simulated with various turbulence models and the results are presented and discussed. Apart from the NACA 0018 airfoil, the TsAGI-9140 airfoil was tested at moderately high Reynolds number of $Re = 5 \times 10^6$ and static aerodynamic hysteresis was observed for the leading edge modified version of the airfoil. Also, to improve the prediction of static hysteresis, slight or major modifications of turbulence models are carried out as a work of this Thesis which allowed improved predictions of the lower branch of aerodynamic hysteresis. The boundary layer setup and numerical framework including time step size and order of accuracy in time marching is also investigated along with the analysis of dependency of static hysteresis simulations on various other factors such as the Reynolds number and shape of the airfoil.

The investigation of ice accretion effect on degradation of the aerodynamic performance was carried out using airfoils of Boeing 737 aircraft. The changes in the stall angle and reduction of lift slope was analyzed for the root, midspan and tip airfoil of the B737 wing. Furthermore, a 3 dimensional wing body made up of B737 airfoils was investigated with one wing having ice shape and the other wing in the clean condition. The resulting aerodynamic coefficients of lift, drag and pitching moment were analyzed using the ANSYS Fluent code. Difficulties also arise in simulations for airfoils, wings or full configuration aircraft in icing conditions. The main challenge being the grid generation techniques that has to be employed, as structured grids are hard to generate for rough icing shapes (horn, glaze, etc). Therefore unstructured grids with triangles and tetrahedral elements are preferred, but this causes an increase in the number of elements in the grid which leads to a large amount of time for solving a single simulation. It is also noted that a steady state simulation cannot be used even at low angles of attack for airfoils with ice accretion as the ice accretion leads to much earlier stall of the

airfoil making an unsteady simulation a more suitable choice.

In investigating ground effect aerodynamics a NACA 4412 airfoil in close proximity to the ground was used with and without flap to extract the coefficients of lift, drag and moments. The conducted observation shows that as the airfoil approaches the ground runway, the lift force increases rapidly and the drag force reduces significantly. However, a two dimensional analysis does not show the changes in the stability of aircraft in close proximity to the ground. Therefore the Common Research Model (CRM) was simulated at various height/chord ratios from the ground with different flight attitudes (bank, pitch and yaw). The resulting loads and moments were then analyzed using flight dynamic methods to yield the longitudinal and lateral stability parameters. The investigation shows that at close proximities to the ground the aircraft may change the modes of motion to form an unstable roll-spiral mode, provoking an unrecoverable flight condition. In investigating ground effect using computational simulations, the main challenges are the grid generation methods and simulation stability. Since the runway needs a boundary layer which will be moving and the aircraft is in such close proximity to the ground/runway various flight attitudes such as banking or pitching are constrained to a limited range. Even with the generation of the correct grids, the simulation is rather unstable due to large unsteady tip vortices that are generated downstream of the aircraft. Therefore a steady state simulation is more preferable to initiate the simulation. Once the simulation has converged in steady state, an unsteady time accurate solution can be initialized from the steady state solution. Various other challenges also arise as there is limited experimental and computational data to verify the simulation results. Also, when the aircraft model is landing in strong cross-winds, the boundary conditions are hard to implement in CFD methods.

The simulations in this Thesis is carried out with the open source CFD code OpenFOAM[5] (Open Field Operations and Manipulation). The code is written in C++ object oriented language. The benefit of using this code is that it comes with various test cases, turbulence models, solvers and parallel computing capabilities. OpenFOAM also lets the user modify their codes or write codes from scratch which was rather helpful for the work in this Thesis.

1.1 Findings of the Thesis

1. Aerodynamic Static Stall hysteresis can be captured with CFD simulations in OpenFOAM using the Spalart-Allmaras (SA) turbulence model. The results can be improved in terms of hysteresis loop's depth and width by modifying the Turbulent Prandtl/Schmidt number. Turbulent Schmidt number Sc_t, controls the diffusion rate of turbulence which then helps in the mixing of the flow thus enabling a better prediction of turbulent characteristics of separated flow conditions with large amplitude oscillations in the aerodynamic forces.

2. Aerodynamic Static Stall hysteresis is extremely sensitive to level of turbu-

lence, noise and method of changing the angle of attack for both CFD and experimental tests. Hence, these factors need to be carefully adjusted and well maintained to make results consistent. The simulations where angle of attack, α, was changed my modifying the grid, seemed to be more sensitive as the boundary characteristics such as $y+$ of the grid changed. Furthermore, the mapping of the flow field from the previous angle of attack to the newly transformed grid was not exactly the same as there are some faulty interpretations in OpenFOAM thus effecting the hysteresis loop results.

3. Two different phenomenological models were presented in Chapter 4 and 5, that can capture the effect of static hysteresis and ice accretion. The models are derived from the Goman-Khrabrov (G-K) model, and modified for each case. The data for constructing these models were extracted mainly from the CFD results presented in this thesis and other experimental/wind tunnel results.

4. Ice accretion analysis on airfoils of Boeing 737 were investigated and showed a decrease of the lift curve slope and earlier stall. Rime ice shape caused most degradation of aerodynamic performance for all the airfoils. Furthermore, analysis of ice accretion effect on 3D wing of Boeing 737 were investigated and the changes in aerodynamic coefficients are presented in Chapter 5.

5. Ground effect in flow past the NASA Common Research model shows lateral-directional modes of motion are significantly transformed via merging the roll-subsidence and spiral eigenvalues, which forms the second oscillatory roll-spiral mode with potential to affect the pilot handling qualities in landing with cross wind conditions.

This Thesis includes seven chapters. The Introduction along with the project objectives are given in Chapter 1. Chapter 2 presents basic principles of the theory of fluid and flight dynamics. The following Chapter 3 contains information about the free CFD software OpenFOAM, which was widely used in the project. This Chapter additionally includes some validation results for CFD simulations. The major results in the prediction of the aerodynamic static hysteresis are presented in Chapter 4. Chapter 5 is dedicated to the ice accretion problem with predictions of deterioration of the aerodynamic characteristics due to geometrical changes generated by ice accretion. The ground effect on airplane aerodynamics in close proximity to the ground is investigated in Chapter 6. A clear understanding of this effect is important for adequate flight simulation during take-off and landing. The final Chapter 7 highlights conclusions of the work and also gives a scope for future research activities.

1.2 Publications

During the work of the thesis the following papers were published:

1. M.Sereez and N.B.Abramov and M.G.Goman and A. Khrabrov, "Computational Simulation of Stall Aerodynamics at Low Reynolds number", Applied Aerodynamics Conference, July 2016, Royal Aeronautical Society, UK.

   The related results and work on static hysteresis is presented in Chapter 4 of this Thesis.

2. M.Sereez and N.B.Abramov and M.G.Goman, "Computational Ground Effect Aerodynamics and Airplane Stability Analysis During Take-off and Landing", 7th European Conference for Aeronautics and Space sciences, July 2017, EUCASS.

3. M.Sereez and N.B.Abramov and M.G.Goman, "Impact of Ground Effect on Airplane Lateral Directional Stability during Take-Off and Landing", Open Journal of Fluid Dynamics, March 2018, Vol 8, Issue 1, Pages 1-14

   The related results and work on Ground Effect for the two papers listed above (2 and 3), is presented in Chapter 6 of this Thesis.

Chapter 2

Principles of Flight and Fluid Dynamics

In order to understand how to apply fluid dynamics simulation results in flight dynamics problems a detailed analysis and understanding of both areas are important. Both areas deal with solving of various types of differential equations, either ODE or PDE. There are some common issues in interpretation of their solutions, for example the concept of steady states and convergence to these steady state solutions can be treated in general terms of stability theory. These similarities allow consideration of bistable flow separation structures in stall conditions in a simple phenomenological form based on ODE. In this chapter the principles of flight dynamics and fluid dynamics methods will be briefly presented and discussed.

2.1 Flight Dynamics

In very simple terms flight dynamics involves using the relationships of the Newton's laws ($F = m \cdot a$ and $M = I \cdot \alpha$) to analyze the performance, stability and control parameters of a flight [6]. It also lies in close context with aerodynamic principles of flight. The body axis system is usually originated in the center of gravity (CG) point of the aircraft with x pointing to nose of the aircraft, y pointing away from the starboard (right side) and z pointing downward from the center of gravity. The motions of the aircraft then can be denoted with respect to the body axes system. Motion around the x axis of the aircraft will be the rolling motion expressed by parameter L and roll rate denoted by P. Motion around the y axis of the aircraft will be the pitching motion expressed by the parameter M and pitch rate denoted by Q. Finally the motion around z axis of the aircraft will be the yawing motion expressed by parameter n and yaw rate denoted by R. To summarize the moments are Roll (L), Pitch (M) and Yaw (N) and the rates o rotation are Roll rate (P), Pitch rate (Q) and Yaw rate (R) as shown in the Fig. 2.1. The coefficients of moments can then be expressed using non dimensionality as (C_l, C_M and C_n).

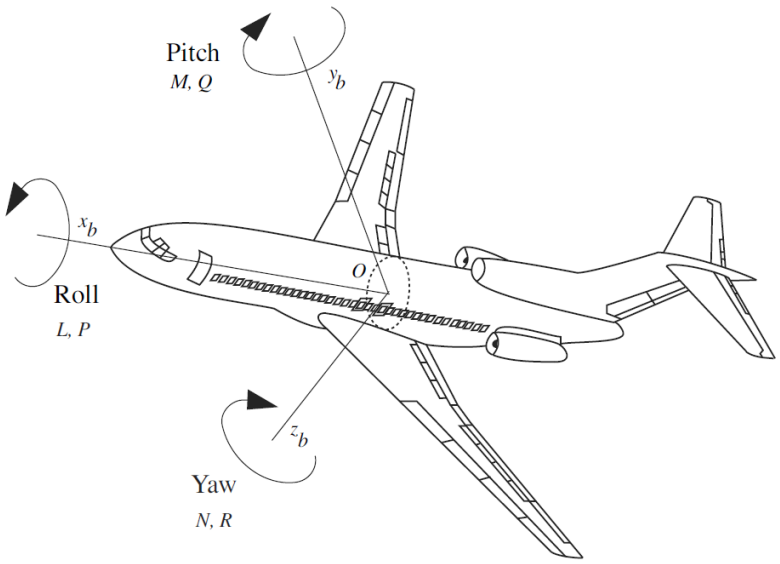

Fig. 2.1: Moments and rates [6].

The co-ordinate systems for flight in a vertical plane are shown in Fig. 2.2. It is useful to indicate important attitude information such as angle of attack (α) and flight path angle(Γ) with respect to the velocity vector V of the flight.

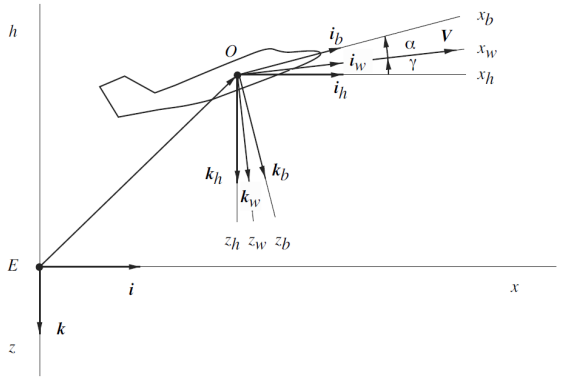

Fig. 2.2: Co-ordinate systems for flight in a vertical plane [6].

The aerodynamics of flight is particularly important to be well understood in order to realize the accuracy of fluid dynamics in evaluating flight dynamics. To achieve this objective one must understand the basics of aerodynamics such as lift, drag and moments and the equations to estimate these parameters.

The lift force of an aerodynamic body is given by:

$$L = \frac{1}{2} C_L \rho S_{ref} V^2 \tag{2.1}$$

where L is Lift force, C_L is lift force coefficient, ρ is free stream density, S_{ref} is the reference wing plan form area and V is velocity of flight relative to atmospheric conditions.

The drag force of an aerodynamic body is given by:

$$D = \frac{1}{2} C_D \rho S_{ref} V^2 \tag{2.2}$$

where D is the Drag force and C_D is the drag force coefficient.

It can also be noted that C_L, C_D are functions of α, Ma and Re. Where Ma is the Mach number, Re is the Reynolds number and α is the angle of attack in degrees.

The Mach number is usually expressed as $M = \frac{V}{a}$ and $Re = \frac{\rho V l}{\mu}$ where $a =$ speed of sound, $l =$ reference length of the aircraft and μ is the dynamic viscosity of air.

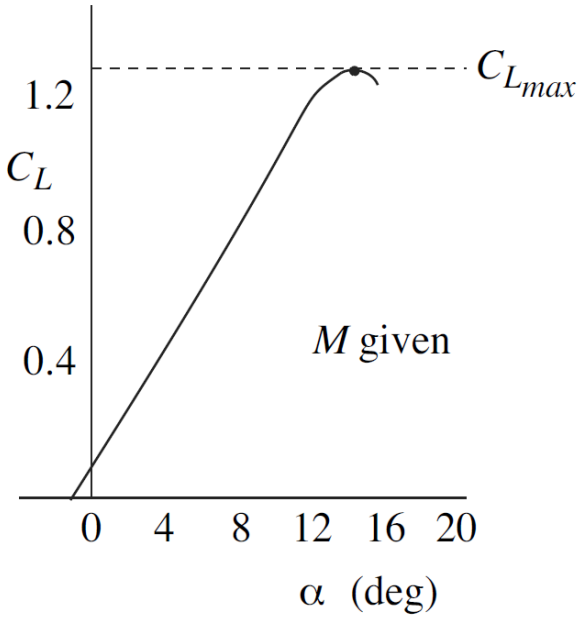

Fig. 2.3: Lift force coefficient vs. angle of attack (α) [6].

Fig. 2.3 shows a typical lift coefficient C_L vs. angle of attack plot for an aircraft. There is a linear increase in lift force as the angle of attack increases but after reaching the maximum lift coefficient $C_{L_{max}}$ the lift coefficient value drops which is often referred to as stall of an aircraft.

The lift to drag force ratio is also an important parameter in evaluating aerodynamic performance as the fuel usage and cost of flying reduces with the increase of this ratio and is expressed as:

$$E = \frac{L}{D} = \frac{C_L}{C_D} \tag{2.3}$$

Like any other control system for an Aircraft the output can be controlled through a block system with appropriate procedures. A simple input output block diagram appropriate for describing flight dynamics is shown in Fig. 2.4.

Fig. 2.4: Block diagram of a control system for flight [7].

In Fig. 2.4, X can be input state such as position $= (x, y, z)$, velocity $= (u, v, w)$, attitude (θ, ϕ, γ) and angular velocities as (p, q, r). Thus;

$$X = [x, y, z, u, v, w, \theta, \phi, \gamma, p, q, r] \tag{2.4}$$

And δ expressed in terms of e - elevator, t - throttle, a - aileron, r - rudder, is a function of:

$$\delta = [\delta_e, \delta_t, \delta_a, \delta_r] \tag{2.5}$$

One can now express the dynamic equations using the previous denotions. Linear acceleration can be taken as the sum of aerodynamic, gravitational and gyroscopic forces.

$$m\dot{u} = X - mg \cdot sin(\theta) + m(rv - qw) \tag{2.6}$$

$$m\dot{v} = Y + mg \cdot sin(\phi)cos(\theta) + m(pw - ru) \tag{2.7}$$

$$m\dot{w} = Z + mg \cdot cos(\phi)cos(\theta) + m(qu - pv) \tag{2.8}$$

where:

$$X = C_x \frac{\rho V^2}{2} S \tag{2.9}$$

$$Y = C_y \frac{\rho V^2}{2} S \tag{2.10}$$

$$Z = C_z \frac{\rho V^2}{2} S \tag{2.11}$$

and:

$$I_{xx}\dot{p} = L + (I_{yy} - I_{zz})qr \tag{2.12}$$

$$I_{yy}\dot{q} = M + (I_{zz} - I_{xx})pr \tag{2.13}$$

$$I_{zz}\dot{r} = N + (I_{xx} - I_{yy})pq \tag{2.14}$$

where: I_{xx}, I_{yy} and I_{zz} are moment of inertia about principal x, y and z axes respectively.

and:

$$L = C_l \frac{\rho V^2}{2} S_{ref} b \tag{2.15}$$

$$M = C_m \frac{\rho V^2}{2} S_{ref} \bar{c} \tag{2.16}$$

$$N = C_n \frac{\rho V^2}{2} S_{ref} b \tag{2.17}$$

where: b is wing span, $\bar{c}$ is wing reference chord and S_{ref} is reference wing area. The kinematic relation between position and velocity can be expressed as:

$$\begin{bmatrix} \dot{x} \\ \dot{y} \\ \dot{z} \end{bmatrix} = T^{B \to I}(\phi, \theta, \gamma) \begin{bmatrix} u \\ v \\ w \end{bmatrix}$$

where $T^{B \to I}(\phi, \theta, \gamma)$ is the transformation matrix from the body axis frame $O_b X_b Y_b Z_b$ to the Earth inertia axis frame $O_E X_E Y_E Z_E$. We can now express the relationship between attitude and angular velocity.

$$\dot{\phi} = p + qsin(\phi)tan(\theta) + rcos(\phi)tan(\theta) \tag{2.18}$$

$$\dot{\Theta} = qcos(\phi) - rsin(\phi) \tag{2.19}$$

$$\dot{\gamma} = q\frac{sin(\phi)}{cos(\theta)} + r\frac{cos(\phi)}{cos(\theta)} \tag{2.20}$$

The lateral and longitudinal system can be expressed as:

Longitudinal state and control vectors

$$X_{long} = \begin{bmatrix} u \\ w \\ \theta \\ q \end{bmatrix}$$

$$\delta_{long} = \begin{bmatrix} \delta_e \\ \delta_t \end{bmatrix}$$

Lateral and directional state and control vectors

$$X_{lat} = \begin{bmatrix} v \\ \phi \\ p \\ r \end{bmatrix}$$

$$\delta_{lat} = \begin{bmatrix} \delta_a \\ \delta_r \end{bmatrix}$$

The control of flight is a much more complicated process than to be said as linear. Non - linear models describe the behavior of flight more appropriately but is outside the context of this Thesis and the interested readers are referred to [6, 7] and other books and papers published in the public domain.

In order to estimate the dynamics of flight using computational tools study of fluid dynamics is relatively important. In the following section a brief theory of fluid dynamics that lies in close context with the work done in this research degree is presented.

2.2 Fluid Dynamics

In continuum mechanics, the equations that define the flow characteristics are derived from laws established with relation to the conservation of the flow. They are:

1. The conservation of mass,
2. The conservation of momentum,
3. The conservation of energy.

Conservation of any flow quantity is in close relation to the **flux** across boundaries of arbitary volumes. Flux is usually defined in two parts i.e. the convective part and the molecular diffusive part. Conservation laws automatically leads us to define the flow field in a number of control volumes which are finite in their nature. Such an explanation leads to the formulation of **finite control volume**.

To well define a finite control volume fixed in space one can use the series of notations as given below:
1. a closed surface $\partial\Omega$,
2. a surface element on the closed surface dS,
3. outward pointing unit vector, $\vec{n}$.

The fluid flow past these finite volumes are most well described by the Navier-Stokes equations.

2.2.1 Navier-Stokes Equations

Navier-Stokes equations govern the fluid flow and are the basis on which fluid dynamics is developed on. The equations are non-linear in their nature.

NS equations governing **incompressible** fluid flow (with approximation of no changes in temperature) are the continuity and momentum equation listed below:

$$\nabla \cdot \mathbf{u} = 0 \tag{2.21}$$

$$\frac{\partial \mathbf{u}}{\partial t} + \nabla(\mathbf{uu}) - \nu\nabla^2\mathbf{u} = -\frac{\nabla \mathbf{p}}{\rho} \tag{2.22}$$

Fluids undergo deformation even with application of the tiniest external forces. This is the main cause of fluid flow. The forces that usually drive fluid flow are differences in pressure, gravity, shear, rotation and tension in surfaces. The external forces that are behind fluid flow can be differentiated into two categories. They are; 1) Surface forces and 2) Body forces. [8]

There are various factors that affect the flow. This mainly includes the speed of the flow, the viscosity, density, temperature and surface tension. Depending on the alteration of these factors the flow can be classified into various categories.

1. Incompressible flow When speed of the flow characterized in Mach number is low enough (M $\leq$ 0.3) the flow may be considered as incompressible. In such cases, the fluid density is assumed to be constant. This applies for both liquids and gases.

2. Inviscid flow Inviscid flow is sometimes referred to as Euler's flow. The flow occurs far from a solid surface and the effects of viscosity are small and negligible. Therefore the Navier-Stokes equations reduces to the Euler equations where the viscous effects are not considered. Euler equations are convenient when analyzing the compressible flow at high Reynolds numbers. This is because at high velocities the Reynolds number is very high and the viscous flow takes place only at a very small region just close to the solid walls.

3. Potential Flow When the flow is both inviscid and the flow does not rotate then the flow is called potential flow.

4. Stokes Flow Stokes flow or creeping flow happens when the velocity of the fluid is very small and the viscosity of the flow is very high. This in turn means that the Reynolds number of the flow is very small. The terms that appear for convection in NS equations can be neglected and the flow is dominated by other aspects such as pressure, viscosity and body forces.

5. Boussinesq Approximation This classification of flow involves approximating that the density is constant for unsteady and convectional terms and only varies in the gravitational term.

6. Boundary Layer Approximation Flows that have a defined direction with no reverse flow and main influences on flow characteristics are from upstream.

2.2.2 Mathematical Classification of Flows

In the previous section we distinguished different categories into which the flow can be characterized depending on the viscosity, density, pressure, etc. The prior classification is based on the physics of the flow. It is also possible to classify flows mathematically depending on the nature of equations that need to be solved. The main three categories are Hyperbolic, Parabolic and Elliptic flow.

The difference in these PDE's are best understood by taking some sample example problems and considering their discriminants [9].

1. Hyperbolic Flows

The one dimensional wave equation is a hyperbolic PDE because it's discriminant is one and known to have non-smooth and discontinuous solutions.

$$U_{xx} - U_{tt} = 0 \tag{2.23}$$

2. Parabolic Flows

Diffusion(also referred to as heat) equation is a parabolic PDE because its discriminant is zero.

$$U_t - U_{xx} = 0 \tag{2.24}$$

3. Elliptic Flows

Laplace equation is an elliptic PDE because its discriminant is negative:

$$U_{xx} + U_{yy} = 0 \tag{2.25}$$

The discriminant of an equation is $B^2 - 4ac$ and determines the number of real solutions [10].

2.2.3 Numerical Components for Solving N-S Equations

Mathematical Model

The basics of Fluid Dynamics evolves with the type of solving partial differential equations that define the type of flow. These equations vary depending on the classification of flow and the type of flow. This is often referred to as the starting point to solve Navier-Stokes equations.

Discretization Methods

The methods of approximating the differential equations by a system of algebraic equations are called discretization methods. The most famous of these methods are **finite difference method, finite element method and finite volume method**. Finite Difference (FDM) involves using Taylor - series expansion to approximate the differential equations by approximating them with difference equations. Finite Element method (FEM) involves using weighted residuals functions to approximate the integrals and the Finite Volume method (FVM) uses surface integrals to approximate the differential equations of navier stokes equations.

From all the above mentioned three methods finite difference method is the simplest method. Finite element is known as the most stable and most famous amongst mathematicians while finite volume method is more commonly used in commercial and open source fluid dynamics softwares. More details on Finite Volume Method (as OpenFOAM uses FVM) will be given in a later section of the Thesis.

Cordinate System

The equations defining fluid flow can by written in different forms. They include cylindrical, cartesian, spherical and curvil-linear orthogonal or non - orthogonal co-ordinate systems. The coordinate systems might be moving or stationary.

Numerical Grid

A grid defines the locations at which variables will be calculated. Different types of grids exists such as structured or unstructured grids. Structured grids are regular in their formation such that they can be numerically identified with indices (i,j,k) in a consistent manner. They are usually made up of quadilateral elements or hexahedral elements in 3D space.Unstructured grids cannot be numbered consistently and are usually made of up elements such as triangles, polygons, tetrahedrals, prisms or pyramids.

Finite Approximations

Depending on the chosen method of discretization i.e. FD, FE or FV finite approximations are then made for the differential equations. For finite difference, grid points are used to estimate the derivatives. In the finite element method

shape functions are used while in the finite volume method surface and volume integrals are used.

Solution Method

The methods for marching in time (unsteady cases), and solving the non-linear equations by linearizing them into linear systems is the solution method. One has to chose appropriate methods depending on type of simulations and classification of the flow into a distinctive mathematical model.

Criterion for Convergence

At last one has to specify certain levels in which the equations are believed to be sufficiently solved i.e. residuals of all equations (continuity, momentum and turbulence) drop to this level.

2.2.4 Characteristics of Numerical Solution Methods

The most critical aspects of solution methods are listed as below:

Consistency

The consistency of the solution is ideally indicating that the solution of the numerical method should be ideally equivalent to exact if the grid spacing is infinitely small or tends to zero. When the grid spacing is not zero a difference in solutions between numerical and exact solutions arise and this error is refereed to as truncation error. The truncation error depends on the grid spacing Δx and time $\Delta time$.

Stability

This indicates the solution should be converging at all times and not diverging. Stability of the solution indicates how well a bounded solution is produced as the results converge. A common stability study is Von Neumann stability which involes Fourier decomposition of numerical error.

Convergence

Convergence indicates the tendency of a numerical solution to move towards an exact solution of the differential equation. Convergence can be checked usually with increase of mesh resolution and seeing if the solution changes furthermore.

Conservation

A numerical solution is conserved if the quantity leaving a closed control volume is equivalent to the amount entering and if the overall domain is obeying that the net flux of a conserved quantity is zero as well. When a finite volume method and

strong conservation form of equations are solved it ensures conservation for both individual volumes and the over all domain too.

Boundedness

Boundedness of the solution indicates that a physically reasonable solution or limits of quantities are indicated within a solution. For example quantities such as density, kinetic energy must always be positive and not negative. If they are negative it is an indication of a non-bounded solution. Often to ensure this in numerical methods the quantities are bounded within a lower and upper limit.

Accuracy

It is unimaginable to have a fully accurate solution. Errors occur from modelling, discretization and iterations. Despite these errors, they can be minimized with caution and the amount by which these errors are decreased leads to increase of accuracy of the solution. Hence one can express the accuracy of the solution as how much of exact solution of the differential equations is obtained after elimination of possible errors arising in a numerical solution.

2.2.5 Finite Difference Method

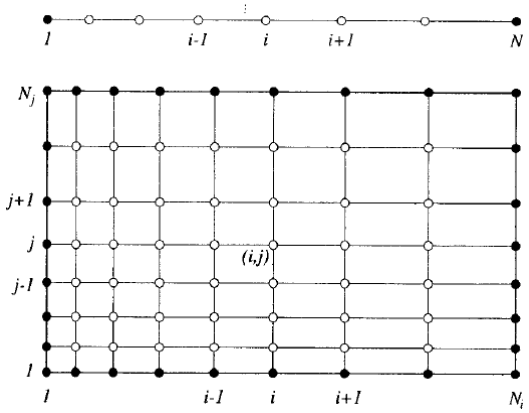

Fig. 2.5: Cartesian grid discretized for finite difference method 1d(top) and 2d(bottom).

Finite Difference methods involve calculation of derivatives at nodal points of the grid. The discretization for a conserved quantity ϕ is such that:

$$\left(\frac{\partial \phi}{\partial x}\right)_{x_i} = \lim_{\Delta x \to 0} \frac{\phi(x_i + \Delta x) - \phi(x_i)}{\Delta x} \tag{2.26}$$

where x is distance in x axis and Δx is the difference in spacing between two nodes in x axis. The approximation can be carried out with many different methods known as schemes such as forward, backward and central difference scheme.

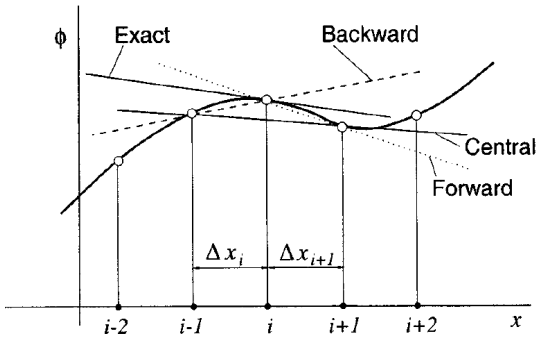

Fig. 2.6: Different schemes used in approximations of derivatives. [8]

Fig. 2.6 shows forward schemes taking the derivative value by line passing through the x_i node and the node at $x_i + \Delta x$. And for backward scheme it would be the x_i node and the node behind at $x_i - \Delta x$. Respectively central difference scheme would include nodes at $x_i - \Delta x$ and node at $x_i + \Delta x$. As in Fig. 2.6 the central difference slope is parallel to that of the exact solution and hence would be very accurate.

From Fig. 2.6 it is obvious that as the grid spacing gets smaller the slope of the solution will tend towards the slope of the exact solution.

Taylor series expansion can be used to express the differential function of $\phi(x)$ around it's neighbouring nodes. Such an approximation would go as follows.

$$\phi(x) = \phi(x_i) + (x - x_i)\left(\frac{\partial \phi}{\partial x}\right)_i + \frac{(x - x_i)^2}{2!}\left(\frac{\partial^2 \phi}{\partial x^2}\right)_i + \frac{(x - x_i)^n}{n!}\left(\frac{\partial^n \phi}{\partial x^n}\right)_i + H \quad (2.27)$$

In Eq. 2.27 H stands for " higher order terms".

Estimating **the first order derivative** usually involves ignoring the higher order terms which results in truncation and can be expressed as below.

$$\left(\frac{\partial \phi}{\partial x}\right)_i \approx \frac{\phi_{i+1} - \phi_i}{x_{i+1} - x_i} \quad (2.28)$$

$$\left(\frac{\partial \phi}{\partial x}\right)_i \approx \frac{\phi_i - \phi_{i-1}}{x_i - x_{i-1}} \quad (2.29)$$

$$\left(\frac{\partial \phi}{\partial x}\right)_i \approx \frac{\phi_{i+1} - \phi_{i-1}}{x_{i+1} - x_{i-1}} \quad (2.30)$$

Consistently the equations above are in the order of forward differencing (FDS), backward differencing (BDS) and Central Differencing (CDS) scheme. The first derivative is often used to discretize and approximate the convective terms of the N-S equations.

The approximation of second order derivatives is often applied to the diffusive terms appearing in the N-S equations. In order to do this one can use the approximation for first derivative two times. If using central difference the derivative can also be obtained at x_{i-1} and x_{i+1}. A common practice for using central difference schemes is to use $x_{i+\frac{1}{2}}$ and $x_{i-\frac{1}{2}}$ i.e halfway between grid points.

2.2.6 Finite Element Method

Finite element method (FEM) involves use of low degree piece-wise polynomials in small subintervals of finite space. The regions of small subdivision of the entire domain is referred to as finite elements [11]. FEM is a well known method amongst numerical engineers and mathematicians as the method is more mathematical and robust than Finite Difference and Finite Volume method. However, it is less conservative compared to the Finite Volume Method.

Discretized domain approximation is carried out using interpolation polynomials to obtain the variations of variables. The Galerkin method is then used for further approximation of the derivatives. The system of algebraic equations that arise are solved to get the approximate solution.

2.2.7 Finite Volume Method

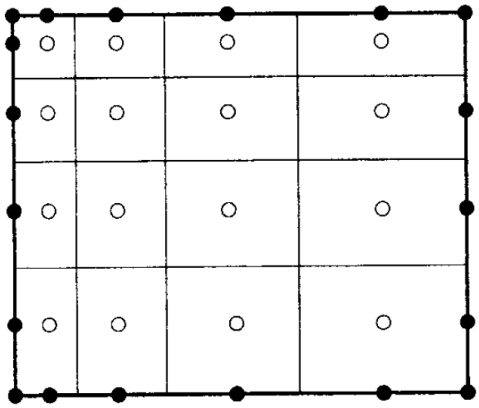

Fig. 2.7: Typical arrangement of control volume (CV) and nodes in Finite volume Method. [8]

As shown in Fig. 2.7 the node centered in the control volume arrangement is used as a common practice. The Finite volume method utilizes the conservation equation's integral form. The advantage of this method is that the values at the node represents the mean average over the control volume to the second order of accuracy.

$$\int_S \rho\phi \boldsymbol{v} \cdot \mathbf{n} dS = \int_S \Gamma \, grad\, \phi \cdot \mathbf{n} dS + \int_\Omega q_\phi d\Omega \tag{2.31}$$

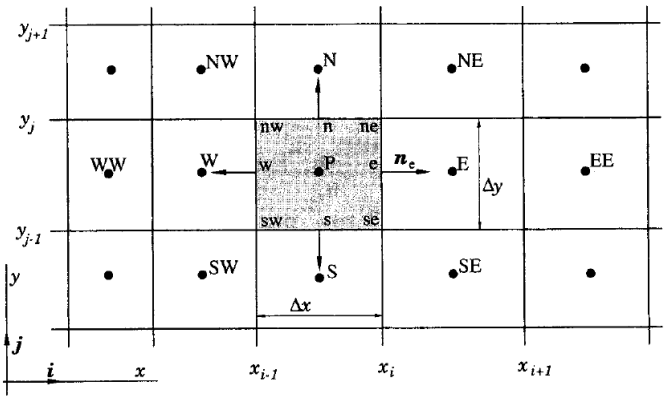

Fig. 2.8: Discretization in finite volume method for a 2D cartesian grid [8]

The **surface integrals** are approximated with use of such control volumes as shown in Fig. 2.8. The net flux through the control volumes boundary is the sum of integrals over the four faces in 2D.

$$\int_S f\,dS = \sum_k \int_{S_k} f\,dS, \tag{2.32}$$

where f stands for the component of convective or diffusive flux vector in the normal direction to the face of the CV. The only calculation is done for the flux ϕ . The integrals must be calculated and approximated in a two step process where the face integrals are obtained and the cell-face values are approximated in terms of nodal values. One of the most simple and commonly utilized approximation method is the **midpoint rule** where the integral is approximated as a product of the integrands at the cell-face center and the cell-face area. This method is of *second order of accuracy*. Such approximations can also be made with other rules such as **trapeziod rule** which is also of second order of accuracy or using **Simpson's rule** which is 4th order accurate.

For midpoint rule:

$$F_e = \int_{S_e} f\ dS\ =\ \bar{f}_e S_e \approx f_e S_e \tag{2.33}$$

For trapezoid rule:

$$F_e = \int_{S_e} f\ dS\ =\ \frac{S_e}{2}(f_{ne} + f_{se}) \tag{2.34}$$

and for Simpon's rule:

$$F_e = \int_{S_e} f\ dS\ =\ \frac{S_e}{6}(f_{ne} + 4\ f_e + f_{se}) \tag{2.35}$$

Volume integrals

There are terms in NS equations that require integration over a control volume rather than a surface. The mean value of the integrand can be approximated at the cell center;

$$Q_p = \int_{\Omega} q \, d\Omega \; = \; \bar{q} \, \triangle\Omega \; \approx \; q_P \triangle\Omega \tag{2.36}$$

Interpolation Schemes

The integrals needs to be approximated not just at cell nodes but also at cell centers. Interpolation can be used to approximate these integrals. The Upwind Differencing Scheme (UDS) is a famous method in interpolation and is of first order accuracy. Such an approximation will not yield oscillatory solutions, however, are known to be numerically diffusive. Other interpolation methods include second order accurate Central Differencing Scheme (CDS), Quadratic Upwind Interpolation (QUICK) and other high-order schemes [8].

2.2.8 Application of the Numerical Framework settings to CFD

The various components and methods discussed prior, has several impacts on the accuracy of CFD simulations. The grid plays an important role in determining whether accurate solutions are produced. The denser the grid, the better the solution but with a compromise of the time taken to reach convergence. Hence, the right amount of grid cells should be chosen in order to get an accurate but a cost effective solution. Other components mentioned such as stability, convergence and boundedness, plays a vital role in maintaining accuracy of the simulation as well. If the solution is not stable, then it could mean that either the grid is of bad quality or numerical setup is not correct. Sometimes, if an unsteady simulation is solved with a steady state solver, the solution in unstable as well. Hence, the stability of the solution speaks for errors in the numerical grid, setup or type of solver. Furthermore, judging convergence is also important as it indicates how much of a true solution has actually been achieved. In aerodynamics the true convergence is a mere outcome of convergence in the residuals of Navier Stokes equations and the convergence of aerodynamic forces and moments. Hence, one should be able to tell the right solution by looking at these two components simultaneously rather than individually.

2.2.9 Turbulence Models

Since the equations are based on Reynolds averaging of the fluctuations of components of the stresses that arise we close the Navier-Stokes(NS) equations in RANS/URANS with assumption that they can be estimated by introducing the concept of eddy viscosity [12]. Linear Eddy viscosity models use the Boussinesq assumption that the stresses are proportional to the strain rate due to the mean velocity gradients.

$$\tau_i j = 2\mu_t\Big(S_{ij} - \frac{1\partial u_k}{3\partial x_k}\delta_{ij}\Big) - \frac{2}{3}\rho k\delta_{ij} \tag{2.37}$$

Where S_{ij} is the strain rate magnitude of velocity vector.

Cebeci - Smith Model

The Cebeci - Smith model [13] is an algebraic model that assumes two zones of eddy viscosity, the inner and outer zones. The zones are distinguished by a normal wall distance $y_{crossover}$ and the viscosity in the outer zone is calculated using the velocity thikness. The model follows as:

The inner region of viscosity is calculated by:

$$\mu_{t_{inner}} = \rho l^2\left[\left(\frac{\partial U}{\partial y}\right)^2\left(\frac{\partial V}{\partial x}\right)^2\right]^{1/2} \tag{2.38}$$

where

$$l = ky\Big(1 - e^{\frac{-y+}{A+}}\Big) \tag{2.39}$$

the outer region of viscosity is given by:

$$\mu_{t_{outer}} = \alpha\rho U_e\delta_v^* F_{KLEB}(y;\delta) \tag{2.40}$$

where F_{KLEB} is the intermittency factor.

Baldwin Lomax Model

Baldwin - Lomax model assumes two zones of eddy viscosity the inner and outer zones. The distance at which two viscosity zones are separated is determined by a normal wall distance $y_{crossover}$. The Cross over distance is the minimum wall distance at which the outer and inner eddy viscosities are equal to each other.

The inner region can be computed with the Prandtl - Van Driest formula:

$$\mu_{t_{inner}} = \rho l^2|\Omega| \tag{2.41}$$

where

$$l = ky\Big(1 - e^{\frac{-y+}{A+}}\Big) \tag{2.42}$$

$$|\Omega| = \sqrt{2\Omega_{ij}\Omega_{ij}} \tag{2.43}$$

$$\Omega_{ij} = \frac{1}{2}\Big(\frac{\partial u_i}{\partial x_j} - \frac{\partial u_j}{\partial x_i}\Big) \tag{2.44}$$

The outer eddy viscosity is computed with:

$$\mu_{t_{outer}} = \rho K C_{cp} F_{WAKE} F_{KLEB(y)} \tag{2.45}$$

where F_{WAKE} is given by:

$$F_{WAKE} = min\left(Y_{MAX}F_{MAX}; C_{WK}Y_{MAX}\frac{U_{DIF}^2}{F_{MAX}}\right) \tag{2.46}$$

where Y_{MAX} and F_{MAX} are obtained from the maximums of the function (F), which means that Y_{MAX} is the distance at which function $F(y)$ goes to the maximum value and $F_{KLEB(y)}$, the intermittency factor, is defined as:

$$F_{KLEB(y)} = \left[1 + 5.5\left(\frac{yC_{KLEB}}{Y_{MAX}}\right)^6\right]^{-1} \tag{2.47}$$

where U_{DIF} is the difference in the maximum and minimum speed in the velocity profiles.

Algebraic models allows us to compute quick iterative simulations in the design process without much computation costs and time. DES, LES and DNS are still costly and require much more computing power developments to be able to used as an every day substitute in the design and testing phases. Therefore it is essential to improve RANS and eddy viscosity concepts and rely on these models with our computing power and capabilities at the moment.

The original Baldwin-Lomax (BL) model [14] has difficulties in implementation as it requires the dimensionless wall distance $Y+$ along a line from the wall up to the far fields. Only structured grids and some solvers are capable of determining this. Therefore the model presents challenges in itself. Furthermore, we also face issues in that the $F(y)$ function goes to maximum twice in the profile, once close to the wall and then right after the prior maximum. The solver confuses in determining which is the actual F_{MAX} function as they vary in value and the two peaks fluctuate and dominate individually at different times. This indeed changes the Y_{MAX} obtained from the maximum of function F_{MAX} and greatly overestimates the eddy viscosities. And the requirement for calculation of the crossover distance to determine two zones of eddy viscosities presents difficulties too, as the inner and eddy viscosities might be equal to each other at more than one wall distance for a given problem. The challenges associated with the Baldwin - Lomax model can be further read in [14].

Spalart - Allmaras Model

This One - Equation Eddy Viscosity Model [15] is used for turbulence closure where modified turbulence viscosity $\hat{v}$, is solved with the PDE system:

$$\frac{\partial\hat{v}}{\partial t} + u_j\frac{\partial\hat{v}}{\partial x_j} = C_{b1}(1-f_{t2})\hat{S}\hat{v} - \left[C_{w1}.f_w - \frac{C_{b1}.f_{t2}}{\kappa^2}\right]\left(\frac{\hat{v}}{d^2}\right) + \frac{1}{\sigma}\left[\frac{\partial}{\partial x_j}(v+\hat{v})\frac{\partial\hat{v}}{\partial x_j} + C_{b2}\frac{\partial\hat{v}}{\partial x_i}\frac{\partial\hat{v}}{\partial x_i}\right] \tag{2.48}$$

and the turbulence viscosity is then obtained from:

$$\nu_t = \hat{v}.f_{v1} \tag{2.49}$$

where f_{v1} in the equation above is:

$$f_{v1} = \frac{X^3}{X^3 + C_{v1}^3} \tag{2.50}$$

where X is:

$$X = \frac{\hat{v}}{v} \tag{2.51}$$

The model constants are:
$\sigma = 2/3$,$C_{b1} = 0.1355$, $C_{b2} = 0.622$, $\kappa = 0.41$, $C_{w1} = C_{b1}/\kappa^2 + (1 + C_{b2})/\sigma$, $C_{w2} = 0.3$, $C_{w3} = 2$, $C_{v1} = 7.1$, $C_{t1} = 1$.

Production of turbulence is defined as: $C_{b1}(1 - f_{t2})\hat{S}\hat{v}$,
Diffusion term for turbulence is defined as : $\frac{1}{\sigma}[\frac{\partial}{\partial x_j}(v + \hat{v})\frac{\partial \hat{v}}{\partial x_j} + C_{b2}\frac{\partial \hat{v}}{\partial x_i}\frac{\partial \hat{v}}{\partial x_i}]$,
and the destruction of turbulence is defined as: $[C_{w1}.f_w - \frac{C_{b1}.f_{t2}}{\kappa^2}](\frac{\hat{v}}{d^2}) + \frac{1}{\sigma}]$.

k - epsilon model

This model [16] is one of the most generally applied turbulence models in CFD simulations.

The turbulent kinetic energy is given by:

$$\frac{\partial k}{\partial t} + \frac{\partial u_j k}{\partial x_j} = P_k + P_b - \rho\epsilon - Y_M + \frac{\partial}{\partial x}\left[(\mu + \mu_t/\sigma_k)\frac{\partial k}{\partial x_j}\right] + S_k \tag{2.52}$$

$$\frac{\partial \epsilon}{\partial t} + \frac{\partial u_j \epsilon}{\partial x_j} = C_{1\epsilon}\frac{\epsilon}{k}(P_k + C_{3\epsilon}P_b) - C_{2\epsilon}\frac{\epsilon^2}{k} + \frac{\partial}{\partial x}\left[(\mu + \mu_t/\sigma_\epsilon)\frac{\partial \epsilon}{\partial x_j}\right] + S_\epsilon \tag{2.53}$$

and the turbulence viscosity is defined as:

$$v_t = C_\mu \frac{k^2}{\epsilon} \tag{2.54}$$

where P_k is the production of turbulence and P_b is the effect of buoyancy.

The model coefficients are set as follows: $C_{1\epsilon} = 1.44$, $C_{2\epsilon} = 1.92$, $C_\mu = 0.09$, $\sigma_k = 1.0$ and $\sigma_\epsilon = 1.3$.

k - ω Model

In this turbulence model [17] the turbulent kinetic energy is given by:

$$\frac{\partial k}{\partial t} + \frac{\partial u_j k}{\partial x_j} = P_k - \beta^* k\omega + \frac{\partial}{\partial x}\left[(\mu + \sigma_k\mu_t)\frac{\partial k}{\partial x_j}\right] \tag{2.55}$$

$$\frac{\partial \omega}{\partial t} + \frac{\partial u_j \omega}{\partial x_j} = \alpha\frac{\omega}{k}P_k - \beta\omega^2 + \frac{\partial}{\partial x}\left[(\mu + \sigma_\omega\mu_t)\frac{\partial \omega}{\partial x_j}\right] \tag{2.56}$$

and the turbulence viscosity is defined as:

$$v_t = \frac{k}{\omega} \tag{2.57}$$

k - ω SST Model

$$\frac{\partial k}{\partial t} + \frac{\partial u_j k}{\partial x_j} = (P_k - \beta^\star \omega k + \frac{\partial}{\partial x_j}\left[(\mu + \sigma_k v_t)\frac{\partial k}{\partial x_j}\right] \tag{2.58}$$

$$\frac{\partial \omega}{\partial t} + \frac{\partial u_j \omega}{\partial x_j} = \frac{\gamma}{\nu_t}(P_k - \beta\rho\omega^2 + \frac{\partial}{\partial x_j}\left[(v + \sigma_\omega v_t)\frac{\partial \omega}{\partial x_j}\right] + D \tag{2.59}$$

where Turbulent Viscosity is defined as:

$$v_t = \frac{a_1 k}{max(a_1\omega, \Omega F_2)} \tag{2.60}$$

Detached Eddy Simulations

The RANS models approximate steady state and unsteady flows with small separated regions quite well, but their ability to predict transient flows with large separation zones or other complicated phenomenon is not very accurate[18]. The Large Eddy Simulations can predict unsteady flows with large separation zones very well. However, using LES for some problems (specially in aerodynamics with wall bounded flows) leads to unnecessary accuracy in some regions of the flow field. A hybrid RANS/LES approach is more suitable, where RANS will be applied only in regions close to the wall.

Spalart was the first who proposed such a hybrid method called DES. The modification proposed in [19] includes the hybrid combinations of RANS closed by the Spalart-Allmaras turbulence model [15] along with LES.

Recall the S-A model equation:

$$\frac{\partial \hat{v}}{\partial t} + u_j \frac{\partial \hat{v}}{\partial x_j} = C_{b1}(1 - f_{t2})\hat{S}\hat{v} - \left[C_{w1}.f_w - \frac{C_{b1}.f_{t2}}{\kappa^2}\right]\left(\frac{\hat{v}}{d^2}\right) + \frac{1}{\sigma}\left[\frac{\partial}{\partial x_j}(v+\hat{v})\frac{\partial \hat{v}}{\partial x_j} + C_{b2}\frac{\partial \hat{v}}{\partial x_i}\frac{\partial \hat{v}}{\partial x_i}\right] \tag{2.61}$$

in which the turbulence destruction term is:

$$\left[C_{w1}.f_w - \frac{C_{b1}.f_{t2}}{\kappa^2}\right]\left(\frac{\hat{v}}{d^2}\right) \tag{2.62}$$

The d (wall distance) in Eq. 2.62 is replaced with:

$$\hat{d} = min(d, C_{des}\triangle) \tag{2.63}$$

When the modified distance $\hat{d} = d$, S-A model is activated and when $\triangle << d$ the subgrid scale model is activated. Parameter $\triangle$ is the maximum length of the cell in either X, Y or Z direction and C_{des} is calibrated to be 0.65.

Large Eddy Simulations

Direct Numerical Solutions (DNS) provide the most accurate solutions resolving the movement of smallest scale eddies. LES solves larger scale motions of the

eddies (see Fig. 2.9). Most of the energy and other conservative properties are transported mostly through large scale eddies. Smaller eddies have lesser influence on this transport mechanism. Hence, LES can be used to effectively model flows where DNS is not feasible as LES is very accurate, more cost effective and less time consuming than DNS.

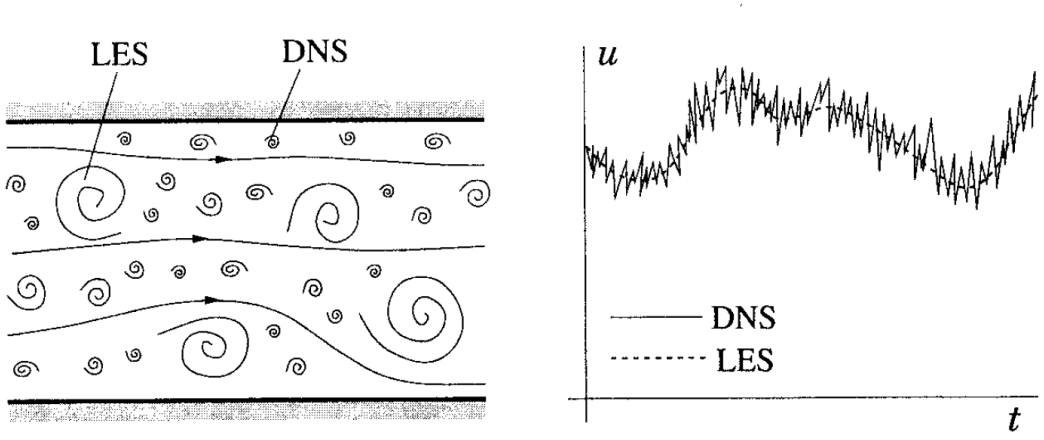

Fig. 2.9: LES/DNS turbulent motion(left) and time-dependent velocity fluctuations(right)[8].

In order to resolve the larger scales of motions the velocity is filtered:

$$\bar{u_i}(x) = \int (x, x')u_i(x')dx' \tag{2.64}$$

The averaging in Eq. 2.64 is introduced to incompressible NS equations, it leads to equations, which are very similar to RANS equations.

Filtering does not introduce any changes to the continuity equation:

$$\nabla \cdot \bar{u} = 0 \tag{2.65}$$

The momentum equation after filtering is written as:

$$\frac{\partial \bar{u}}{\partial t} + \nabla \overline{uu} = -\nabla \bar{p} + \nabla \Big[\mu \Big(\nabla \bar{u_i} + \nabla \bar{u_j}\Big)\Big] \tag{2.66}$$

and it is important to note the difference that, $\overline{uu} \neq \bar{u}\bar{u}$

$$\tau_{ij}^{s} = -\rho(\overline{uu} - \bar{u}\bar{u}) \tag{2.67}$$

Parameter τ_{ij}^{s} in Eq. 2.67 is the subsgrid-scale Reynolds stress. One of the most common and earliest LES model is the Smagorinsky model. There are other models which are available such as the Dynamic and Deconvolution model.

Direct Numerical Simulations

Direct Numerical Simulations (DNS) are the most expensive and most accurate approach to solve turbulent flows. There is no averaging involved in DNS. The only introduced errors are through discretization and numerical approximations.

DNS is too expensive to be used as a simulation method for flows of engineering interest, which is turbulent with high velocities and high Reynolds numbers. The available computing facilities are only capable of simulating DNS for very low Reynolds number flow conditions.

The results from DNS can be used to validate current RANS/DES/LES modelling approaches allowing one to introduce more approximation and improvement strategies. The modelling of flow using DNS is out of the scope of this Thesis and the interested reader is referred to [8]

Chapter 3

OpenFOAM

3.1 Introduction

OpenFOAM stands for Open Field Operations and Manipulations. It is an open source computational fluid dynamics software written in the object oriented C++ language. It utilizes advanced programming techniques with custom defined templates and data structures. Such an open source CFD softwares provides the research community a strong motivation to continue and develop on concepts of the fluid dynamics.

Since it is written in C++ and every program and models are available to modify, users have advanced control and option to develop and improve on the existing physical, numerical and mathematical models. Furthermore, this also provides a very reliable opportunity to design and develop applications for a particular need.

OpenFOAM [5] has been developed over more than a decade now and hence the applications, the numerical methods and the results are well verified and validated for aerodynamics of aircraft.

3.1.1 User Control and Interfaces

OpenFOAM is a command line control and text editor based software and therefore the official version of OpenFOAM does not include an interface. Text files are used to control the inputs and outputs. Like most other open source softwares it's source codes are developed in a Linux support environment. However, due to the large demand for windows and OS x applications binaries and ways to build from source codes have been developed over the years. While there are many ways to do this, CygWin is the leading choice to use OpenFOAM on windows.

3.1.2 Solvers

OpenFOAM comes with two different kinds of solvers. A list of solvers that are most applicable to computational aerodynamics and available in the software is as follows.

1. **simpelFOAM** solves the steady state NS equations using RANS turbulence

closure. This is mainly used for analysis of airflow past airfoils at low angles of attacks with no or minimum separation.

2. **pisoFOAM** solves the time accurate unsteady NS equations using RANS turbulence closure and an explicit time marching algorithm. This is mainly used for analysis of airflow past airfoils at high angles of attack with large separation zones and unsteady flow and helps to accurately predict the stall aerodynamics. The Courant number used for this solver must be strictly below 1.

3. **pimpleFOAM** solves the time accurate NS equations using RANS turbulence closure and an implicit time marching algorithm. This is mainly used for analysis of airflow past airfoils at high angles of attack with large separation zones and unsteady flow and helps to accurately predict the stall aerodynamics. This algorithm involves inner loops in every time step to reach for a steady state and hence a Courant number of 20 and below can be used with caution.

3.2 Numerical Methods

OpenFOAM is a CFD code written in C++ using the well known Finite Volume Method. In this section, the numerical methods related to OpeNFOAM will be discussed.

The control volume for CFD evaluation using the FVM in OpenFOAM is shown in Fig. 3.1.

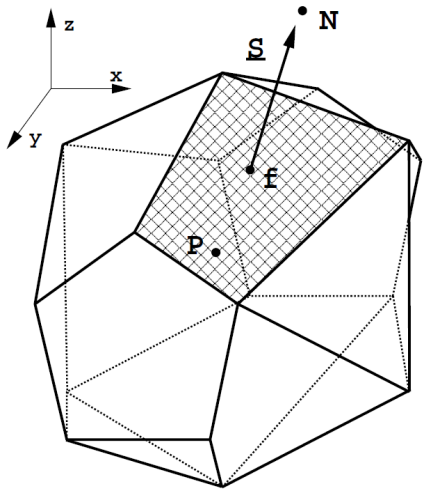

Fig. 3.1: Control volume [20].

3.2.1 Spatial Discretization

Convection term

The convection term in OpenFOAM is discretized as:

$$\int_{V_P} \nabla \cdot (\rho U \phi) dV = \sum_f S.(\rho U \phi)_f \tag{3.1}$$

Differencing schemes for the convection term uses the current cell and the nearest neighbour. The face value is then calculated with the **central differencing scheme** as[20]:

$$\phi_f = f_x \phi_P + (1 - f_x)\phi_N \tag{3.2}$$

Blended differencing scheme (a hybrid between upwind and central differencing) can also be used to express the face value of ϕ and is determined as:

$$\phi_f = (1 - \gamma)(\phi_F)_{UD} + \gamma(\phi_F)_{CD} \tag{3.3}$$

The constant γ determines the blend between upwind and central differencing and affects the accuracy and boundedness of the solution.

Diffusion term

The diffusion term in OpenFOAM is discretized as:

$$\int_{V_P} \nabla \cdot (\rho \Gamma_\phi \nabla \phi) dV = \sum_f S.(\rho \Gamma_\phi \nabla \phi)_f \tag{3.4}$$

Source terms

Terms other than convection and diffusion or temporal terms are source terms and are linearized as follows[20].

$$S_\phi(\phi) = Su + Sp\phi \tag{3.5}$$

3.2.2 Temporal Discretization

Crank-Nicholson method

Using the Crank-Nicholson method the temporal discretization is decsribed as:

$$\frac{\rho_P \phi_P^n - \rho_P \phi_P^o}{\Delta t} V_P = SuVp + \frac{1}{2} S_P V_P \phi_P^n + \frac{1}{2} S_P V_P \phi_o^n \tag{3.6}$$

The Crank-Nicholson method is unconditionally stable but does not guarantee the accuracy of the solution [20].

A first order accurate in time method used in an explicit manner is described below:

$$\frac{\rho_P \phi_P^n - \rho_P \phi_P^o}{\Delta t} V_P + \sum_f F\phi_f - \sum_f (\rho\Gamma_\phi)_f S.(\nabla\phi)_f = SuVp + S_P V_P \phi_P \tag{3.7}$$

In explicit discretization the old time field values are used to obtain the face values of ϕ and $\nabla\phi$. If Courant number (CFL) is bigger than 1 the system becomes unstable.

Euler Explicit method The Euler explicit method requires face values from the old time field and can be described as:

$$S.(\nabla\phi)_f = |\triangle| \frac{\phi_N^o - \phi_P^o}{|d|} + k.(\nabla\phi)_f^o \tag{3.8}$$

Euler Implicit method The Euler implicit method to obtain face values is:

$$S.(\nabla\phi)_f = |\triangle| \frac{\phi_N - \phi_P}{|d|} + k.(\nabla\phi)_f \tag{3.9}$$

The resulting system from the Euler implicit method is still first order accurate but more stable than the Euler explicit method so the Courant number limit can still be violated within reasonable limits.

Backward differencing method

The discretized equation for backward differencing is as:

$$\frac{\frac{3}{2}\rho_P \phi^n - 2\rho_P \phi^o + \frac{1}{2}\rho_P \phi^{oo}}{\Delta t} V_P + \sum_f F\phi_f^n - \sum_f (\rho\Gamma_\phi)_f S.(\nabla\phi)_f^n = SuVp + S_P V_P \phi_P^n \tag{3.10}$$

3.2.3 Boundary conditions

Fig. 3.2 helps to understand the notations in a boundary cell of OpenFOAM.

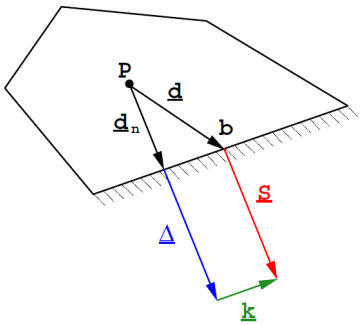

Fig. 3.2: Control volume in the boundary reprinted from [20].

The **Fixed Value boundary condition** for the **convection term** in OpenFOAM in terms of the face value is written as:

$$F_b \phi_b \tag{3.11}$$

where F_b is the face flux and ϕ_b is the fixed value of phi on the face.

And the **diffusion term** is written as:

$$S.(\nabla\phi)_b = |S| \frac{\phi_b - \phi_P}{|d_n|} \tag{3.12}$$

The **Fixed Gradient boundary condition** is written as:

$$\left(\frac{S}{|S|} . \nabla\phi \right)_b = g_b \tag{3.13}$$

3.3 Validation of OpenFoam for Aerodynamics

In order to use OpenFOAM for simulation of subsonic and transonic flight regime conditions it must be validated. Even though OpenFOAM is the most validated open source CFD code available in the public domain it seems ideal to validate and compare results to published results in order to be able to qualify it as a reliable CFD code. Various test results using OpenFOAM at different flight conditions are brought forward in the following sections.

3.3.1 CFD results for NACA - 0012 airfoil at Re = 6 million against Experimental results

In the following simulation, NACA 0012 airfoil is simulated at moderately high Reynolds number of ($Re = 6million$). The grid was made according to the specific requirements stated in [12]. The simulation results show that the OpenFOAM predictions matches well with wind tunnel test results up to maximum lift coefficient, $C_{L_{max}}$. The stall is offset by 2 degrees and there may be a number of reasons for the offset such as turbulent intensity or tripping condition.

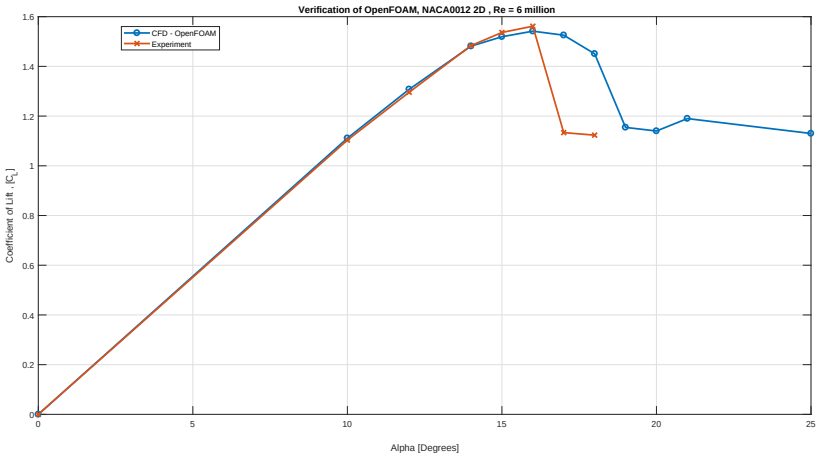

Fig. 3.3: OpenFOAM SST model vs. Experimental results for NACA-0012 airfoil at $Re = 6\ million$.

3.3.2 CFD results for NACA - 4412 airfoil at Re = 6 million against Experimental results

The simulation of NACA 4412 airfoil at moderately high Reynolds number of 6 million is carried out using OpenFOAM. The flow domain is shown in Fig. 3.4 and the blocking with the grid generated are shown in Fig. 3.5. The grid was made up of 44,000 elements and caution was given to ensure that the orthoganlity of the grid is maintained while still adapting the grid around the cambered shape of this airfoil. The boundary resolution consisted of 10 layers with an increase of cell height by a ratio of 1.1 normal to the airfoil. The first cell had a Y+ of 1 or below ensuring that the boundary is well resolved.

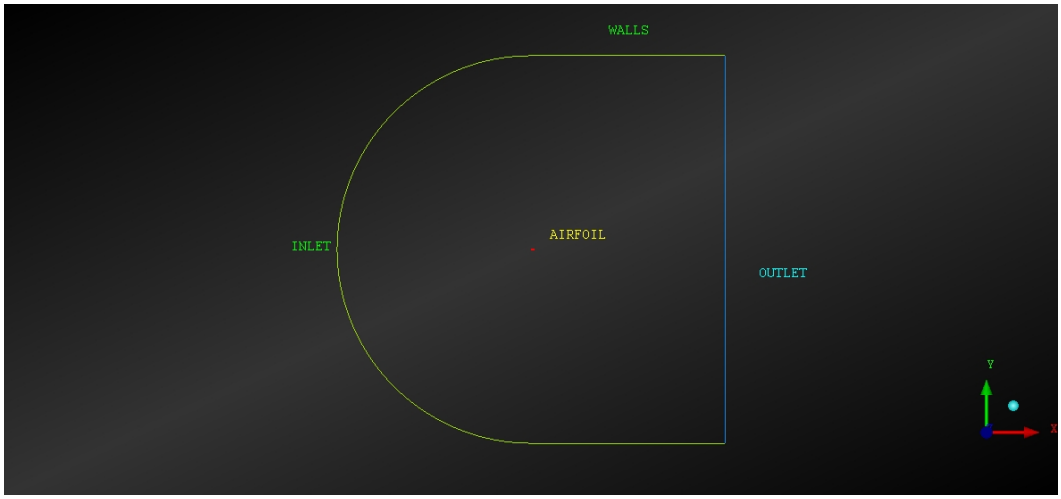

Fig. 3.4: Computational Domain for NACA 4412 airfoil CFD simulation.

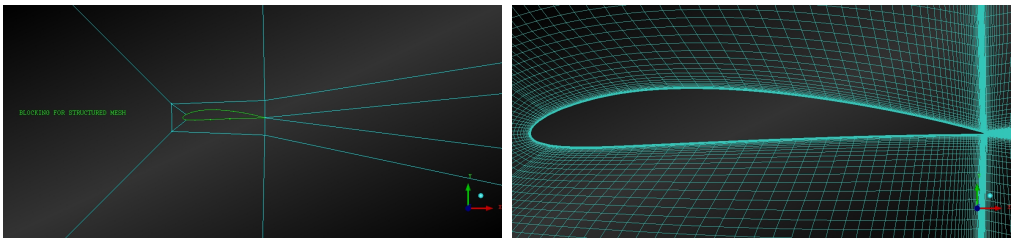

Fig. 3.5: Blocking and Grid for structured meshing of NACA 4412 airfoil CFD simulation.

The computational results plotted against the experimental result from Abott [12] are shown in Fig. 3.6. The results show a good match between CFD and the experimental tests. In Fig. 3.7 the contours of the velocity for various angle of attacks are shown, indicating an increase in the tip separation (blue region) with the increase of angle of attack.

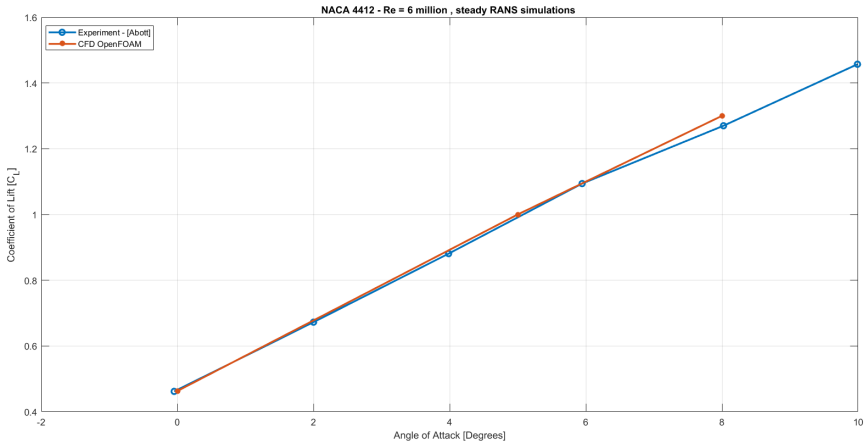

Fig. 3.6: Results for NACA 4412 airfoil at $Re = 6million$ compared against experiment from Abott.

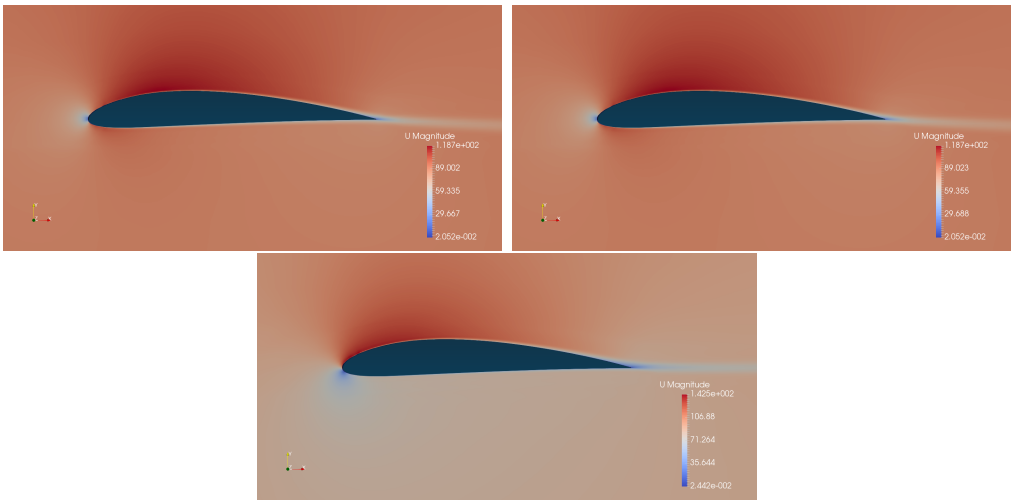

Fig. 3.7: Contours of Velocity for NACA 4412 airfoil at $Re = 6million$ top left $\alpha = 0°$, top right $\alpha = 5°$ and bottom $\alpha = 8°$.

3.3.3 Turbulent Flow past Cylinder at Re = 100,000

The time-accurate method PISO (Pressure Implicit Split Operator) is compared against the pseudo time accurate algorithm SIMPLE (Semi - Implicit Pressure Linked Equations).

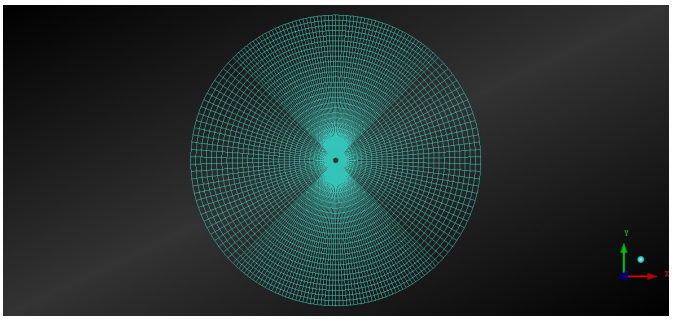

Fig. 3.8: Computational setup for flow past cylinder at $Re = 100,000$.

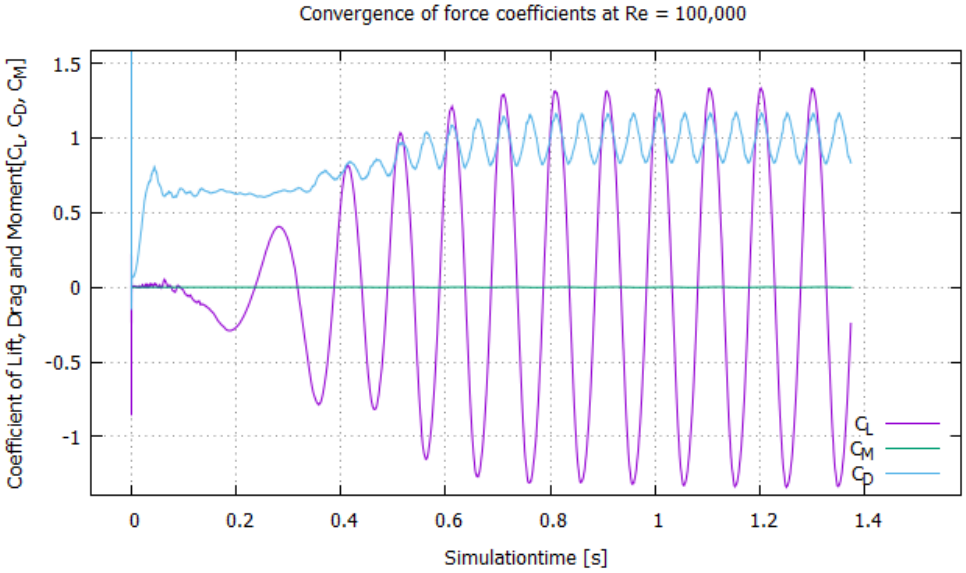

Fig. 3.9: Convergence of force coefficients, URANS, S-A model, PISO $Re = 100,000$.

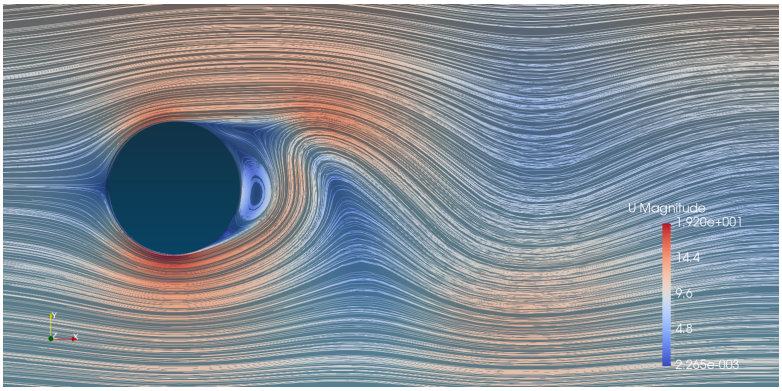

Fig. 3.10: Streamline visualization of fully developed flow past the cylinder, URANS, S-A model, PISO $Re = 100,000$.

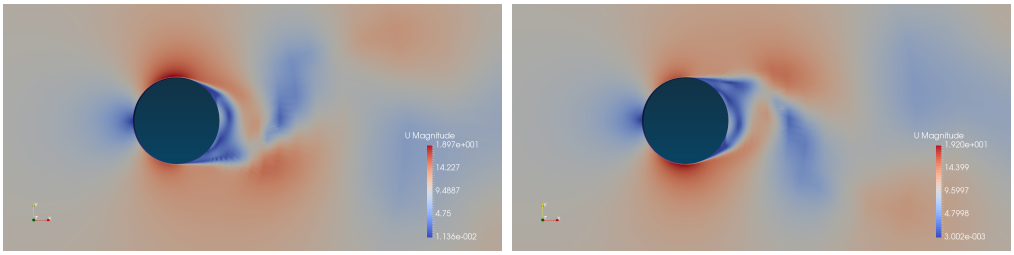

Fig. 3.11: Contours of velocity at $time = 1.2s$ for maximum lift coefficient [left] and $time = 1.25s$ for minimum lift coefficient [right] URANS, S-A model, PISO $Re = 100,000$.

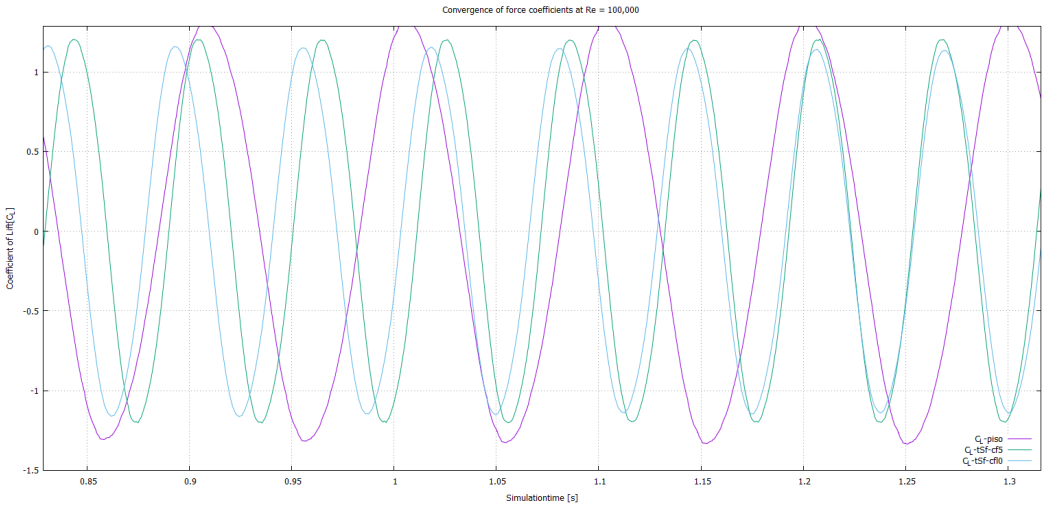

Fig. 3.12: Convergence of lift force for PISO vs. Unsteady SIMPLE algorithm $Re = 100,000$.

The only visible difference is a very slight shift in C_{L-max} and C_{L-min} and the time period shift towards the right. However, the mean values of unsteady fluctuations in lift are still zero for both solvers and shows the same physical results as we expect for fully developed flow past cylinder at reasonable Reynolds number of 100,000. It can be concluded that the transient SIMPLE algorithm can be successfully used to simulate unsteady processes and hence save the time and cost of the simulations.

3.4 Contribution to OpenFOAM

Various new and modified solvers, turbulence models, matrix solvers and dynamic mesh movement methods have been implemented in OpenFOAM as a work of this Thesis for the purpose of speed up and improvement of accuracy of the simulations. The interested reader in the source code is referred to appendix of the Thesis. A mathematical description of the source codes is presented briefly as follows.

3.4.1 transientSimpleFoam - Unsteady flow solver with Adapative Time Stepping

This solver is called as transientSimpleFoam because it involves the Semi-Implicit Pressure Linked Equations(SIMPLE) algorithm and as it solves the unsteady NS equations (in two stages A and B).

A1 - Outer loop calculations begin

1 -Initially, momentum equation (Ueqn) are described as:

$$\frac{\partial \mathbf{u}}{\partial t} + \nabla(\mathbf{uu}) - \nu\nabla^2\mathbf{u} = -\frac{\nabla \mathbf{p}}{\rho} \tag{3.14}$$

2 - The equations are solved against the prescribed pressure gradient and under relaxation of velocity is applied.

3 - The pressure boundary conditions are updated.

4 - The diagonal terms(H) and off diagonal terms(A) in matrix system of the equation 3.14 (Ueqn) can be denoted by **Ueqn.H()** and **Ueqn.A()** respectively.

5 - A new term rAU is expressed as:

$$rAU = 1/Ueqn.A() \tag{3.15}$$

6 - Velocity at faces are obtained by:

$$U = \frac{rAU}{Ueqn.H()} \tag{3.16}$$

7 - Flux (ϕ) is expressed as:

$$\phi = interpolate(U) \cdot \Omega_{SF} \tag{3.17}$$

where Ω_{SF} is the cell face area and Ω is the control volume.

B - Inner loop calculations begin

8 - the pressure equation (pEqn)is then solved as:

$$\nabla \cdot \left(\frac{1}{rAU}\nabla p\right) = \nabla\phi \tag{3.18}$$

9 - In the final step the flux ϕ is corrected by deducting the flux of Eqn. 3.18.

$$\phi = \phi - \phi_{pEqn} \tag{3.19}$$

A2 - Back to the outer loop

10 - pressure is under relaxed to allow for stability and convergence.

11 - Correct the cell velocities with the new pressure obtained.

$$U = U - (rAU \times \nabla P) \tag{3.20}$$

12 - Final step is to correct the turbulent quantities.

3.4.2 transientSimpleDyFoam - Unsteady Large Courant flow solver with Dynamic Mesh Movement

A1 - Outer loop calculations begin

1 -Fluxes are determined and corrected with respect to cell locations after dynamic meshing.

$$\phi = interpolate(U) \cdot \Omega_{SF} \tag{3.21}$$

$$correct(\phi) \tag{3.22}$$

2 -momentum equation (Ueqn) are described as:

$$\frac{\partial \mathbf{u}}{\partial t} + \nabla(\mathbf{uu}) - \nu\nabla^2\mathbf{u} = -\frac{\nabla \mathbf{p}}{\rho} \tag{3.23}$$

3 - The equations are solved against the prescribed pressure gradient and under relaxation of velocity is applied.

4 - The pressure boundary conditions are updated.

5 - The diagonal terms(H) and off diagonal terms(A) in matrix system of the equation 3.23 (Ueqn) can be denoted by **Ueqn.H()** and **Ueqn.A()** respectively.

5 - A new term rAU is expressed as:

$$rAU = 1/Ueqn.A() \tag{3.24}$$

6 - Velocity at faces are obtained by:

$$U = \frac{rAU}{Ueqn.H()} \tag{3.25}$$

7 - Flux (ϕ) is expressed as:

$$U = interpolate(\phi) \cdot \Omega_{SF} \tag{3.26}$$

where Ω_{SF} is the cell face area and Ω is the control volume.

B - Inner loop calculations begin

8 - the pressure equation (pEqn)is then solved as:

$$\nabla \cdot \left(\frac{1}{rAU}\nabla p\right) = \nabla\phi \tag{3.27}$$

9 - In the final step the flux ϕ is corrected by deducting the flux of Eqn. 3.27

$$\phi = \phi - \phi_{pEqn} \tag{3.28}$$

A2 - Back to the outer loop

10 - pressure is under relaxed to allow for stability and convergence.

11 - Correct the cell velocities with the new pressure obtained.

$$U = U - (rAU \times \nabla P) \tag{3.29}$$

12 - Final step is to correct the turbulent quantities.

3.4.3 hysteresisFoam - incorporates pre-history of pressure

A1 - Outer loop calculations begin

1 -Initially, momentum equation (Ueqn) are described as:

$$\frac{\partial \mathbf{u}}{\partial t} + \nabla(\mathbf{uu}) - \nu\nabla^2\mathbf{u} = -\frac{\nabla \mathbf{p}}{\rho} \tag{3.30}$$

2 - The equations are solved against the prescribed pressure gradient and under relaxation of velocity is applied.

3 - The pressure boundary conditions are updated, variable A is introduced which stands for the iteration number in the simulation and pressure is corrected with respect to old time step(n-1) and old.old time step pressure (n-2)

$$p = 0.85p + 0.15p_{n-1} + 0.05p_{n-2} \tag{3.31}$$

where n stands for time step number

4 - The diagonal terms(H) and off diagonal terms(A) in matrix system of the equation 3.30 (Ueqn) can be denoted by **Ueqn.H()** and **Ueqn.A()** respectively.

5 - A new term rAU is expressed as:

$$rAU = 1/Ueqn.A() \tag{3.32}$$

6 - Velocity at faces are obtained by:

$$U = \frac{rAU}{Ueqn.H()} \tag{3.33}$$

7 - Flux (ϕ) is expressed as:

$$\phi = interpolate(U) \cdot \Omega_{SF} \tag{3.34}$$

where Ω_{SF} is the cell face area and Ω is the control volume.

B - Inner loop calculations begin

8 - the pressure equation (pEqn)is then solved as:

$$\nabla \cdot \left(\frac{1}{rAU}\nabla p\right) = \nabla\phi \tag{3.35}$$

9 - In the final step the flux ϕ is corrected by deducting the flux of Eqn. 3.35.

$$\phi = \phi - \phi_{pEqn} \tag{3.36}$$

A2 - Back to the outer loop

10 - pressure is under relaxed to allow for stability and convergence.

11 - Correct the cell velocities with the new pressure obtained.

$$U = U - (rAU \times \nabla P) \tag{3.37}$$

12 - Final step is to correct the turbulent quantities.

3.4.4 GMRES and Bi-Conjugate Stabilized Matrix Solver

The method in which GMRES and BiCCGStab matrix solvers will be briefly outlined here. The interested reader is referred to the source code in appendices for more detailed understanding.

GMRES

1 - Calculate initial residual.

2 - Create the Hessenberg Matrix.

3 - Allocate kyrlove space vectors.

4 - Execute preconditioning.

5 - Use Ardnoldi's method and apply preconditioning again.

6 - Apply givens rotation to columns and then to rows.

7 - Back substitue to solve Hy = b.

8 - Update solution.

BiCCGStab

1 - Calculate initial residual.

2 - Calculate transpose residual.

3 - Update search directions.

4 - Execute preconditioning.

5 - Update solution and residual.

3.4.5 Modified Baldwin-Lomax model

$$\mu_{t_{outer}} = \rho K C_{cp} F_(y) F_{KLEB(y)} \tag{3.38}$$

Function $F(y)$ in Eqn. 3.38 is the product of wall distance $Y+$, vorticity magnitude $|\Omega|$ and the Van Driest damping factor D:

$$D = \left(1 - e^{\frac{-y+}{A+}}\right) \tag{3.39}$$

The Intermittency Factor $F_{KLEB(y)}$ in Eqn. 3.40 is redefined as:

$$F_{KLEB(y)} = \left[1 + 5.5\left(\frac{yC_{KLEB}}{Y_{MAX_{REF}}}\right)^6\right]^{-1} \tag{3.40}$$

where Y_{MAX} is replaced with $Y_{MAX_{REF}}$, introduced in[22]:

$$Y_{MAX_{REF}} = \frac{L_{sep}}{L}\frac{0.03855}{Re_x} \tag{3.41}$$

The reference airfoil length L in (3.41) and parameter L_{sep} can be taken approximately equal, as proposed in[22]. The Reynolds number Re_x is given as:

$$Re_x = \frac{U_{freestream} C_{ref}}{\nu} \tag{3.42}$$

and the eddy viscosity μ_t is computed as the minimum from $\mu_{t_{inner}}$ and $\mu_{t_{outer}}$:

$$\mu_t = min\left(\mu_{t_{inner}}, \mu_{t_{outer}}\right) \tag{3.43}$$

The proposed modified BL model constants are taken as in the original BL model:

$A+$	C_{CP}	C_{KLEB}	C_{WK}	k	K
26	1.6	0.3	0.25	0.4	0.0168

3.4.6 K-Omega SST Vorticity Model

$$\frac{\partial k}{\partial t} + \frac{\partial u_j k}{\partial x_j} = (P_k - \beta^\star \omega k + \frac{\partial}{\partial x_j}\left[(\mu + \sigma_k v_t)\frac{\partial k}{\partial x_j}\right] \tag{3.44}$$

$$\frac{\partial \omega}{\partial t} + \frac{\partial u_j \omega}{\partial x_j} = \frac{\gamma}{\nu_t}(P_k - \beta\rho\omega^2 + \frac{\partial}{\partial x_j}\left[(v + \sigma_\omega v_t)\frac{\partial \omega}{\partial x_j}\right] + D \tag{3.45}$$

where Turbulent Viscosity is defined as:

$$v_t = \frac{a_1 k}{max(a_1\omega, \Omega F_2)} \tag{3.46}$$

the main difference is that the production of turbulence , P_k is defined with vorticity magnitude rather than strain rate magnitude:

$$P_k = m u_t \Omega^2 \tag{3.47}$$

3.4.7 Spalart-K-Omega Hybrid model

$$\frac{\partial k}{\partial t} + \frac{\partial u_j k}{\partial x_j} = (P_k - \beta^\star \omega k + \frac{\partial}{\partial x_j}\left[(\mu + \sigma_k v_t)\frac{\partial k}{\partial x_j}\right] \tag{3.48}$$

$$\frac{\partial \omega}{\partial t} + \frac{\partial u_j \omega}{\partial x_j} = \frac{\gamma}{\nu_t}(P_k - \beta\rho\omega^2 + \frac{\partial}{\partial x_j}\left[(v + \sigma_\omega v_t)\frac{\partial \omega}{\partial x_j}\right] + D \tag{3.49}$$

$$\frac{\partial \hat{v}}{\partial t} + u_j \frac{\partial \hat{v}}{\partial x_j} = C_{b1}(1 - f_{t2})\hat{S}\hat{v} - \left[C_{w1}.f_w - \frac{C_{b1}.f_{t2}}{\kappa^2}\right]\left(\frac{\hat{v}}{d^2}\right) + \frac{1}{\sigma}\left[\frac{\partial}{\partial x_j}(v+\hat{v})\frac{\partial \hat{v}}{\partial x_j} + C_{b2}\frac{\partial \hat{v}}{\partial x_i}\frac{\partial \hat{v}}{\partial x_i}\right] \tag{3.50}$$

and the viscosity is then calculated as:

$$\mu_t = \alpha m u_{t_{SSTmodel}} + (1 - \alpha)\mu_{t_{SSTmodel}} \tag{3.51}$$

where α is a ratio between 0 to 1(value of 0.5 will give equal contribution from both models).

3.4.8 Dynamic Mesh Solver with prescribed α change

This mesh motion method involves prescribed change in the mesh using tabulated data.

$$euler_{angles} = Amplitude(sin(\omega t)) \times \pi/180 \tag{3.52}$$

$$quarternionR = R(euler_{angles}.X, euler_{angles}.Y, euler_{angles}.Z) \tag{3.53}$$

$$septernionTR = TR(septernion(origin) \times R \times septernion(-origin)) \tag{3.54}$$

3.4.9 Need for new/modified implementations

The unsteady time marching solvers in OpenFOAM are the pisoFOAM and pimpleFOAM (relevant to the work in this Thesis). pisoFOAM is limited to a Courant number of 1 and below and pimpleFOAM can only handle Courant number below 20 (that too with at least 40-100 inner loops in every time step). Hence the transientSimpleFOAM and transientSimpleDyMFOAM implementation helps to speed up the unsteady simulations as they can handle large courant numbers (even up to 200). However, one must give enough caution to ensure that the inner iterations are converged well before moving on to the next time step. The hysteresisFOAM is a modification of the transientSimpleFOAM with more pressure information from the previous time step's flow field ensuring to keep pre-history of the motion. This helps improve the prediction of static aerodynamic hysteresis.

GMRES and BiCGStab matrix solvers described are matrix solvers that can speed up and improve convergence of the NS equation thus helping to reduce costs

of simulations. They perform much better than the usual matrix solvers implemented in OpenFOAM and has not been included in the source codes provided. Thus coding them and implementing them helped to reduce the time taken to study the hysteresis phenomena.

Some turbulence models such as Baldwin-Lomax model are not included in the OpenFOAM source code, mostly because it is an algebraic model. Hence coding of this model was difficult, as OpenFOAM turbulence models are designed to solve Partial Differential equations. This simple, robust model can quickly produce accurate results is the early design stages of aircraft.

Hence, every implementation that was carried out as work of this Thesis had a particular impact and use, either in speeding up the simulations or ensuring accuracy of the simulation is improved.

Chapter 4

Aerodynamic Stall Hysteresis

A major focus of this Thesis is investigating and improving the capture of the aerodynamic static hysteresis loops using computational tools available within the open source CFD code OpenFOAM. As mentioned before, static hysteresis loops are difficult to capture accurately using experimental and computational methods due to the sensitivity of these loops to various factors. In computational simulations, the static stall hysteresis loops are sensitive to the numerical grid, setup, turbulence model, etc. Firstly in this chapter, a thorough review of the experimental results obtained for static hysteresis is presented with comments on the differences for the results in aerodynamic loads amongst various wind tunnel tests for the same flow conditions. Following the experimental results section, the computational results obtained using OpenFOAM simulations is presented for both low and high Reynolds number flow conditions and the challenges faced in acquiring accurate hysteresis loops are discussed.

It is important to differentiate static hysteresis phenomena that happens due to onset and burst of laminar bubbles which exist at low Reynolds numbers from the massive static hysteresis phenomena that exists due to transition from the trailing edge separation to fully separated flow condition. The later can exist in combination with laminar bubbles at low Reynolds numbers and also at high Reynolds number when laminar bubble practically disappear [23, 24]. In [24] experimental results shows existence of static hysteresis at $Re = 5million$ where there is no laminar bubble in the pressure or suction side for a thin airfoil i.e. TsAGI-9140.

It is also important to note that the experimental results and CFD results related to extended flight envelope problems involving largely separated flows are extremely sensitive to the flow conditions and setup of the evaluation procedure. Results in paper [3] show significant difference between CFD prediction of the aerodynamic auto-rotation effect at stall conditions versus similar results obtained in wind tunnel tests. This indicates sensitivity of stall aerodynamics to various testing conditions such as interference, test model vibrations, level of turbulence, etc. One can expect similar sensitivities in investigation of the static aerodynamic hysteresis.

There are many experimental results indicating the existence of static hysteresis. In [25] the effect of laminar bubble on a cambered airfoil i.e. Lisamann airfoil,

at $Re = 150,000$ was considered and reverse hysteresis loops were found out. The smoke visualization proves the unsteadiness and large separation regions in the flow when the airfoil is in hysteresis (see Fig. 4.1)

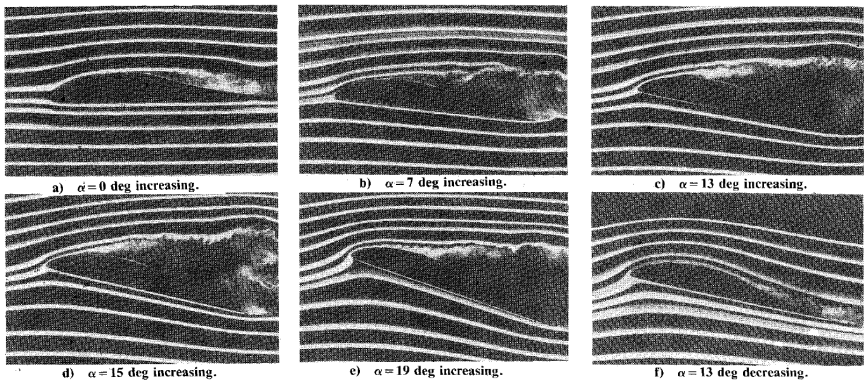

Fig. 4.1: Smoke visualization of static hysteresis for Lisamann airfoil presented in [25].

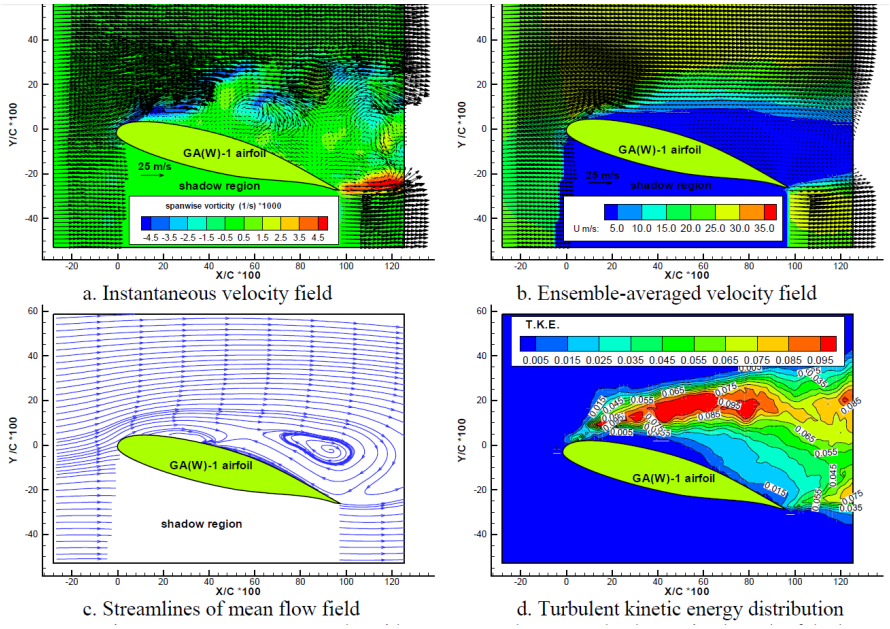

Fig. 4.2: PIV visualization of $\alpha = 14°$ return branch from [26].

PIV measurements can also produce useful visualizations to indicate the existence of static hysteresis. PIV measurement results in the case of hysteresis associated with General Aviation(GA) airfoil was presented in [26]. The visualization of velocity field, streamlines and turbulent kinetic energy distribution for $\alpha = 14°$ of the bottom branch of hysteresis is shown in Fig. 4.2.

Among aerodynamic hysteresis results published in the public domain, the work of W.A. Timmer [27] is remarkable. The presented study in [27] shows wind tunnel results for NACA 0018 airfoil at from a Reynolds number in the range of $0.15 - 1 \times 10^6$ (see Fig. 4.3).

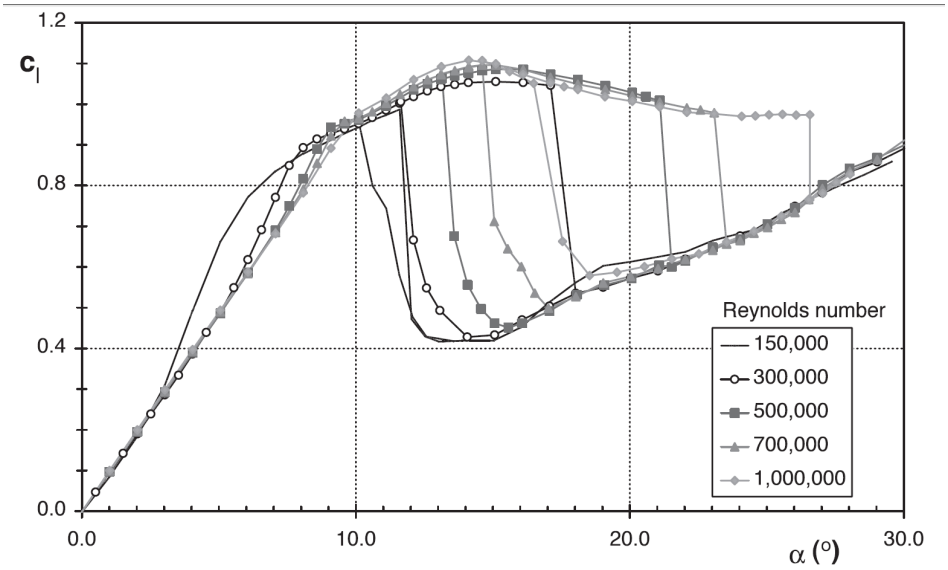

Fig. 4.3: Wind tunnel test results for NACA 0018 airfoil in static hysteresis reported in [27].

The static hysteresis process is very sensitive to the flow conditions. Hoffmann [28] investigated the static hysteresis in flow past NACA 0015 finite aspect ratio wing and showed that with the increase in turbulence intensity the hysteresis loops disappear accompanied with the increase of $C_{L_{max}}$(see Fig.4.4).

In close association with Hoffman's results the work in [29] also shows that aerodynamic hysteresis loops are affected with modification of the aspect ratio of the wing. Also, the level of noise in the wind tunnel can lead to shrinking of the hysteresis loops as demonstrated in [30]

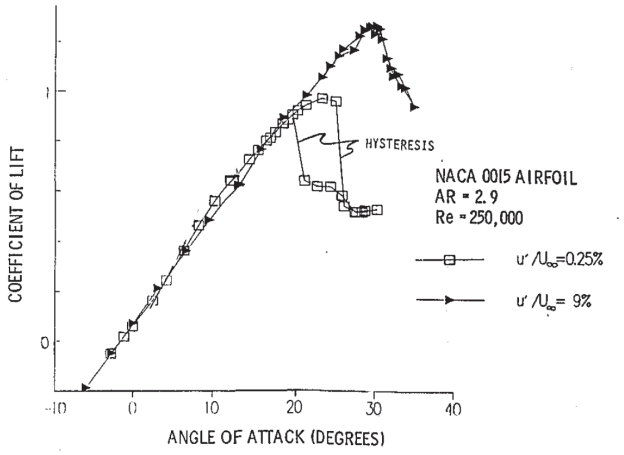

Fig. 4.4: Static hysteresis for NACA 0015 wing presented in [28].

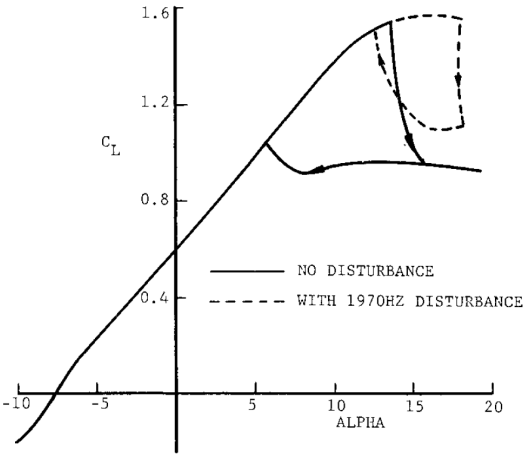

Fig. 4.5: Shrinking of hysteresis loop due to wind tunnel noise presented in [30].

Noticeably, there are only few computational results presented in static hysteresis. The work of Sanjay Mittal and Priyank Saxena in [4] is remarkable and is the first attempt to capture static hysteresis using CFD methods. The work in [4] was carried out using NACA 0012 airfoil at $Re = 1 \times 10^6$ and Finite Element Method(FEM) with a special stabilization approach. Using this approach, a 1.5 degree wide static hysteresis loop was found where the lower branch had much lower lift coefficient value. The lower branch of static hysteresis loop was also accompanied with much larger vortex shedding and higher unsteadiness in the flow. The results for this work is shown in Fig. 4.6.

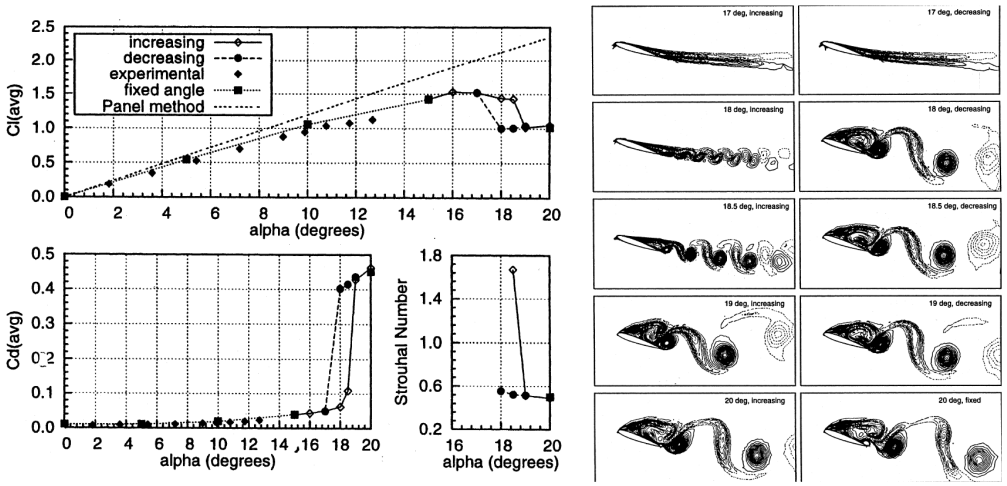

Fig. 4.6: CFD simulation of static hysteresis past NACA 0012 airfoil from [4].

Another recent publication in static hysteresis presented in [31] was carried out using a non symmetric airfoil in the transonic flow regime. The static hysteresis in this case is closely related to the shock wave found on the top surface of the airfoil. The flow visualization for the lower branch of static hysteresis(pitch down)

at 7 degrees demonstrated a slightly bigger flow separation zone as shown in Fig. 4.7.

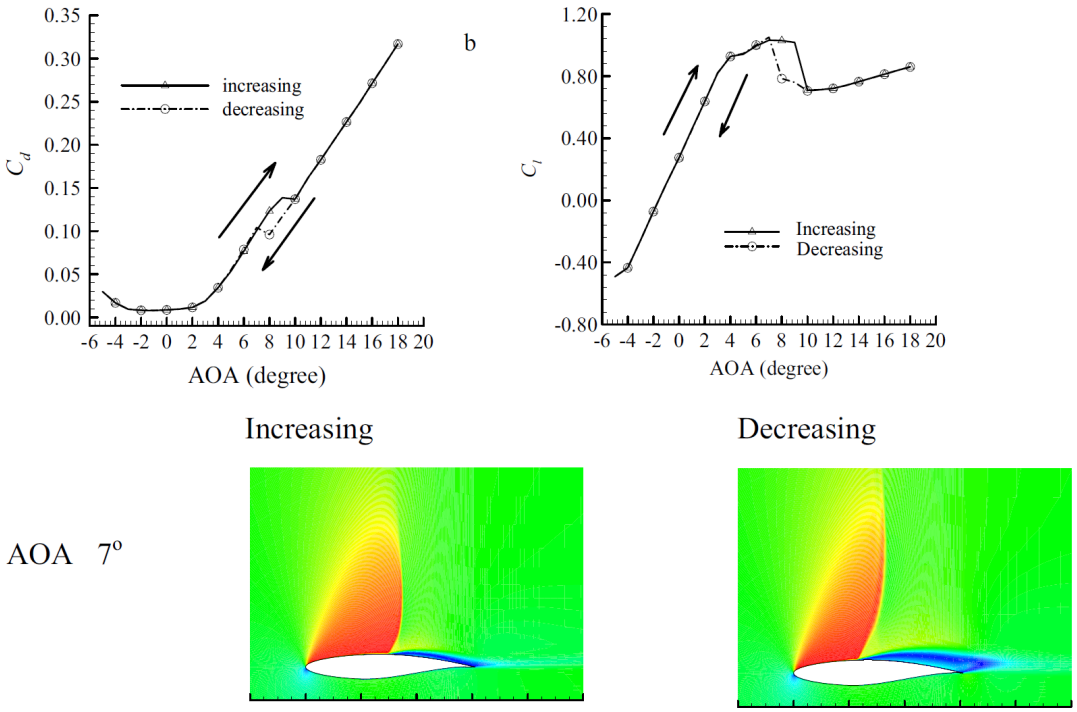

Fig. 4.7: Computational simulation of static hysteresis in the transonic flow regime from [31].

Empirical methods are also useful in analysis of static and dynamic hysteresis. A semi empirical method to capture the static hysteresis loops are presented in [32]. The results are discussed in terms of the thickness of the airfoil and turbulent intensity and shows reasonably accurate predictions. The lift coefficient values obtained for various airfoils at different turbulence intensities are shown in Fig. 4.8.

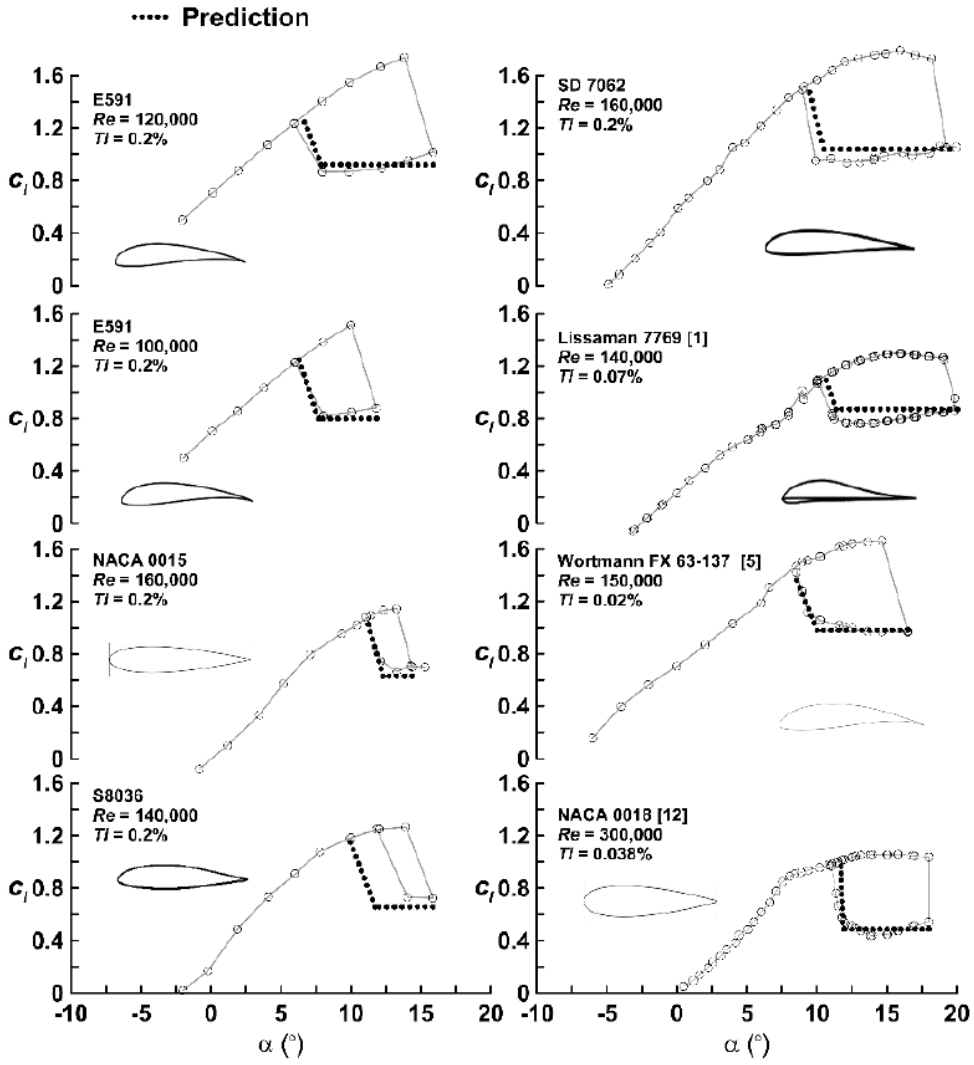

Fig. 4.8: Semi empirical prediction model for static hysteresis from [32].

Dynamic hysteresis results are more frequently published in literature than static hysteresis results. There exists many experimental and computational proof of dynamic hysteresis past airfoils, wings and aircraft. In [33] the NASA's common research model (CRM) was used to find the dynamic hysteresis in the lift coefficient values at different reduced frequencies(k). The results demonstrated that with increasing k values the hysteresis loop expands quite significantly (see Fig. 4.9.)

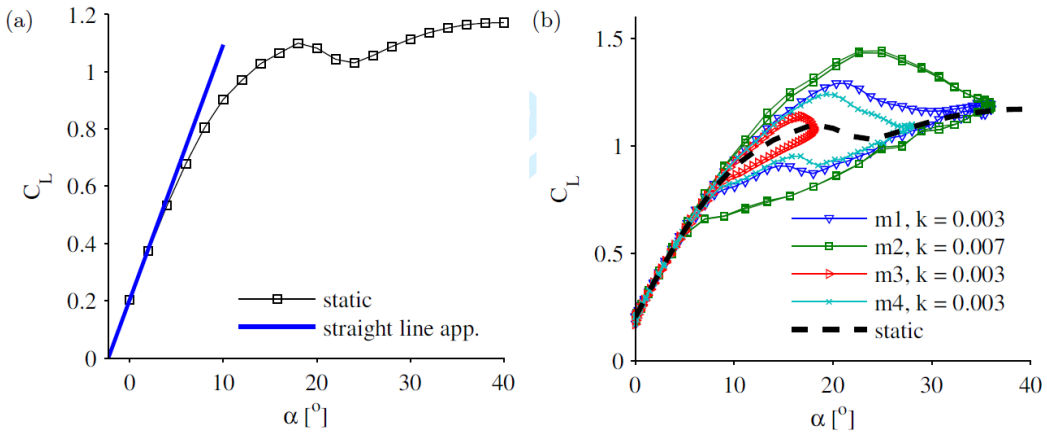

Fig. 4.9: Dynamic Hysteresis loops in flow past CRM aircraft model from [33].

Since the dynamic hysteresis involves large amplitude oscillations at high angles of attack and mesh morphing methods , low order models (LOM) are developed in order to reduce the cost of using CFD or experimental methods to capture the dynamic hysteresis loops. The work in [34] presents a low order modeling approach for dynamic hysteresis using indical methods and the acquired results in Fig. 4.10 shows that the the implemented Low order model performs well in comparison to CFD simulation. The visualizations for the development of the unsteady vortices in dynamic hysteresis are shown Fig. 4.11.

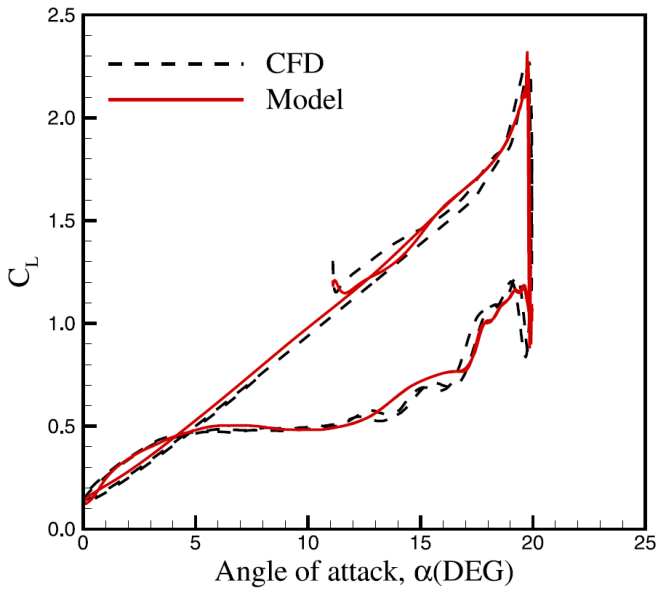

Fig. 4.10: Low order modelling of dynamic hysteresis from [34].

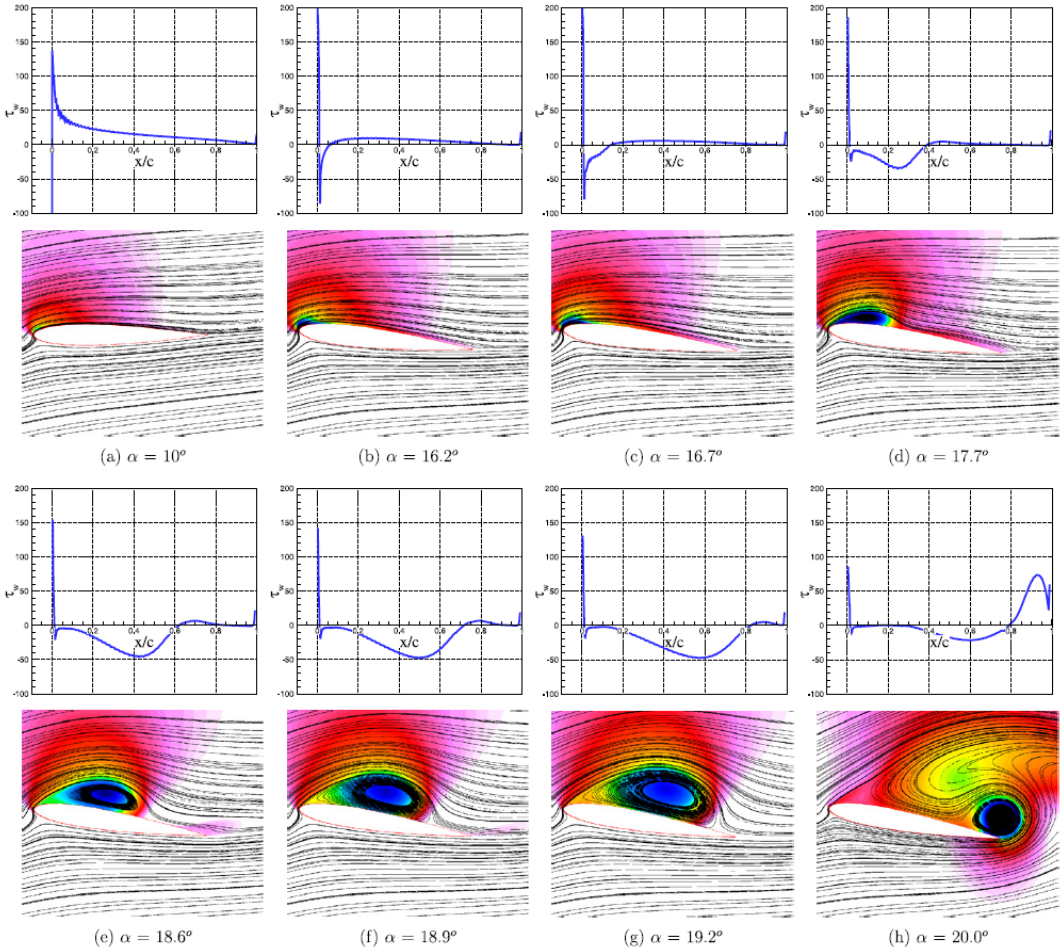

Fig. 4.11: Visualization of results of dynamic hysteresis from [34].

There also exists various other published results in dynamic hysteresis and the interested reader is referred to [35–40]. There are also results published in close context to dynamic hysteresis which involves solid body motion such as flapping wings and the results for a flapping wing motion predicted using Lattice Boltzmann methods presented in [41] are shown in Fig. 4.12.

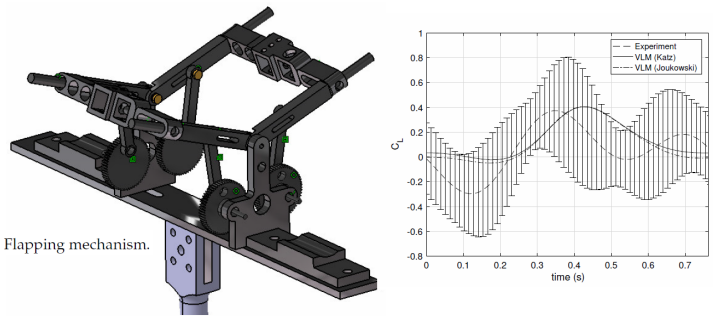

Fig. 4.12: Flapping wing aerodynamics predicted by Lattice Boltzmann methods from [41].

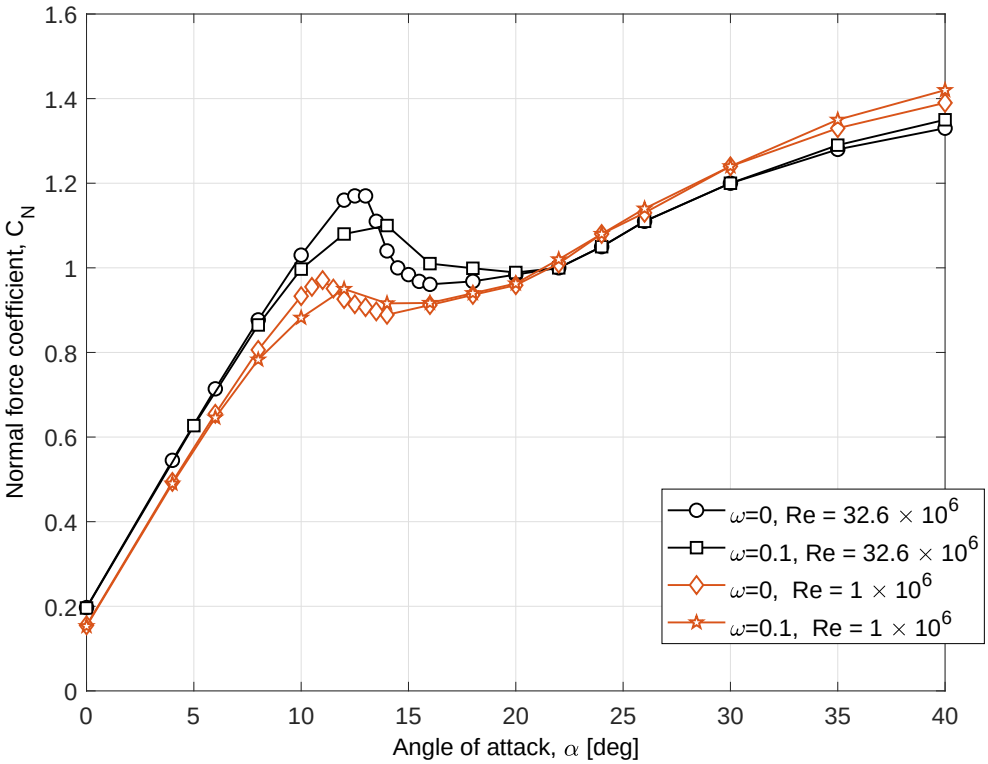

Fig. 4.13: Normal force coefficient from [42].

Fig. 4.13 and 4.14 shows obtained results from [42] for normal force coefficient and pitching moment obtained through simulations for common research model with and without dynamic motion. The results in Fig. 4.13 shows that increase of the Reynolds number from 1 to 32 million leads to an increase of $C_{L_{max}}$ from roughly about 1 to 1.2 and delays the stall angle by 2 degrees. Furthermore an increase of ω, which is the non-dimensional angular velocity, from 0 to 0.1 leads to a slight delay in stall angle but also causes a slight decrease in maximum lift coefficient, $C_{L_{max}}$. The original intent in the work presented in [42] is to find out the regions of auto-rotation in the pre/post- stall region. Fig. 4.14 shows that there is a sharp increase in pitching moment around 12 degrees for the cases with $\omega = 0.1$ indicating existence of auto-rotation regime.

The increase of maximum lift coefficient when Reynolds number is increased accompanied with a deep and sharp stall might indicate existence of static hysteresis. However, the work conducted in [42] have no testing for static hysteresis and therefore the shown results do not demonstrate existence of the hysteresis loops.

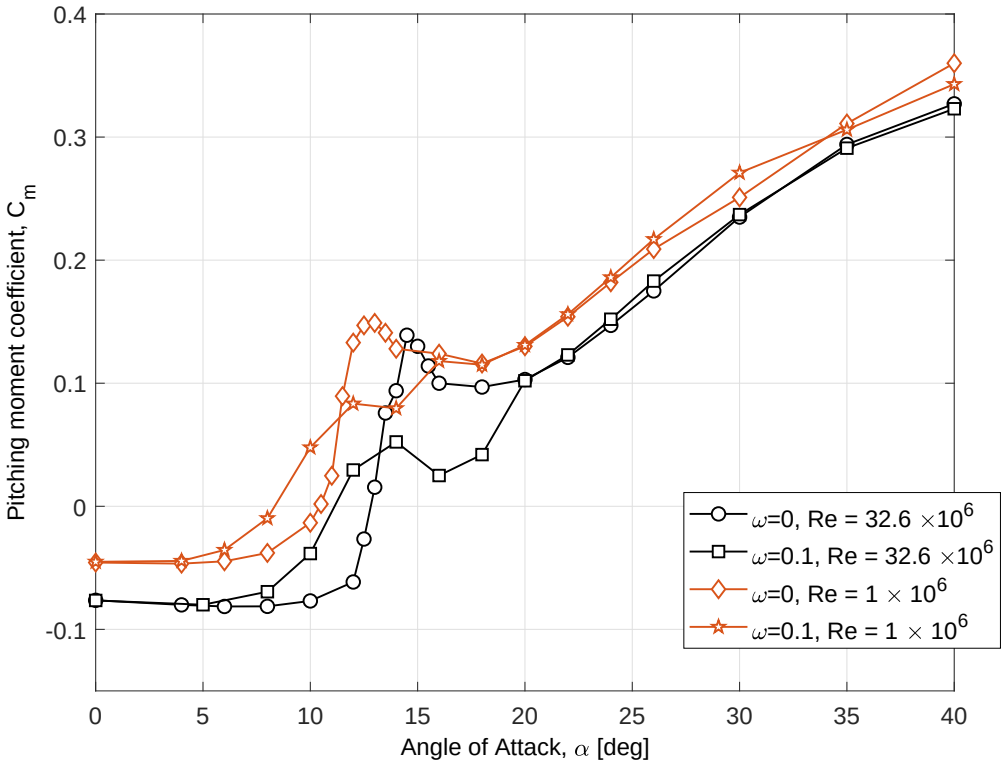

Fig. 4.14: Pitching moment coefficient from [42].

4.1 Experimental results

Static Stall Hysteresis loops in Wind tunnel tests have been investigated by various researchers. In this section the experimental results will be presented in two categories i.e. Low and High Reynolds number flow conditions.

4.1.1 NACA 0018 at Low Reynolds Flow conditions

Experimental investigation of the aerodynamic hysteresis at stall conditions for the NACA0018 airfoil was carried out in the low-turbulence TsAGI T-124 wind tunnel [43]. The wing model has a chord of $0.24m$ and a span of $1m$, which is equal to the width of wind tunnel closed working section (Fig.4.15, left). The level of turbulence of wind tunnel air flow was less than 0.05% at air speed $V = 40m/s$. Dynamic rig OVP-124 allows measuring the lift and drag forces, X_a, Y_a, along the air flow and in orthogonal to flow direction, and also the pitching moment M_z (Fig.4.15, right). The test measurements can be conducted with fixed angle of attack α, continuous sweep movement $\alpha(t)$ and in forced oscillations $\alpha(t) = \alpha_0 + \alpha_s \sin(2\pi f t)$, which can be conducted with different amplitudes ($\alpha_s \leq 20^0$) and frequencies of oscillation ($f \leq 5Hz$) by changing the crank radius and DC motor speed. The straight wing is mounted in bearings on the left and right end of its installation and its rotation is forced with a lever arm of radius r. The reaction forces F, X_R, Y_R, X_L, Y_L are

measured from three strain guages slip rings inside two bearings and the lever arm. These measurements allow calculation of the lift and drag forces and also pitching moment:

$$\begin{aligned} X_a &= X_R + X_L + F\sin(\alpha) \\ Y_a &= Y_R + Y_L - F\cos(\alpha) \\ M_z &= Fr \end{aligned} \tag{4.1}$$

and the lift, drag and pitching moment coefficients $C_L(\alpha), C_D(\alpha), C_m(\alpha)$.

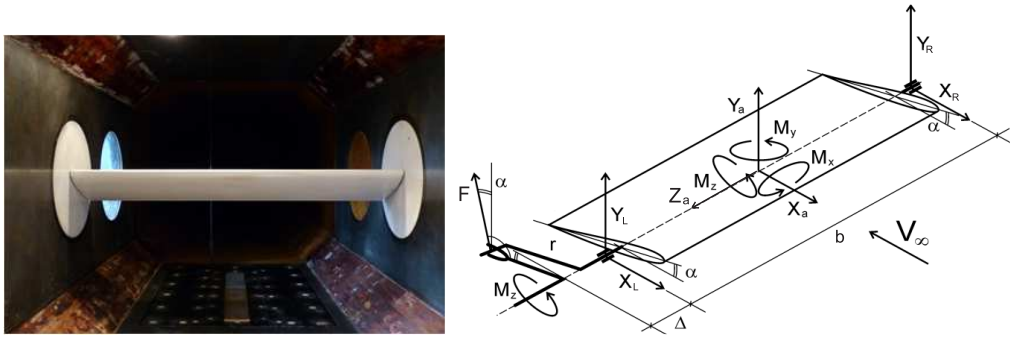

Fig. 4.15: Straight wing with NACA-0018 airfoil fitted in the low-turbulence TsAGI T-124 wind tunnel (left plot), Force balancing scheme for measuring aerodynamic loads (right plot).

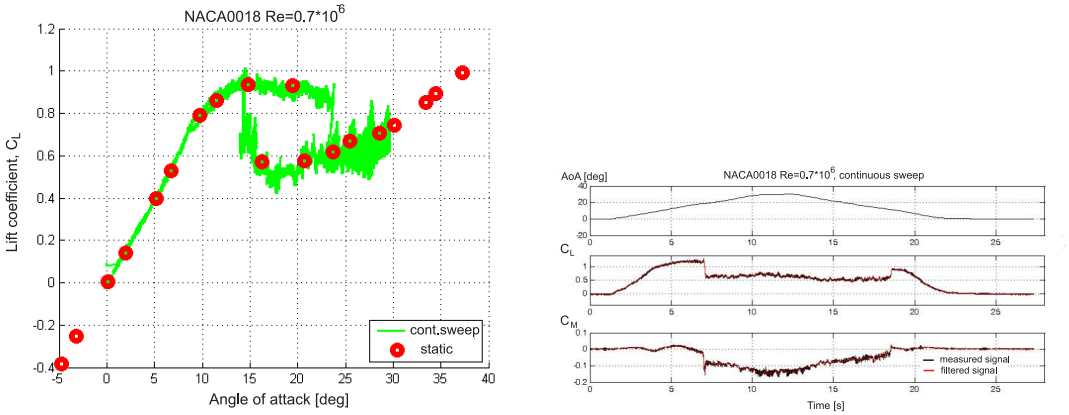

Fig. 4.16: Dependence of the NACA0018 wing lift coefficient on angle of attack from static tests and continuous sweep motion (left), the angle of attack, lift and pitching moment coefficients time dependencies in continuous sweep motion (right). $V = 40m/s, Re = 700,000$.

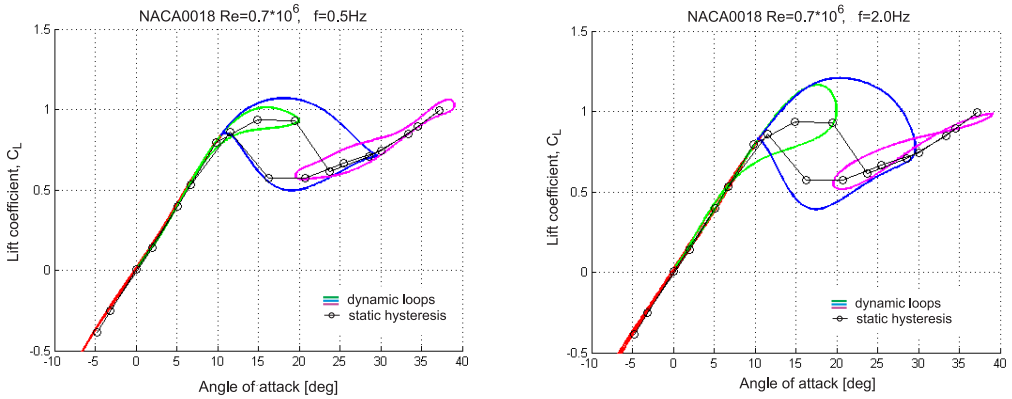

Fig. 4.17: Dynamic loops in the NACA0018 wing lift coefficient during periodic changes of angle of attack with different amplitudes and frequencies: $f = 0.5Hz$ on the left, $f = 2.0Hz$ on the right. $V = 40m/s, Re = 700,000$.

The wind tunnel tests results for $V = 40$m/s ($Re = 0.7 * 10^6$) are presented in Figs.4.16 and 4.17. On the left plot of Fig.4.16 the lift coefficient dependence on angle of attack from static tests (red circles between $\alpha = -5^0$ and $\alpha = 37^0$) and measured in continuous slow sweep motion (green lines between $\alpha = 0$ and $\alpha = 30^0$) clearly show the existence of static hysteresis with two different branches for pitch-up and pitch-down angle of attack variation. The measured lift and pitching moment from continuous sweep variation of angle of attack are shown on the right plot of Fig.4.16 as functions of time. The static test points are calculated as averaged values of the measured aerodynamic load over some finite time interval, while the measured loads from continuous sweep motion are plotted directly without averaging and filtering.

The flow separation starts approximately at $\alpha = 10^0$, which is indicated by decline from the initial linear increase of the lift coefficient. High frequency variations in the measured lift and pitching moment (moderate amplitude at the higher branch of static hysteresis and increased amplitude at the lower branch of static hysteresis) are most likely connected with shedding of vortices having a positive or negative feedback effect on aerodynamic loading. The time dependencies on the right plot of Fig.4.16 show that the transitions between two branches of static hysteresis have abrupt and practically instantaneous nature probably reflecting the changes in structure of separated flow.

Fig. 4.17 shows the aerodynamic responses for the lift coefficient measured in forced oscillation tests with mean values of angle of attack $\alpha_0 = 10^0, 20^0, 30^0$ and amplitude $\alpha_s = 10^0$, which were averaged over a number of periods, smoothed and plotted on the graph against angle of attack for two different frequencies - $f = 0.5Hz$ (left plot) and $f = 2.0Hz$ (right plot). The dynamic loops marked by green and magenta lines belong to the top and the bottom branches of static hysteresis, respectively. The dynamic loops marked by blue lines are surrounding the observed static hysteresis and therefore transiting through regions with two different separating flow structures. The increase of frequency of oscillation expands dynamic loop on the top branch of static hysteresis (green lines) and dynamic loop surrounding static hysteresis loop (blue lines), but their growth is bounded

by two boundaries, which correspond to the existence of different flow structure. One can reason that the upper part of dynamic loop is saturated by dependence of the lift coefficient corresponding to attached flow conditions and the bottom part of dynamic loop is saturated by the lift coefficient dependence corresponding to fully separated flow conditions. As a result the dynamic loops surrounding static hysteresis increase variation in the lift coefficient and include segments with extended to higher attitudes attached flow and to lower attitudes fully separated flow conditions. These two segments are separated by two segments with transitional flow structures. To better understand the flow transformations in static conditions and during airfoil's forced oscillations in stall region flow simulations using computational fluid dynamics methods are discussed in the following section.

4.1.2 Phenomenological bifurcation model of static hysteresis

Reduced order model for simulation of aerodynamic responses at the presence of static hysteresis can be developed with inclusion of its bifurcation properties. The state-space aerodynamic model for dynamic hysteresis accounting for flow transient processes proposed in [44]

$$\begin{aligned} C_L &= C_L(\alpha, x) \\ \tau_1 \frac{dx}{dt} + x &= x_0(\alpha - \tau_2 \dot{\alpha}) \end{aligned} \tag{4.2}$$

was modified in [35] by introduction of a two-valued function for position of flow separation point $x_{0_\pm}$ depending on angle of attack α and its rate of change $\dot{\alpha}$ in static conditions. This modification allows modeling aerodynamic responses at large amplitude oscillations covering hysteresis loop, but may fail to match behavior at critical states crossing and action of external disturbances. To capture these properties in [45] was proposed a nonlinear differential equation for variable x inherently possessing bifurcation properties of static hysteresis, which include variation of characteristic time scale in proximity of bifurcation points and separation of regions of attraction for the upper and lower branches of static hysteresis. Here just a general idea of this approach is briefly outlined. The linear differential equation from (4.2) is replaced by the following nonlinear equation in the form of cubic polynomial with respect to relative deviation of variable x from its static position x_0:

$$\frac{dx}{dt} = G(x, \alpha, \dot{\alpha}) = k_1(\alpha)(x_0 - x) + k_2(\alpha)(x_0 - x)^2 + k_3(\alpha)(x_0 - x)^3 \tag{4.3}$$

where $k_1 = 1/\tau_1$ and x_0 depends on shifted argument $\alpha_s = \alpha - \tau_2 \dot{\alpha}$.

The modified model (4.2),(4.3) intrinsically possesses the properties required for modelling aerodynamic responses with static hysteresis, i.e. following the static hysteresis branches at slow variation of angle of attack in pitch-up/pitch-down motions with abrupt jumps from one branch to another in bifurcation points, showing a higher time lag during critical states crossings, and separating domains

of attraction for upper and lower branches of static hysteresis, the latter property is responsible for the model sensitivity to external disturbance in proximity of bifurcation points making the static hysteresis loop width dependent on the level of turbulence and the wing structural vibrations in wind tunnel tests.

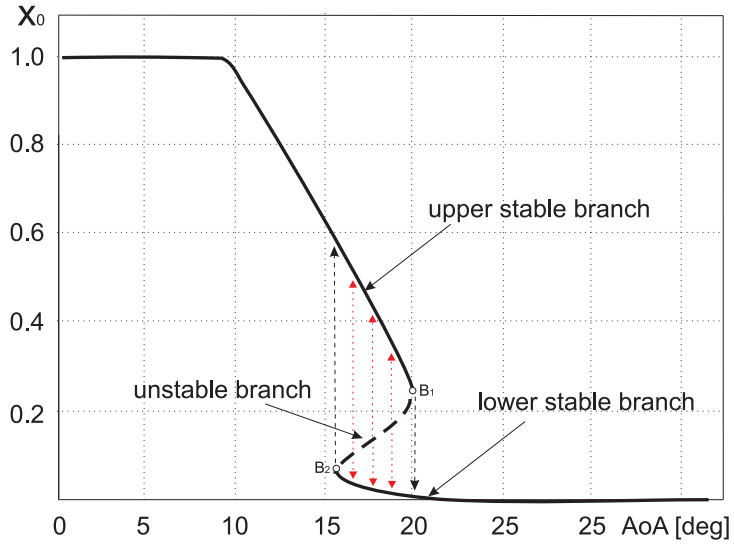

Fig. 4.18: Bifurcation model of static hysteresis with two stable branches separated by unstable branch.

The identification of functions $k_i(\alpha), i = 1, 2, 3$ in (4.3) requires use of various experimental data, for example shape of stable hysteresis loop branches, unsteady aerodynamic derivatives from forced oscillation tests with small amplitudes measured on both branches of static hysteresis and also aerodynamic responses from forced oscillation tests with large amplitudes with critical states crossing covering static hysteresis loop [45]. Fig.4.18 shows two stable branches of static hysteresis smoothly connected by one unstable branch, which plays a role of a separatrix dividing regions of attraction for two stable branches of stable hysteresis (see red transition arrows). The continuous curve of stable and unstable branches of static hysteresis shown in Fig.4.18 is defined by the following condition:

$$G(x, \alpha_s) = 0 \tag{4.4}$$

In nonlinear system (4.3) the effective local time scale on a stable branch is inversely proportional to the partial derivative $\tau_1 = 1/\left(\frac{\partial G}{\partial x}\right)\|_{G=0}$, calculated in a point belonging to the branch. In regular points on stable branches the characteristic time scale in the linearised model (4.2) is defined as $\tau_1(\alpha) = 1/k_1(\alpha)$, while in close proximity of bifurcation points B_1, B_2 the characteristic time scale is approaching infinity $\tau_1 \to \infty$, which slows down transitions from critical states B_1 and B_2 to the opposite branch. The proposed nonlinear transformation of model (4.2) has been successfully validated on experimental data with static hysteresis for NACA0018 wing with aspect ratio $A = 5$, and the modelling results can be found in [45].

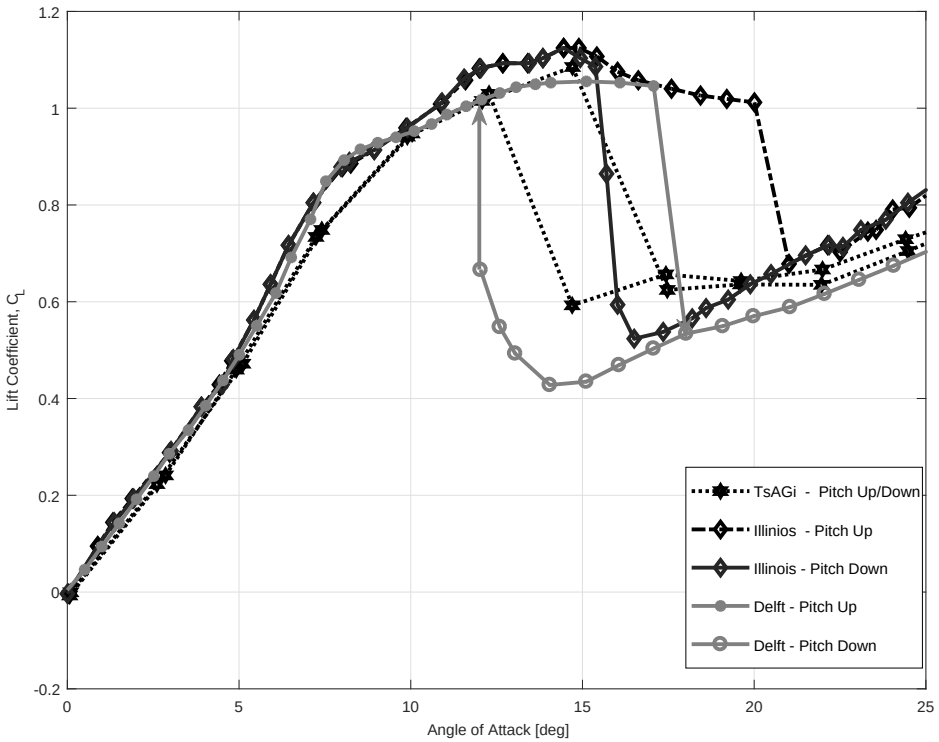

Fig. 4.19: Comparison of experimental results from different sources for $Re = 300k$.

Fig. 4.19 shows crucial results which could be used to compare and discuss the differences in the aerodynamic loads for the same Reynolds number of 300,000. The only possible differences in the experiment are the aspect ratios of the wing used and the level of turbulence/noise in the wind tunnel. The results from delft (solid-grey-circle) shows early and sharp stall at 18 degrees angle of attack. Hysteresis dominates and keeps the lift coefficient below 0.6 up until the return to 12.5 degrees. Results from TsAGI (dotted-grey-hexagram) shows a much narrower hysteresis loop of about just 2-3 degrees and higher lift coefficient in stalled conditions compared to results from Delft and Illionis. The results from Illionois shows a much later stall (at 20 degrees) also with higher maximum lift coefficient than Delft and TsAGi. However, this is accompanied by an early return to the top branch of static hysteresis loop at about 16 degrees. The differences in the experimental results for the same flow Reynolds number in wind tunnels from three different reliable institutions represents how complicated and sensitive static hysteresis results can be to acquire accurately. Therefore, it is our ultimate interest to find out what factors effect the static hysteresis results most and in what extent.

4.1.3 TsAGi-9140 Airfoil at Moderately High Reynolds Flow conditions

In the mid 40's, in the period preceding to the era of supersonic flight, it was quite natural to model the aerodynamics of thin wings, which are suitable for supersonic flight. However, the thin wings caused stall at low angles of attack posing a problem for take-off and landing. To address this problem of the finite aspect ratio rectangular wing $AR = 5$ with TsAGI-9140 airfoil, maximum thickness 9% at 40% chord, was tested in the variable-density transonic wind tunnel T-106 at the Central Aerohydrodynamic Institute (TsAGI), Russia [46] at the following test conditions: $M = 0.15 - 0.45$ in the range of Reynolds numbers $Re \approx (1 - 5) \times 10^6$ and pressure $p = (1 - 6)$ atm. The considered non symmetric TsAGI-9140 airfoil is shown in Fig.4.20 along with a table of the airfoil coordinates. The modifications of the leading edge curvature in the form of small tangent to the leading edge circles (1%, 1.5% and 2%) are shown in Fig.4.21.

x%	0.25	0.50	1.0	2.0	3.0	5.0	7.5	10	15	20	30	40	50	60	70	80	90	95	100
y+%	0.501	0.705	0.992	1.385	1.703	2.216	2.731	3.177	3.891	4.432	5.170	5.470	5.425	5.037	4.285	3.127	1.706	0.923	0
y-%	0.489	0.615	0.832	1.105	1.313	1.646	1.963	2.241	2.671	2.992	3.410	3.530	3.425	3.117	2.525	1.687	0.770	0.353	0

Fig. 4.20: The TsAGI-9140 airfoil geometry. [46]

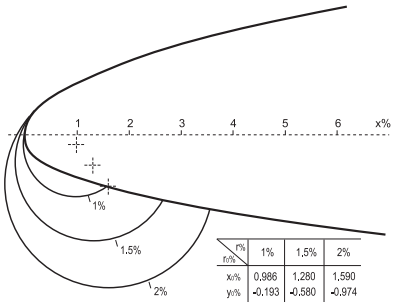

Fig. 4.21: Considered leading edge modifications for the TsAGI-9140 airfoil. [46]

The lift coefficient dependencies for the rectangular wing ($AR = 5$) in the clean and modified configurations, obtained in the wind tunnel tests, are presented in Fig. 4.22. The test results were obtained at $M = 0.15$ and $Re \approx 5 \times 10^6$. The flow separation on the clean wing occurs at $\alpha_s = 13^\circ$ and $C_L = 1.0$ (diamond markers in Fig.4.22). Below this angle $\alpha < \alpha_s$ there is no difference in the lift force dependence for the all tested wings The fully developed stall reduces the lift coefficient on the clean wing to $C_L \approx 0.85$.

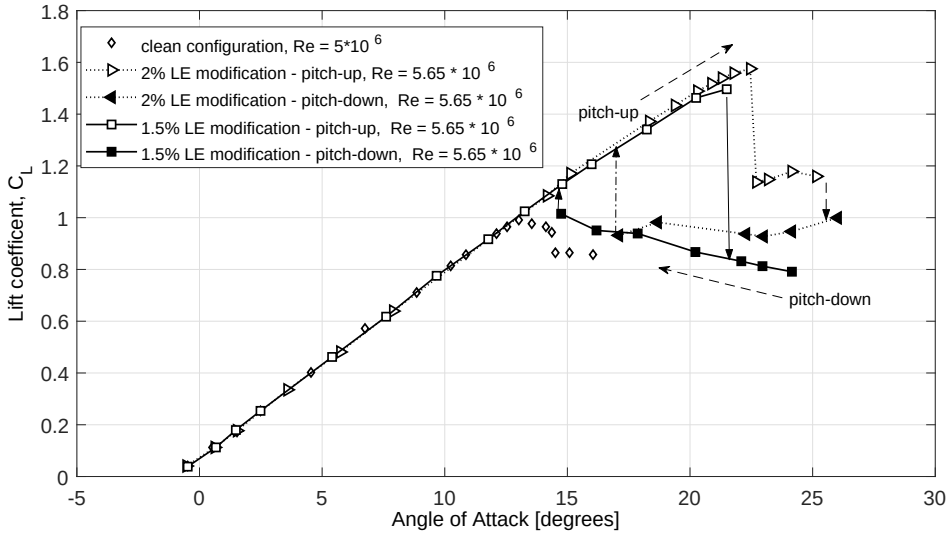

Fig. 4.22: The lift coefficient for the clean and modified TsAGI-9140 airfoils ($M = 0.15$, $Re \approx 5 \times 10^6$) [46].

The leading edge modifications, 1.5% and 2% tangent circles, causes delay in the stall angle and generate significant increase in the maximum lift coefficient, $\alpha_s = 21.5°$, $\Delta C_{L_{max}} \approx 0.5$ and $\alpha_s = 22.45°$, $\Delta C_{l_{max}} \approx 0.6$, respectively. An important feature is that the increase in the maximum lift coefficient is accompanied with the appearance of strong static hysteresis-type dependencies. The aerodynamic loads with increasing angle of attack (pitch-up motion), differ significantly from the aerodynamic loads with decreasing angle of attack (pitch-down motion). The width of the hysteresis loops and the maximum lift coefficient are growing with the increase of the Reynolds number from $Re = 1 \times 10^6$ to $Re = 5 \times 10^6$. When tested at higher Mach numbers $M = 0.3 - 0.45$ with the same Reynolds number $Re = 5 \times 10^6$ the static hysteresis loops and the increase in the maximum lift have practically disappeared. The latter effect is not considered in this research and needs special investigation.

4.2 Static hysteresis in flow past Hawk Model

Fig. 4.23 shows the 2-DOF configuration for the 1/16th scaled approximate Hawk Model which was tested for the static hysteresis in the work presented in [47]. The rig used in the experiment had a 6-DOF configuration with special controls to the rig stability and vibrational sensitivity. The model was tested for aerodynamic perfomance through various flight movements such as pitching, rolling, yawing.

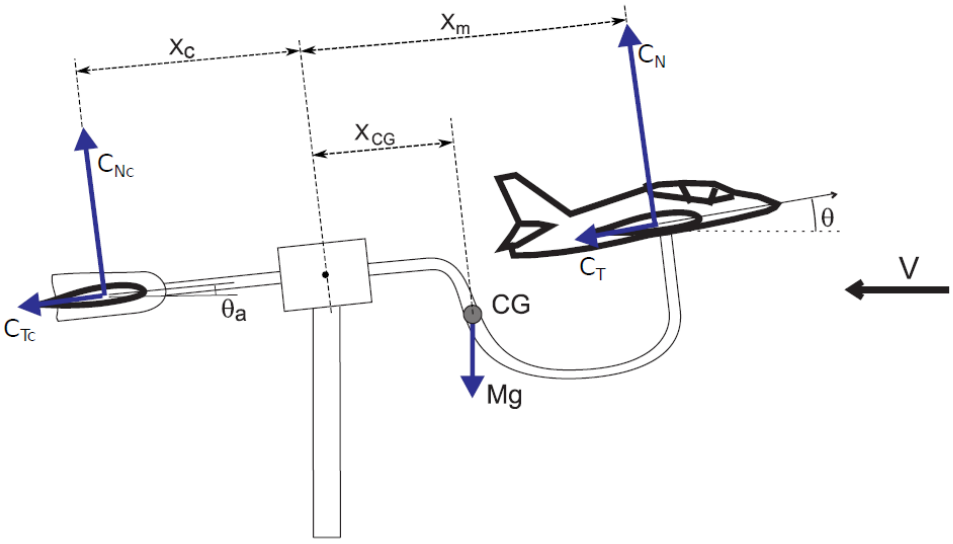

Fig. 4.23: Rig configuration, 2DOF - approx Hawk model. [47]

The obtained results indicated static hysteresis in lift force (see Fig. 4.24 and 4.25). The lift force variation in the upper and lower branch of static hysteresis loops is quite significant indicating the presence of different flow structures at the same angle of attack.The rig arm pitch angle Θ_a is proportional to C_L.

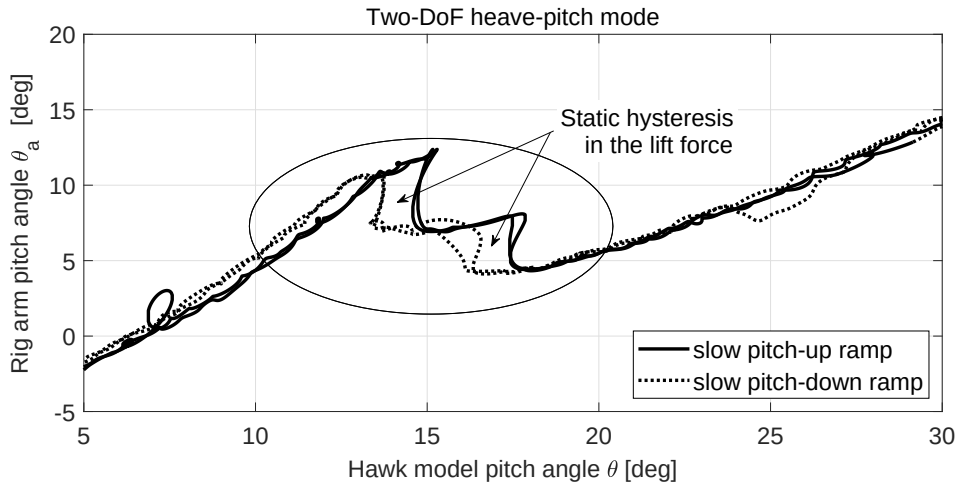

Fig. 4.24: Static hysteresis in lift force measured in rig arm pitch angle for Hawk Model. [47]

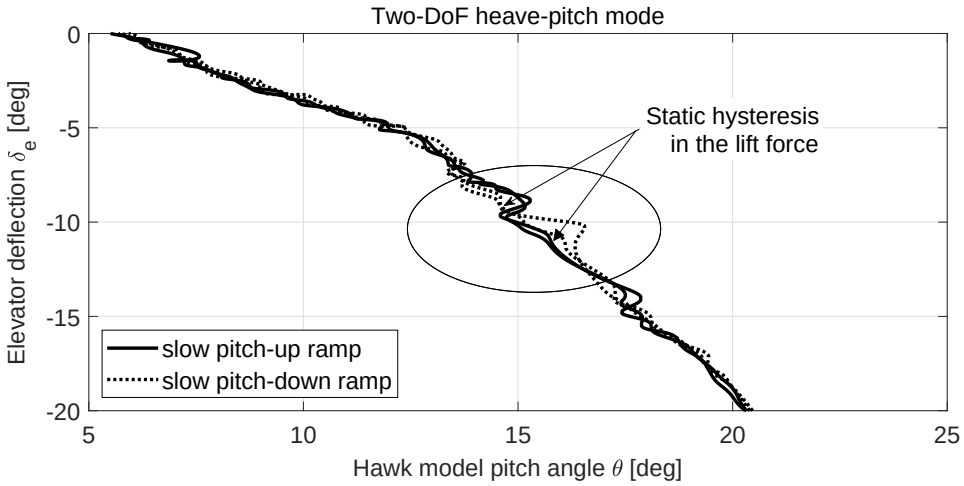

Fig. 4.25: Static hysteresis in lift force measured in elevator deflection angle for Hawk Model.[47]

Apart from the static hysteresis in the lift force, the work presented in [47] also shows static hysteresis in the roll and yaw moment coefficients as shown in Fig. 4.26 indicated in terms of roll angle. The micro asymmetry in the Hawk model leads to evolution of huge static hysteresis loops in roll, yaw and lift coefficient and therefore adds more solid proof to the experimental evidence of presence of multiple-bifurcated solutions for the same flow angle of attack.

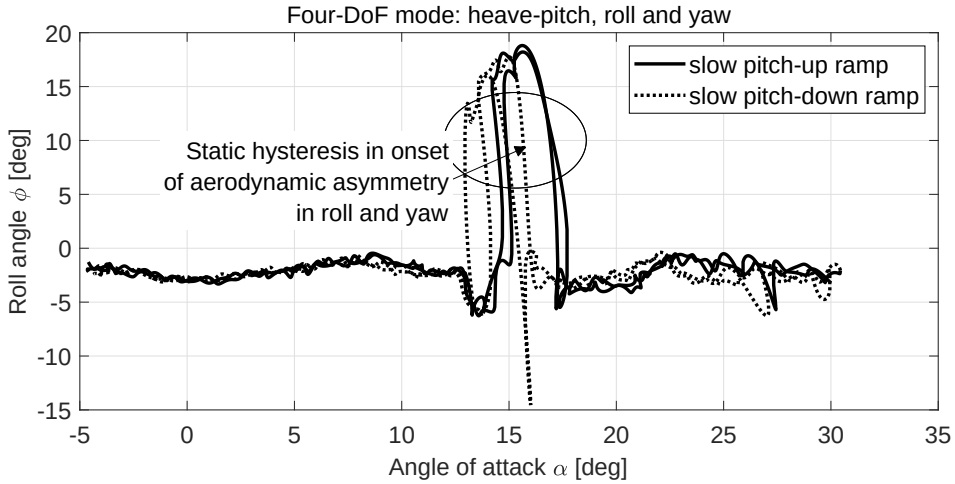

Fig. 4.26: Static hysteresis in onset of aerodynamic asymmetry in roll and yaw for Hawk Model.[47]

4.3 Computational Results

In this section, the results for the computational simulations using OpenFOAM is presented for both Low and High Reynolds flow conditions. The results are discussed in detail in relation to how turbulence models and its parameters affect the accuracy of capture of the static hysteresis loops.

4.3.1 NACA 0012 at Low Reynolds Flow conditions using Modified Baldwin Lomax turbulence model

The first successful computational prediction of static hysteresis phenomenon was made by Mittal and Saxena in [4]. The authors considered NACA 0012 airfoil at $Re = 1 * 10^6$ using the finite element formulation for solving the Reynolds Averaged Navier-Stokes (RANS) equations with the Baldwin-Lomax turbulence model in conjunction with a special stabilization scheme, the Streamline-Upwind/Petrov-Galerkin (SUPG) numerical method. The main purpose of SUPG is to eliminate numerically induced spurious oscillations in flow parameters with high frequencies, which is specific to flow conditions with high Reynolds numbers and convection dominated problems. The scheme introduces an artificial diffusion in the streamline direction, along with enforcing consistency of the solution to satisfy mass, momentum and energy conservation [48, 49].

The results from [4] in comparison with the available wind tunnel data are shown on the top plot of Fig. 4.27. The experimental data for the lift coefficient of the NACA 0012 airfoil from [50] obtained at $Re = 1.8 * 10^6$ and $Re = 6 * 10^6$ are shown with filled open diamond and filled square markers, respectively. One can notice, that the increase of the Reynolds number leads to increase of the lift coefficient slope, C_{L_α}, at low angles of attack $\alpha < 10^\circ$. There is also noticeable delay in the start of trailing edge flow separation from $\alpha = 11^\circ$ at $Re = 1.8 * 10^6$ to $\alpha = 14^\circ$ at $Re = 6 * 10^6$, thus leading to the increase of maximum lift coefficient $C_{L_{max}} = 1.58$ at $Re = 6 * 10^6$.

The CFD simulation results[4] for $Re = 1 * 10^6$ show presence of the static hysteresis loop in the lift coefficient dependency for a narrow range of $\alpha = 18^\circ$-19°. This indicates a possibility of bistable separated flow structures for the same angle of attack attitude. One can expect a trailing edge separation on the top branch and fully separated flow from the leading edge at the bottom branch for two points at $\alpha = 18^\circ$ and $\alpha = 19^\circ$. There is no static hysteresis loop in the experimental results, which may be due to a number of reasons, i.e. no tests with reverse change of angle of attack or noisy flow conditions, etc. Also the CFD results for $Re = 1 * 10^6$ are matching better with experimental data for $Re = 6 * 10^6$, when indeed one could expect this to be placed below experimental data for $Re = 1.8 * 10^6$. This mismatch can be addressed to the effective increase of the Reynolds number due to applied numerical procedure or insufficiency of the mesh resolution in [4].

To correctly simulate stall aerodynamics, the maximum lift coefficient $C_{L_{max}}$ can be taken as a key feature for verification of the CFD framework. The k-ω SST turbulence model is commonly considered as the most accurate model for aeronautical applications in terms of linear eddy viscosity formulations [17, 51]. The bottom plot in Fig. 4.28 shows a good match with the experimental dependence from [50] for the lift coefficient predicted by the URANS equations with the k-ω SST turbulence model at $Re = 6 * 10^6$ using the open source CFD code OpenFOAM [5], which is based on Finite Volume Method (FVM). There is a good correlation in $C_{L_{max}}$, but CFD prediction gives a two degree delay in the onset of full stall separation.

Fig. 4.27 shows computational prediction of the static hysteresis phenomena

for NACA 0012 at $Re = 6 * 10^6$. The simulations for URANS utilised the modified Baldwin-Lomax (BL) model and the shear stress transport model (k-ω SST [51]) for turbulence closure. Both turbulence models reasonably predict the lift coefficient slope and the maximum value $C_{L_{max}}$, which is placed below experimental data for $Re = 1.8 * 10^6$ as one can expect. The k-ω SST model failed to capture static hysteresis loop, while the modified BL model predicted four angles of attack points in the range of $\alpha = 15.5°$-$17.5°$, with bistable flow structures.

The modified BL model improves simulation results for the attached and separated flow conditions (Fig. 4.29). At $\alpha = 5°$ the aerodynamic coefficients obtained from URANS simulation with the Baldwin-Lomax model are highly agitated (dashed line in the top plot). This does not match with the intuitively expected result in the unsteadiness level in aerodynamic loads for nearly attached flow conditions. The modified BL model stabilizes the oscillations in $C_L(\tau)$, where $\tau = tv/c$ is the non dimensional time (solid line in the top plot). The bottom plot in Fig. 4.29 shows the amplitude of numerically induced oscillations in the lift coefficient at $\alpha = 5°$, when using the BL model. The unsteadiness amplitude in $C_L(\tau)$ due to vortex shedding in the stall region at $\alpha = 15°$ is also reduced by the modified BL model with the increase in the mean lift coefficient value. This is confirmed by the flow structures for $\alpha = 15°$ shown in Fig. 4.30 (BL model - top image, modified BL model - bottom image).

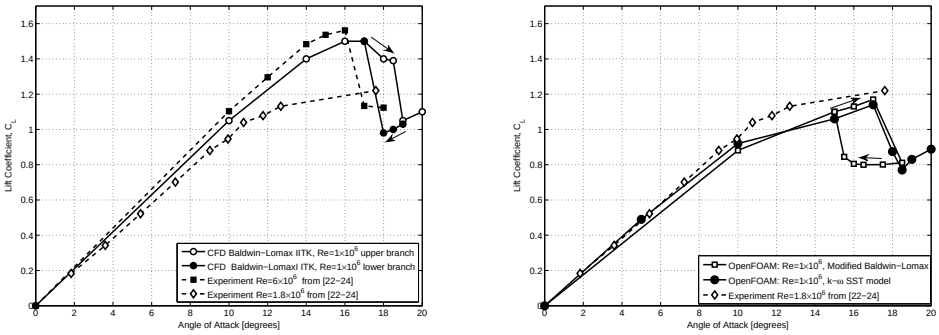

Fig. 4.27: NACA-0012 2D airfoil at Re = 1 million, CFD and experimental results.

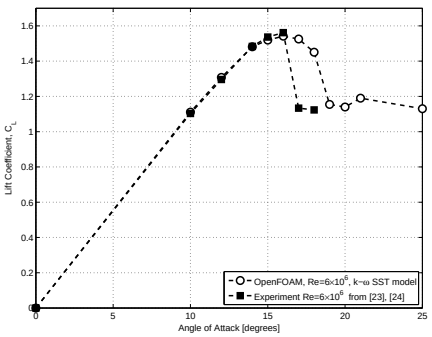

Fig. 4.28: NACA-0012 2D airfoil at Re = 6 million, CFD and experimental results.

The presented CFD simulations under predict C_L values in the range of angles of attack $5° < \alpha < 15°$, as the laminar bubble separation is not captured with the applied turbulence models. Prediction of the laminar bubble flow separation phenomenon needs special transitional turbulence models[52], but this is not an objective of this research work.

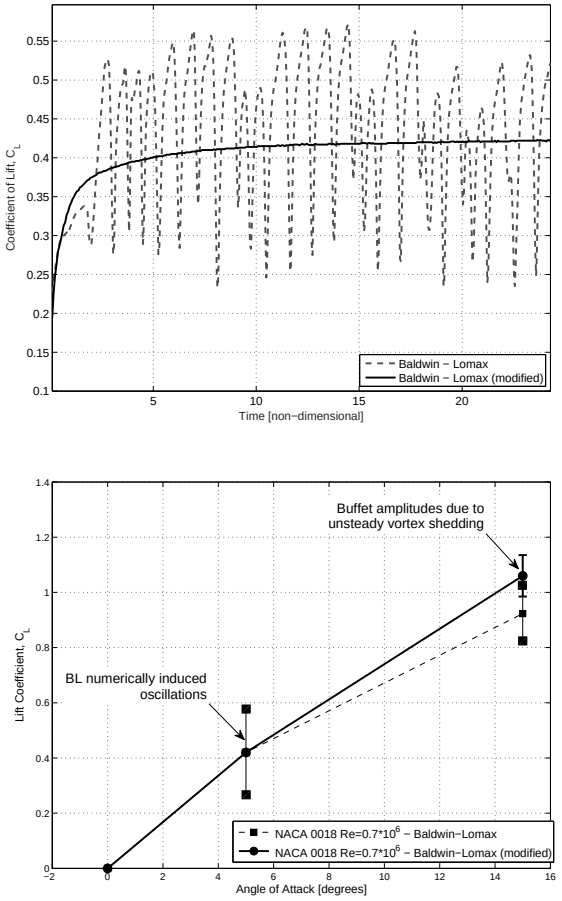

Fig. 4.29: Convergence at $\alpha = 5$ degrees(top) and oscillation amplitudes for low angles of attack - Baldwin-Lomax original model and modified BL model(bottom).

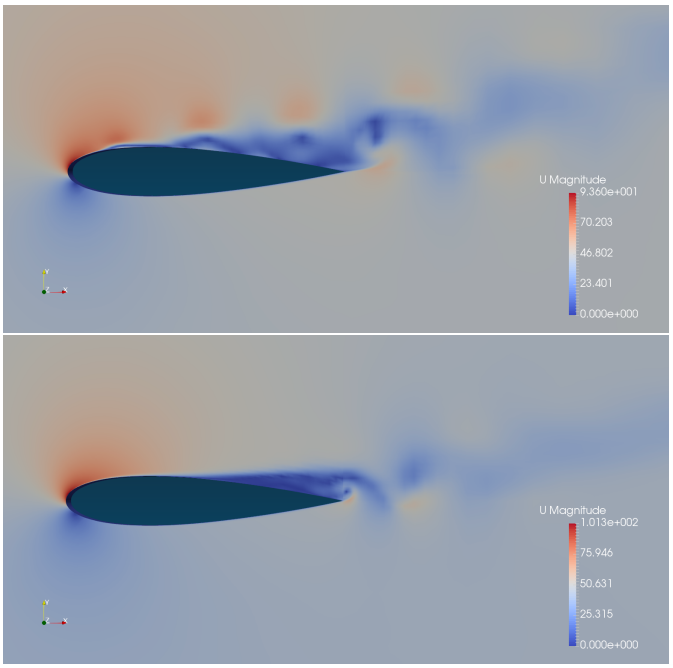

Fig. 4.30: Contours of velocity at $\alpha = 15$ degrees for original(top) and modified version(bottom)of Baldwin-Lomax model.

4.3.2 NACA 0018 at Low Reynolds Flow conditions using Modified BL and S-A turbulence model

The computational prediction of aerodynamic hysteresis loops in dynamic conditions with fast variation of angle of attack is more robust in comparison with static conditions. Such computational results are well known and extensively published [36–38].

Results show that the prediction of static hysteresis loop is highly sensitive to the selected turbulence model used for closure of the URANS equations, grid density, numerical solver, the flow Courant number and the method of mapping the flow field from previous step. A similar sensitivity is noticed to the airfoil thickness and flow Reynolds number. For instance, the attempt to capture static aerodynamic hysteresis made in paper [43] using the Menter's k-ω SST model for NACA 0018 was successful at $Re = 3 * 10^5$, while at higher Reynolds number of $Re = 7 * 10^5$ the prediction of static hysteresis failed. The above comments on sensitivity of experimental testing and computational prediction of static hysteresis phenomena clearly indicate the difficulties in comparison of wind tunnel experimental results against computational simulation of static hysteresis.

Prediction of the static hysteresis phenomenon is carried out using the Unsteady Reynolds Averaged Navier Stokes equations (URANS) with a Pseudo-Unsteady solver based on the Semi Implicit Pressure-Linked Equations (SIMPLE) algorithm [53] using the open source fluid dynamics software OpenFOAM[5]. A backward second-order accurate Euler time marching scheme was employed along with appropriate divergence schemes, which limit the fluxes of velocity. The Gauss

linear interpolation method was used to correct the fluxes at cell centres along the grid. The gradients of pressure was measured using the Gauss linear method, while for other flow quantities a cell limited least squares method was utilized.

The arising matrix system is solved using the Geometric Algebraic Multi-Grid (GAMG) method for pressure. A smooth solver with the Gauss-Seidel algorithm is utilized for velocity and other flow components. Each time step consists of a number of inner iterative loops in which the velocity, pressure and turbulent quantities are computed until the specified tolerance is reached (at least 3 orders less in magnitude of residual).

Such a numerical procedure allows simulations to be carried out with reasonably large flow Courant numbers (between 1 and 20), allowing simulations to be executed faster, while not compromising the solution accuracy. The number of inner loops in one time step increases with increase of the flow Courant number in order to meet accuracy requirements both locally and globally.

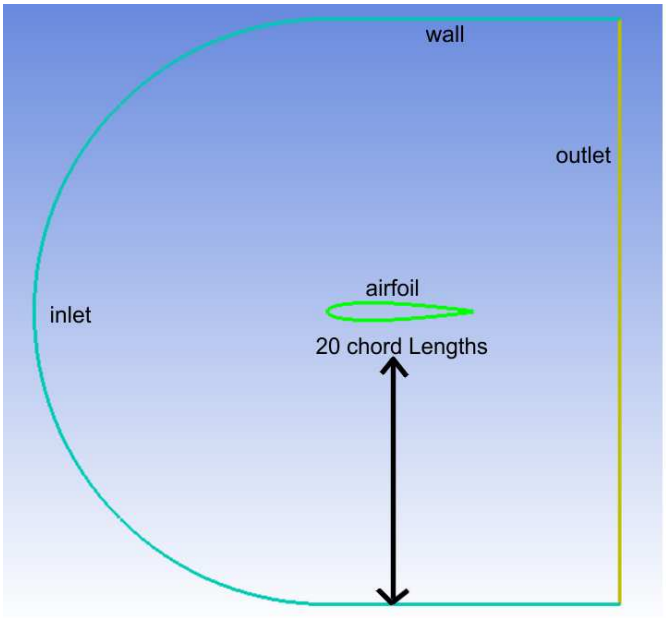

Fig. 4.31: Computational domain for the 2-D simulation.

The simulated flow domain is taken as a C type tunnel, which is conformal to the leading edge of an airfoil, allowing a curvilinear mesh to be created. The inlet, outlet, top and bottom walls were placed at least 20 chord lengths away from the airfoil, to ensure negligible influence of far field (see Fig. 4.31).

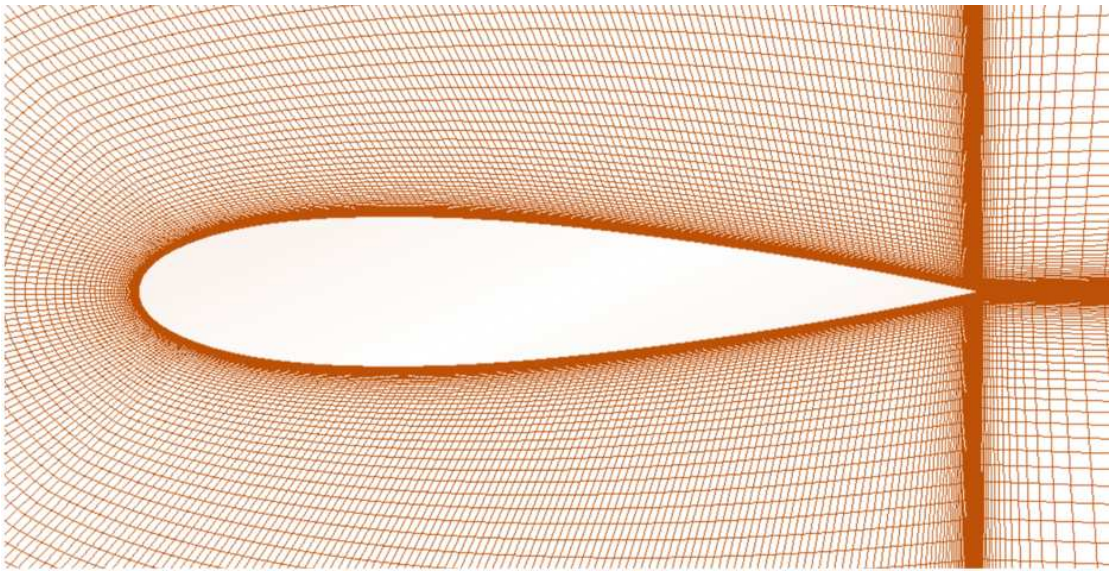

Fig. 4.32: Close up view of grid for NACA 0018 airfoil.

The mesh for NACA 0018 airfoil was created as a structured grid by splitting the domain into different blocks. The grid is more dense towards the walls of the airfoil and along the lines connected to the sharp trailing edge (see Fig. 4.32). The non-dimensional wall distance, Y+, was maintained below 1 for the first cell and the cell growth ratio was below 1.1 to ensure that the viscous layer in the boundary is well captured. The mesh quality was improved with respect to the orthogonality, skewness, aspect ratio and cell size transition ratios.

Algebraic models such as the Baldwin-Lomax model allow quick iterative CFD simulations for aeronautical applications with significant reduction in computational time. However, the Baldwin-Lomax model [54] has difficulties in its implementation, as it requires the dimensionless wall distance $Y+$ to be calculated along a straight line normal to the wall extended to the far field.

Only for certain combinations of grids and CFD solvers it is possible to determine $Y+$ in such a manner. Furthermore, the function $F(y)$ reaches it's maximum value twice in its profile, once very close to the airfoil. Due to this, the solver cannot chose the right $F(y)_{max}$, i.e. the second maximum further away from the wall. If Y_{max} is determined from the first maximum of function $F(y)$, the eddy viscosity value is significantly underestimated thus affecting the flow velocity field and location of separation point. The Baldwin-Lomax model also has difficulty in determining the maximum thickness of the inner eddy viscosity zone at the dimensionless wall distance $y_{crossover}$, which is calculated when the inner eddy viscosity is equal to the outer eddy viscosity value. And this criterion can be true for more than one location in the grid at a given simulation time.

Modification of the Baldwin-Lomax model, which is free from the above mentioned difficulties, is discussed below. The proposed modification redefines the outer eddy viscosity zone replacing F_{WAKE} with original function $F(y)$.

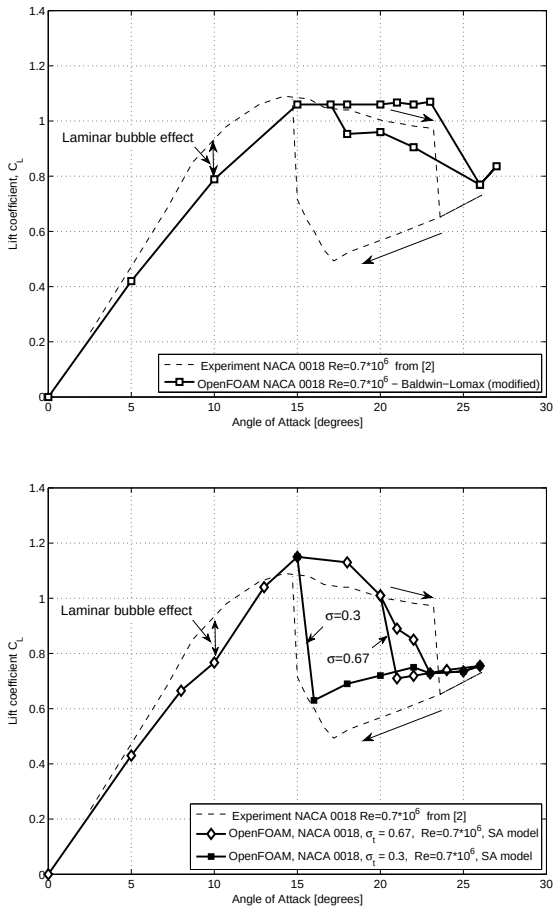

Fig. 4.33: Static Hysteresis Loops - CFD and Experimental - NACA 0018 - 2D , Re = 700,000.

The previous analysis of the NACA 0012 stall aerodynamics is not fully complete due to the absence of the static hysteresis phenomenon in the experimental data. Such experimental data with static hysteresis loops are available for many configurations. In the following analysis the data for NACA 0018 airfoil at $Re = 0.7 * 10^6$ [27] are considered for validation of CFD static hysteresis prediction. The top plot in Fig. 4.33 shows that the modified BL model predicts maximum lift and the onset of full flow separation rather well in comparison with the experimental dependence $C_L(\alpha)$ [27] (dashed line). Also, the static hysteresis phenomenon has been predicted in this simulation, but the lower branch is significantly elevated, substantially shrinking the hysteresis loop (top plot - square markers).

This underestimation of the static hysteresis loop size may be due to a number of reasons. The Y_{max} parameter in the modified BL model is fixed and is not adjusted to the large eddy separation flow conditions. This may lead to inadequate modelling of turbulent momentum transfer inside such a vortex circulation zone.

The deficiency of Baldwin-Lomax and similar algebraic models to predict the turbulent diffusion is overcome with Partial Differential Equations (PDE) based

turbulence models, which improve the modelling of production, destruction and diffusion of eddy viscosity term.

The Spalart-Allmaras (SA) turbulence model is one of the most simple and popular one-equation models of this class used in aeronautical applications [15]. Bottom plot in Fig. 4.33 shows that the SA turbulence model slightly over predicts the maximum lift coefficient $C_{L_{max}}$ and captures static hysteresis loop in a narrow range of angle of attack ($\Delta\alpha \approx 2°$). The turbulent Schmidt number σ_t, the ratio of eddy viscosity to eddy diffusivity, is an important parameter in the SA model. In many publications, it is usually taken as $\sigma_t = 0.67$. But if the turbulent Schmidt number value is reduced to $\sigma_t = 0.3$, this significantly expands the lower branch of static hysteresis loop with fully detached flow conditions till $\alpha = 16°$, which is in close correlation with the experimental data. Based on this simulation result one can assume that the reduction of σ_t is more appropriate for fully separated and circulating flow conditions formed by large eddies.

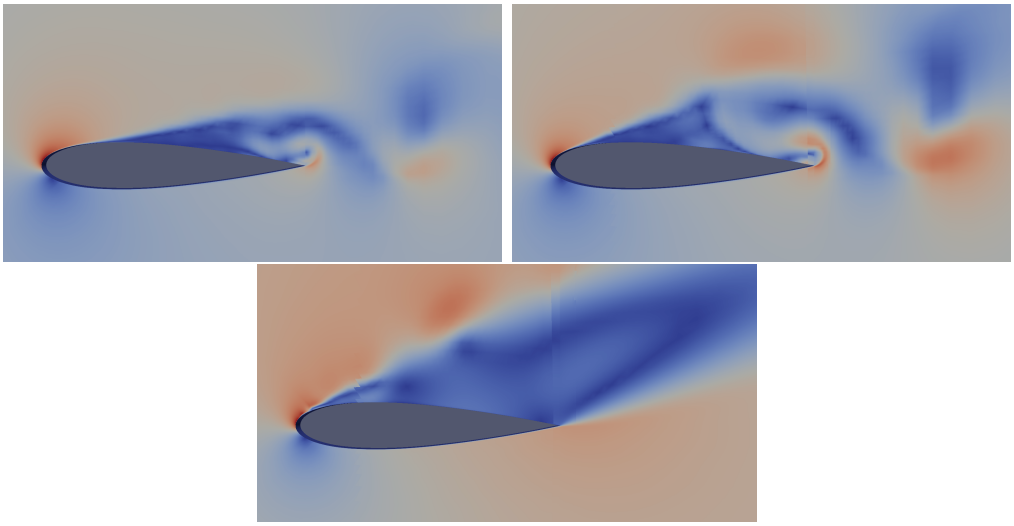

Fig. 4.34: Flow field images of NACA0018 at $Re = 0.7 \times 10^6$ and $\alpha = 18°$, top left- modified BL model, top right - SA model and bottom plot shows SA model with lower Turbulent Schmidt number

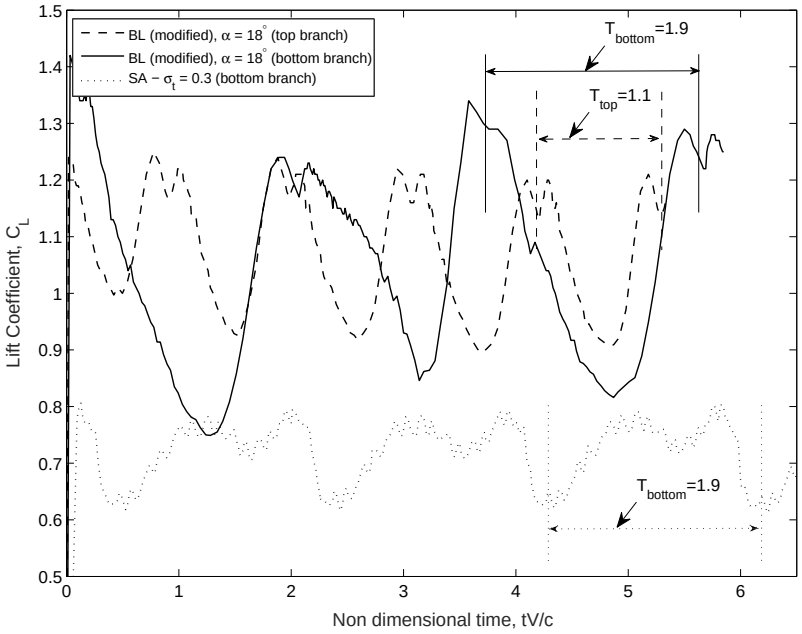

Fig. 4.35: flow stream patterns for NACA 18 at Re = 700,000 at multiple solutions using Baldwin-Lomax model.

Fig. 4.34 shows contours of velocity levels obtained with the modified BL and SA model. The modified BL model reasonably captures trailing edge separation on the top branch of static hysteresis loop, starting approximately at $0.75c_{ref}$ from the trailing edge with unsteady vortex shedding. The flow pattern at the bottom branch has a similar separation pattern with separation starting approximately at $0.9c_{ref}$ from the trailing edge with bigger scale of unsteady vortex shedding. The SA turbulence model with $\sigma_t = 0.3$ gives a fully developed flow separation zone starting at the leading edge of the airfoil with large circulatory flow.

Variation of the lift coefficient $C_L(\tau)$ vs non dimensional time $\tau = tV/c_{ref}$ for all three flow patterns discussed above is shown in Fig. 4.35. The $C_L(\tau)$ dependencies show various aerodynamic buffet processes, which are characterised by their amplitude and frequency spectrum. The oscillations in lift coefficient $C_L(\tau)$ with low frequency and large amplitudes reflect shedding of the large scale eddies. While, the oscillations with low amplitudes and higher frequencies reflect shedding of smaller scale eddies. Periodic time for vortex shedding predicted with the modified BL model on the top branch of static hysteresis is $\triangle\tau \approx 1.1$ and on the bottom branch is $\triangle\tau \approx 1.9$. The SA model predicts a significantly lower average value for $C_L(\tau)$ for the bottom branch, the reduced buffet oscillation amplitude with the same periodic time $\triangle\tau \approx 1.9$.

The above analysis shows that the flow prediction in stall region associated with the static hysteresis phenomenon is highly sensitive to the turbulence model type and selection of model constants. Combination of the URANS and Large Eddy Simulation (LES), more commonly known as Detached Eddy Simulation (DES) [19], may be considered as a more adequate approach for prediction of

the static aerodynamic hysteresis. Although being much more expensive in terms of the required computational time, DES can be used for generating simulation results, that can be used as a reference for tuning turbulence models used for closure of the URANS equations.

For illustration purposes, Fig. 4.36 shows simulations of separated flow patterns for the top branch of the static hysteresis loop on NACA 0018 airfoil at $\alpha = 20°$ and $Re = 0.7 \times 10^6$, obtained using the original and modified BL model, SA model and DES in combination with the SA turbulence model [19]. The original BL model gives unsteady separated flow with small scale eddies shedding with high frequency. The modified BL model shows more stable separated flow structure with larger scale eddies shedding with lower frequency. The SA model with $\sigma_t = 0.67$ shows a steady circulatory zone reattached to the trailing edge. The modified BL model predicts the flow separation point further upstream compared to the SA model.

The flow pattern produced in the DES simulation is more similar to the pattern obtained by URANS simulations closed with the modified BL model. The later predicts flow separation point closer to the leading edge in comparison with DES results affecting the size of the separation zone. The flow separation point in the case of SA model is almost the same as in the DES simulation, but the circulatory zone looks more stable with less vortex shedding.

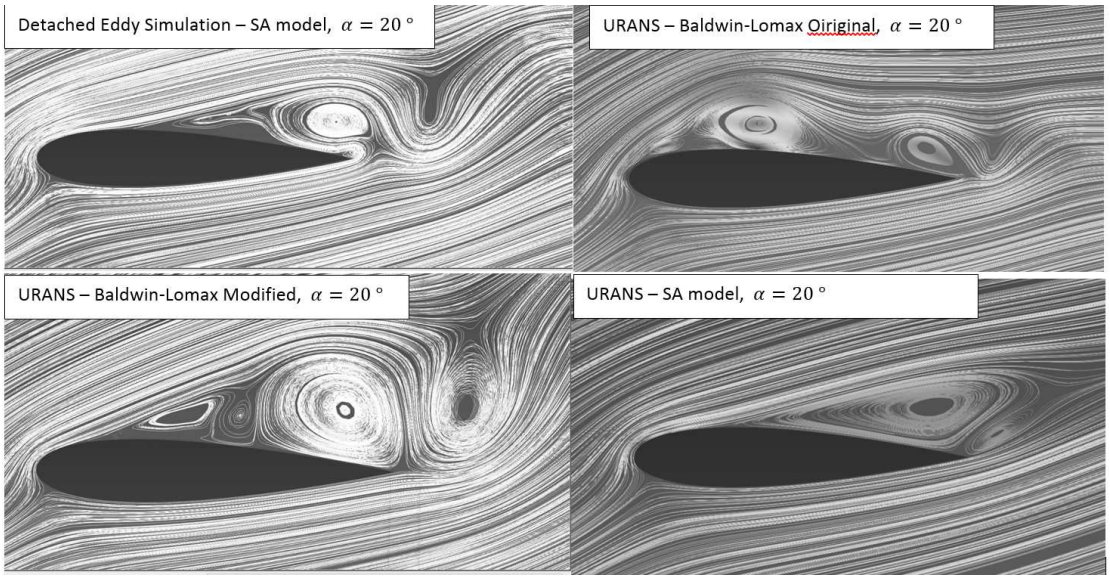

Fig. 4.36: Streamlines of flow for NACA 0018 at $\alpha = 20° = 20$ degrees DES-SA Vs. Modified Baldwin-Lomax model.

An adequate CFD simulation of the static hysteresis phenomenon is required for modelling of stall aerodynamics in static and dynamic conditions. This is now important in many applications from aerodynamics modelling for Loss-of Control In flight (LOC-I) to the active flow control on wind turbine blades.

The proposed modification of the Baldwin-Lomax algebraic turbulence model has a stabilising effect on the flow at low angles of attack with attached flow

conditions and reduces the buffet amplitude in stall region with increase in mean value of the lift coefficient. The static hysteresis loop has been predicted in the range of $\triangle\alpha \approx 3^{\circ}$ for NACA 0012 airfoil at $Re = 1 \times 10^6$. No experimental data for this case was available for comparison.

The presented simulation results for NACA 0018 airfoil show significant sensitivity of the static hysteresis phenomena to many factors such as airfoil thickness, Reynolds number, the type of turbulence model and its constants. The level of flow turbulence and intensity of structural vibrations are additional important factors which will make the accurate prediction of the static hysteresis phenomenon more difficult.

The Detached Eddy Simulation (DES) seems to be more appropriate for prediction of the static hysteresis phenomena, but being computationally expensive, it can only be used for tuning process of turbulence models and their constants for closure of the URANS equations.

4.3.3 TsAGi-9140 airfoil at Moderately Higw Reynolds Flow conditions

Static Hysteresis in flow past TsAGi-9140 airfoil and its modified versions (1.5 and 2 percent circular bump introduced to the Leading Edge) at a Reynolds number of $Re = 5 * 10^6$ is carried out using Unsteady Reynolds Averaged Navier-Stokes (URANS) equations with OpenFOAM CFD code, which is based on Finite Volume Method(FVM). OpenFOAM [5] is a reliable platform to evaluate static hysteresis because it is written in object oriented C++ programming which is modifiable, thus, allowing modification and implementation of numerical methods when and if it is required. For the analysis used in this work, the two most commonly applied eddy viscosity models in aeronautical applications i.e. 1) Spalart-Allmaras (S-A) model[15] and 2) the two-equation k-ω SST model by Menter[17] are used for turbulence closure. For each configuration tested a pitch-up phase where the angle of attack is increased until development of full flow separation and a pitch-down phase where angle of attack is decreased until reattachment of the flow. The simulations also utilized a moderately tuned version of SA eddy visocisty model in which the turbulent Schmidt number σ_t is reduced from 0.6 to 0.35.

The governing equations, mesh resolution, turbulence models used and effect of modification of the turbulent schmidt number on prediction of static hysteresis loops for the tested configurations are discussed= as follows.

Grid and Boundary conditions

The airfoil is placed in a far field which is at least 30 chord lengths away from the airfoil in every direction. The grids are produced in ICEM CFD and using a structured mesh generation approach. This approach is favorable for grid generation around the leading edge modified versions of the TsAGi-9140 airfiol, see (Fig.4.21). The grids have $Y+ = 1$ and more cells in the streamwise direction which helps to maintain a low aspect ratio and high quality quadrilaterals. The number of cells varied from $30k$ to $45k$ allowing a reasonably accurate prediction

of the solution. The generated grids are shown in Fig. 4.37 to 4.39. Once the grids were generated and exported to the solver, appropriate boundary conditions were denoted and they are:
$\hat{\upsilon}_{wall} = 0$, $\hat{\upsilon}_{farfield} = 3\upsilon_\infty$ to $5\upsilon_\infty$, and $\upsilon_{twall} = 0$
and $\frac{\partial p}{\partial x}_{wall,farfield} = 0$
where U is velocity, υ_t is the turbulent viscosity, $\hat{\upsilon}$ is modified turbulent viscosity and $\frac{\partial p}{\partial x}$ is the pressure gradient. Also note that the Farfield boundary conditions applies to the velocity inlet/outlet in this case and wall is refers to any solid surface.

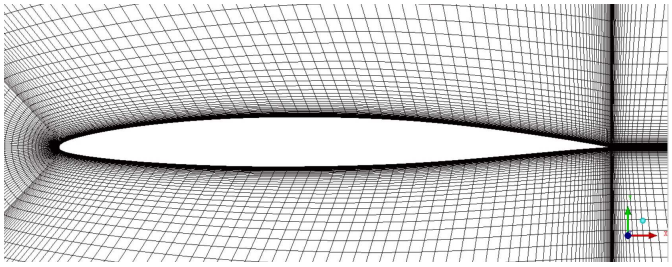

Fig. 4.37: Mesh generated for clean TsAGi-9140 airfoil.

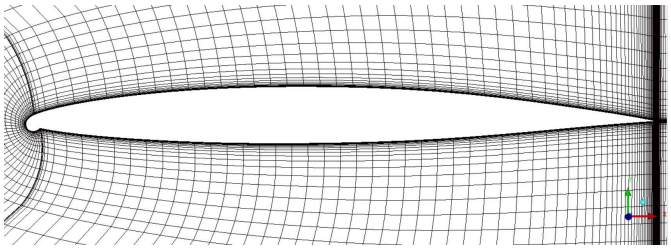

Fig. 4.38: Mesh generated for 1.5% LE modified TsAGi-9140 airfoil.

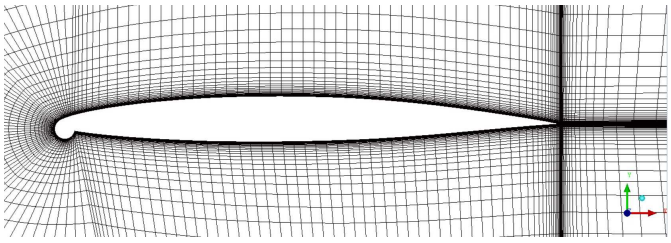

Fig. 4.39: Mesh generated for 2% LE modified TsAGi-9140 airfoil.

Results and Discussions

Validation of CFD models and computational algorithms for prediction of static hysteresis phenomenon is an important task in applied aerodynamics. To achieve this, the computational simulation results are compared to the wind tunnel data. The experimental data demonstrate significant hysteresis loops in the aerodynamic lift coefficient at rather high Reynolds numbers $Re \approx 5 \times 10^6$.

The lift coefficient C_L for the non-modified TsAGI-9140 airfoil has been predicted using k-ω SST and SA turbulence models as shown in Fig.4.40. To compare two-dimensional simulation results against the experimental data, obtained for the finite aspect ration wing $AR = 5$ in paper[46], the computational results have been re-calibrated by factor, calculated as carried out in [**?**].

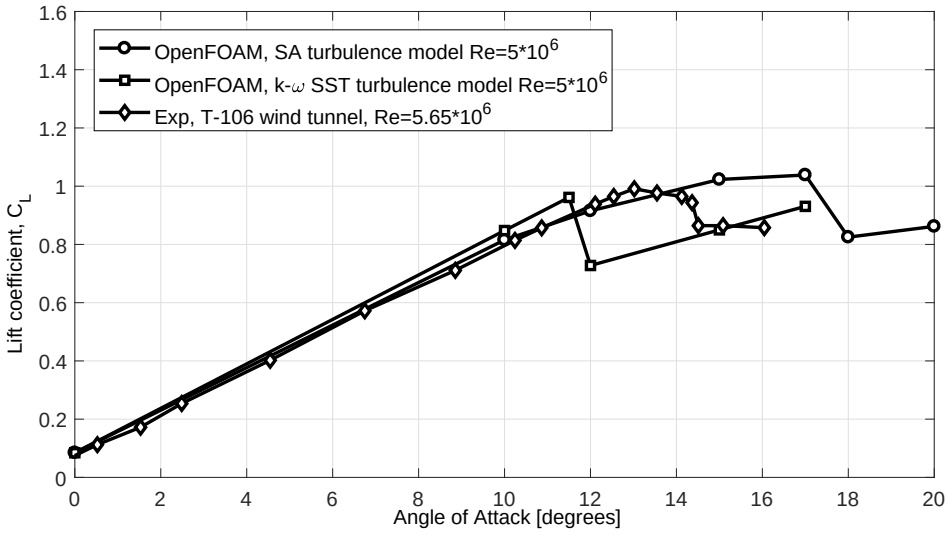

Fig. 4.40: Experiment and CFD results for clean TsAGi-9140 airfoil.

Fig. 4.40 shows the lift coefficient C_L prediction for the clean TsAGi-9140 airfoil at $Re = 5 \times 10^6$ obtained using the SA and SST turbulence model plotted against the experimental results from wind tunnel at $Re = 5.65 \times 10^6$. The SA model results(open circle) shows delayed stall while the SST model results(open squares) illustrate earlier stall in comparison to the experimental stall angle. SST model also has a very slight over prediction of the lift coefficient slope C_{L_α} when compared against SA and experimental results while the maximum lift coefficient $C_{L_{max}}$ is approximately same for CFD and experimental tests. Furthermore, experiments did not indicate existence of static hysteresis phenomena for the clean configuration and on several attempts CFD was not capable of capturing hysteresis loops as well for the clean configuration of the TsAGi-9140 airfoil.

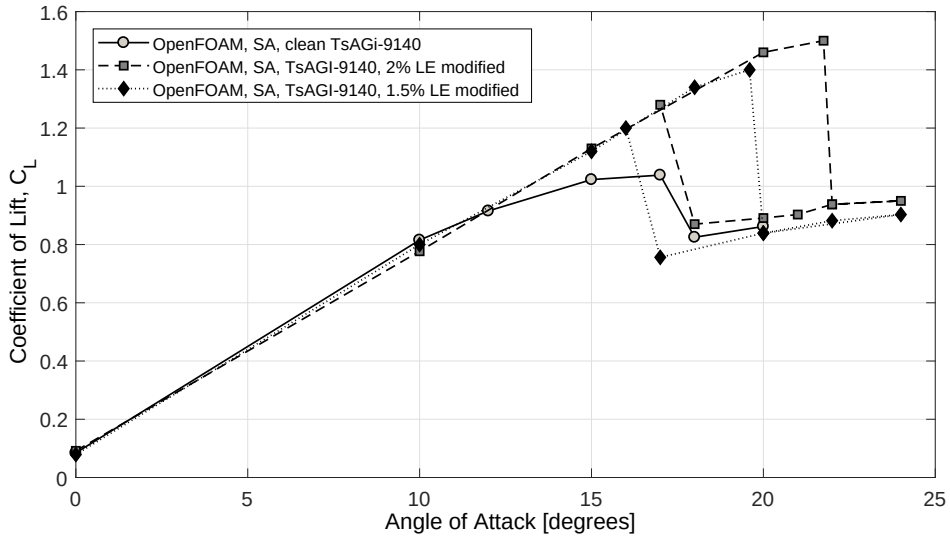

Fig. 4.41: CFD results for TsAGi-9140 airfoil at $Re = 5 \times 10^6$.

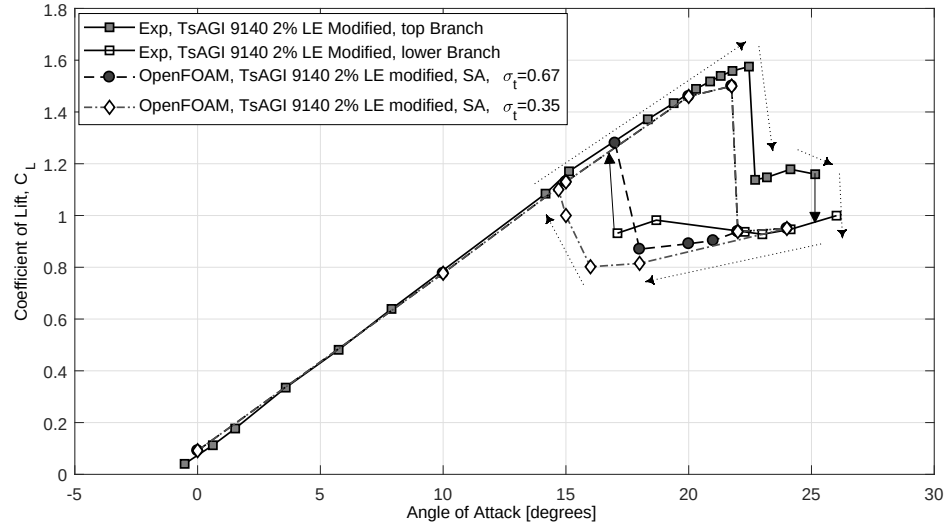

Fig. 4.42: Experiment and CFD results for 2 percent modified TsAGi-9140 airfoil at $Re = 5 \times 10^6$.

Fig. 4.41 shows the prediction of static hysteresis using SA model for the TsAGi-9140 airfoil. As experiment demonstrated the leading edge modified configuration with 2 percent bump included on the lower side increased the maximum lift coefficient to 1.5 and delayed the stal angle by 5-7 degrees. On returning from stalled conditions to lower angles of attack a 4 degree wide static hysteresis loop were captured as well. Further testing with lower Turbulent Schmidt number of $\sigma_t = 0.35$ increased the width of this loop by another 2 degrees as shown in Fig. 4.42.

4.4 Concluding Remarks on Static Aerodynamic Hysteresis

It is evident through both experimental and computational results that static aerodynamic hysteresis is a real phenomenon which causes late recovery from stalled conditions. From the acquired results in this chapter, it was found out that the static hysteresis loops are sensitive to various factors in both experimental and numerical predictions.

It was found that for the same Reynolds number of $Re = 300,000$ experimental results for static hysteresis in flow past NACA 0018 (see Fig. 4.19) are significantly different. While the flow Reynolds number might be the same, the only possible explanation for the difference in experimental results should be the wind tunnel flow conditions. The hysteresis loops are extremely sensitive to the acoustic noise, turbulence intensity and rig stability of the wind tunnel. Therefore it can be concluded that meaningful results can only be produced if one takes great caution in ensuring that the previously mentioned factors are being monitored and adjusted well to match the tunnel conditions from the source of results that the experiment is being compared to.

The understanding that static hysteresis is limited to low Reynolds flow conditions can be classified as an inaccurate assumption as the experimental results in flow past TsAGi-9140 airfoil at 5 million Reynolds demonstrates large static hysteresis loops (see Fig. 4.22. Therefore, it can be stated that the static hysteresis loops are not only caused due to the known assumption of low Reynolds laminar bubble formation but also due to the inability to recover from a stalled condition with attempt to remember pre-history of the flow field.

The computational results that are presented in this chapter shows that the turbulence model and its parameters effect the ability to accurately capture the static hysteresis loops . While the more complex turbulence models such as Menter's shear stress transport (SST) model fails to predict the loops, much simpler eddy viscosity models such as Spalart-Allamaras (S-A) and Baldwin-Lomax (BL) capture and predict the hysteresis loops much more effectively. It is also noted that the parameters in most of the eddy-viscosity turbulence models for the rate of production, destruction and diffusion of turbulence are well adjusted to the attached flow conditions and much less attention has been given to the tuning of these parameters to post-stall flow region with fully separated flow conditions. Lowering the value of the turbulent diffusion coefficient (σ_t) improves and stabilizes the lower branch of static hysteresis loops according to the computational results presented in this chapter (see Fig. 4.33).

While, the findings in this chapter are quite valuable it is but limited and much more research should be conducted. Further assumptions include that the static hysteresis loop is quite sensitive to the state of flow from which the simulations are initiated when in stalled conditions (whether from separated or slightly attached condition). It can also be stated the results are sensitive to the method of simulation such as if the wing is moving (slow dynamic with much reduced frequencies) or pitching in prescribed and fixed α changes. The preliminary results show that a

slow dynamic moving method is more stable in CFD simulations as the unsteady initial transient is omitted which occurs in the case of fixed α change to achieve the desired degree of angle of attack. Nevertheless, the method of slow dynamic motion is much more costly as the total simulation time is largely expanded due to the very slow reduced frequencies. Hence, the accurate simulations of static hysteresis loops need much more research and input to improve and stabilize the predictions of aerodynamic hysteresis.

Chapter 5

Ice Accretion effect on Aerodynamics of Flight

It is evident that In-flight icing can cause degradation of aerodynamic performance. However, the extent of degradation of aerodynamic characteristics to different icing shapes on the airfoil/wing is still not very clear. Furthermore, the current CFD and other numerical/mathematical modeling and simulation capabilities to check for the effect of icing on airfoils/wings and aircraft is not throughly researched. In this chapter, XFOIL and ANSYS Fluent are used as simulation tools to evaluate the effect of icing on the performance of airfoils and wings. XFOIL from [59] is panel code method which quickly iterates and produces accurate results prior to the stall region. The use of XFOIL enables to produce fast and reliable results with and without leading edge modifications of ice shapes installed thus giving a really good insight to the changes in aerodynamics in the case of low to severe ice accretion. On the other hand, the use of ANSYS Fluent, a well established CFD software allows reliable, accurate results which can then be compared to XFOIL's results along with an insight to the changes in the flow field with contours, streamlines and profiles which are not able to be produced in XFOIL.

The changes in shear layer and vortex shedding patterns in the case of a horn shape ice on the leading edge of an airfoil discussed in [56] is shown in Fig. 5.1.The airfoil in Fig. 5.1 is NLF airfoil and the changes in its aerodynamics for a horn ice accretion and clean conditions at $Re = 1.8 \times 10^6$ using CFD methods are shown in Fig. 5.1. The clean airfoil stalls at about 14 degrees while the Iced airfoil stalls at about 4 degrees. The 10 degrees early stall can be noted as an extreme degradation of performance and a hazard for flight. The differences in the estimation of turbulent intensity for CFD and experimental work in [56] is shown in Fig. 5.2.

Numerous research has been conducted to study the changes in aerodynamics of ice accreted airfoils and also to build Lagrangian models which can simulate the shape and size of ice that wil deposit on airfoils at given weather conditions. For instance, the study in [57] has a very through research on ice accretion and changes in aerodynamics for a large number of airfoils that are used in the design phase of modern aircraft.

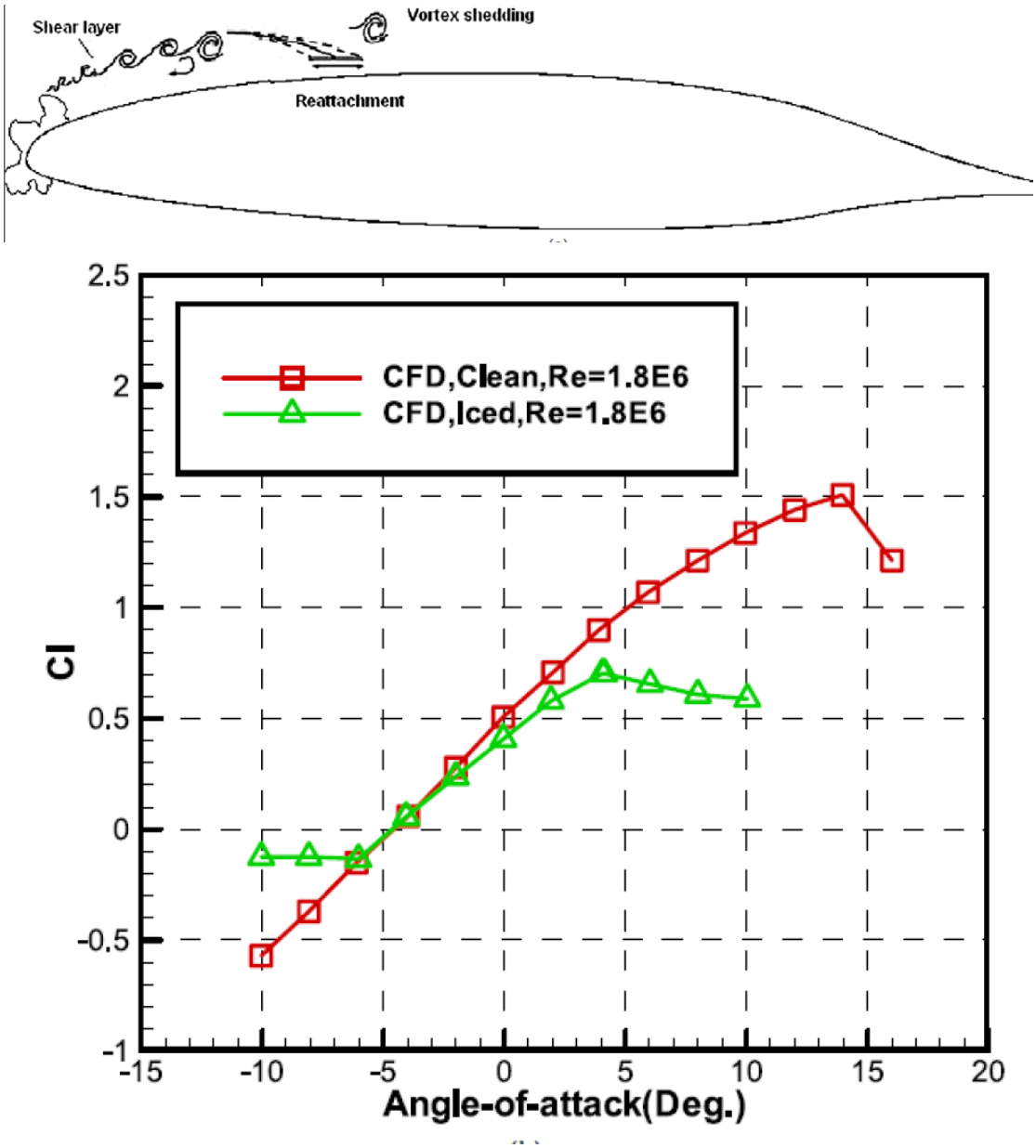

Fig. 5.1: Shear layer and vortex shedding distribution for a horn shape ice deposited airfoil from [56].

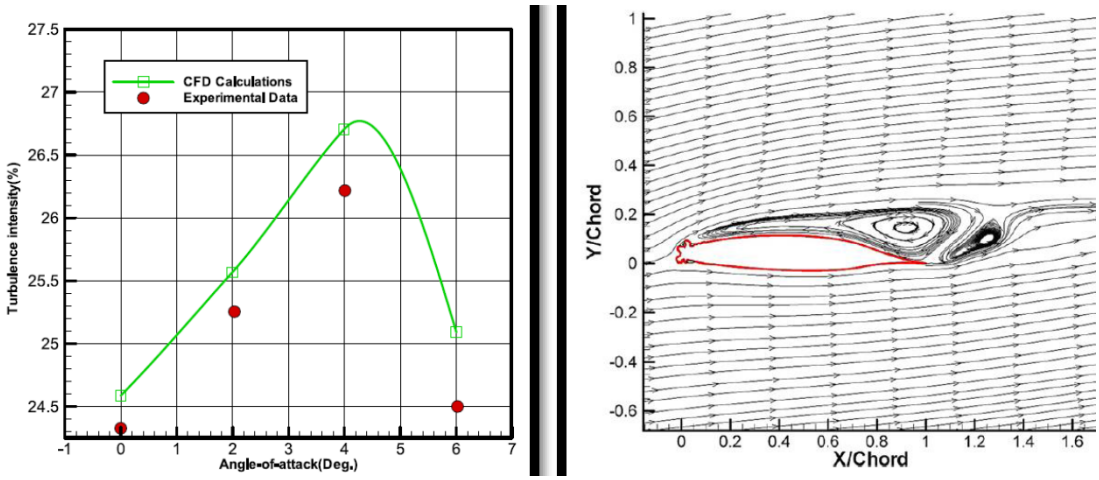

Fig. 5.2: CFD and experimental data for horn shape iced airfoil from [56].

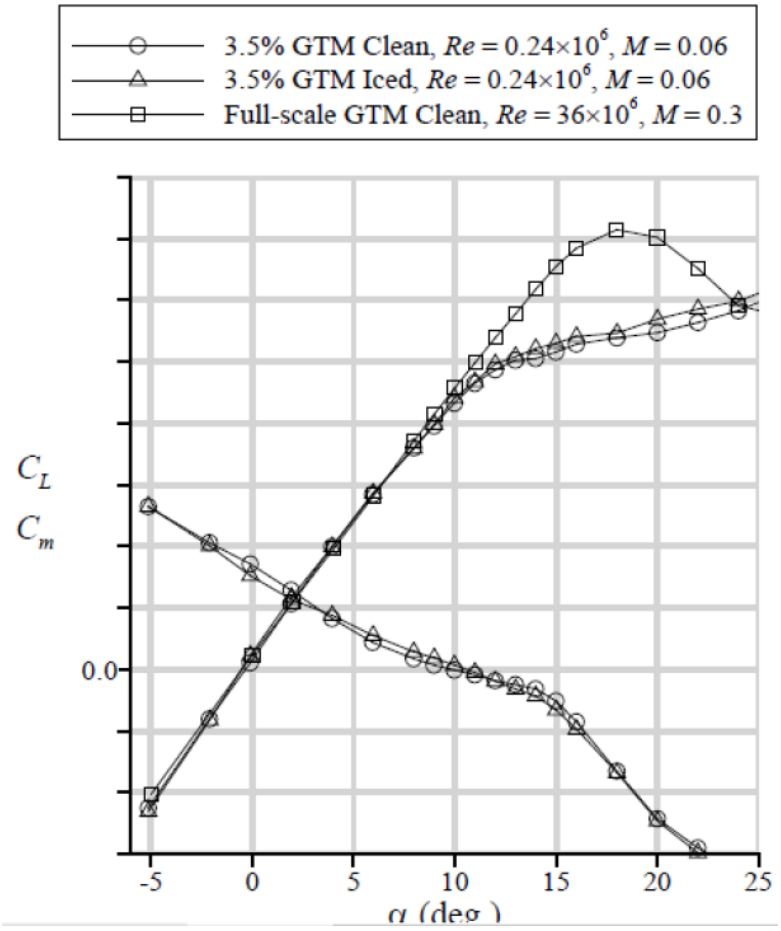

Fig. 5.3: Wind tunnel results for NASA GTM model with and without ice from [58].

Furthermore, continuous attempts are made to compare and evaluate the effect of icing on 3D aircraft models that represent commercial flight. Researchers in

NASA Langley research centre utilized a Wind tunnel of 12 feet wide cross-section, which was a Low-speed Wind tunnel to verify the effect of icing on a 3.5 percent scaled generic transport model of NASA Langley research centre. Mach number used was 0.06 and Reynolds number was 0.24 million. The scaled generic transport model (GTM) was used in both clean conditions and with full span artificial ice shapes attached to the leading edge of the wing, horizontal and vertical tail [58]. The results from Fig. 5.3 shows the differences for full scale and scaled down GTM models with and without ice shapes installed on the leading edge.

Results obtained in Jian Ming Liu's work [61] is presented below. The analysis was carried out for various cross sections of the Boeing 737 wing. The effect of rime ice accretion with 5 different ice shapes are investigated in open source cfd code SU2 for the B737 root airfoil.

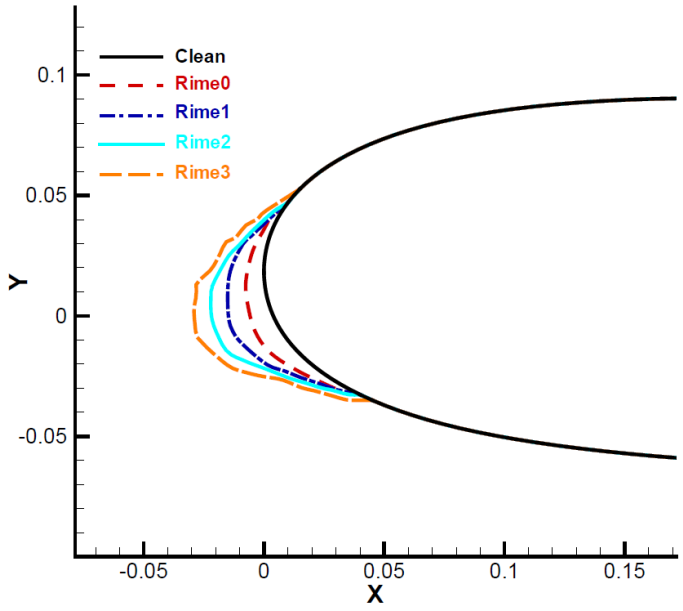

Fig. 5.4: Rime Ice shapes for Boeing 737 wing root airfoil [61].

Fig. 5.4 shows the 5 different rime ice shapes that were used for the analysis. The cartesian grids generated for the ice accreted airfoil are shown in Fig. 5.5.

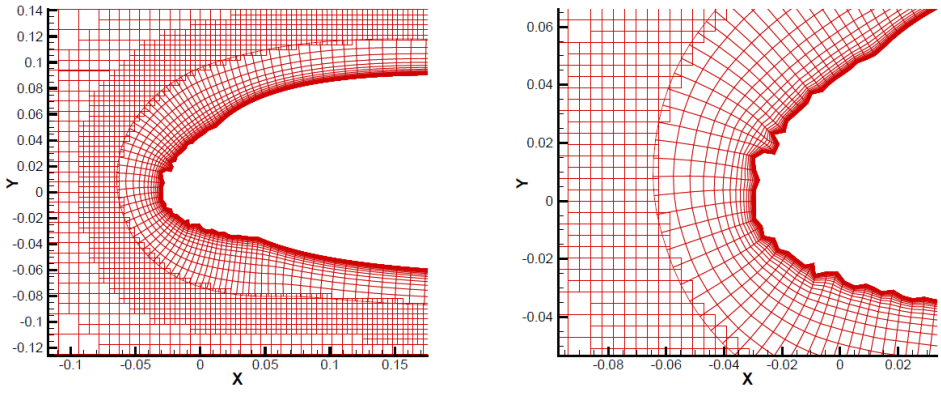

Fig. 5.5: Grids generated for rime ice shapes for Boeing 737 wing root airfoil [61].

The simulation results (see below Fig. 5.6) indicates that the clean airfoil stalls at about 14 degrees with $C_{L_{max}} \approx 1.4$ but airfoil with rime ice shape 3 and maximum ice accretion stalls at 10 degrees (4 degrees early) with $C_{L_{max}} \approx 0.9$

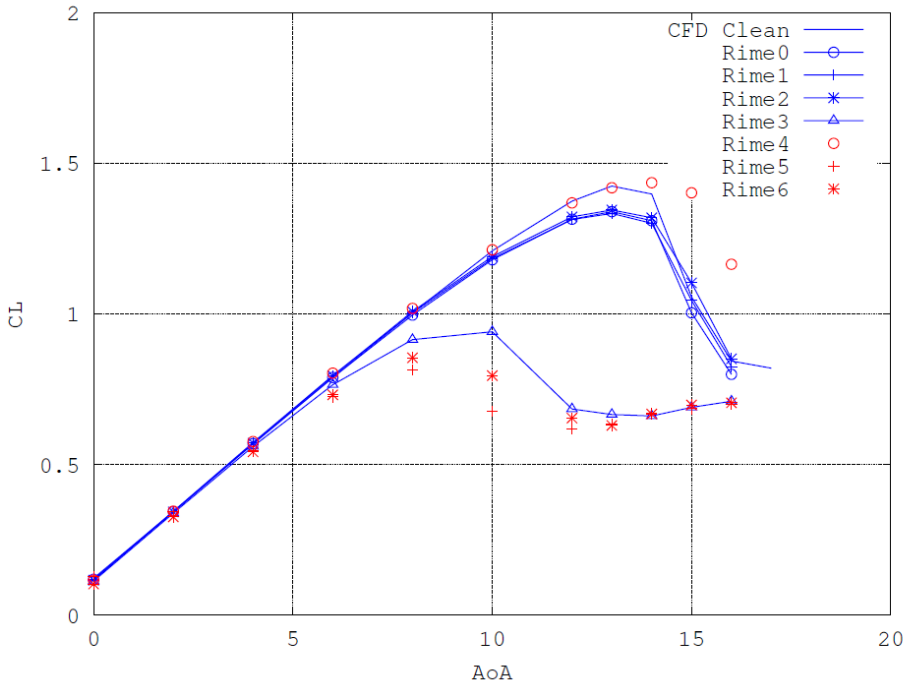

Fig. 5.6: Results obtained for rime Ice shapes for Boeing 737 wing root airfoil [61]

Liu's work also includes analysis of Boeing 737 wing in 3 dimensional unsteady fluid flow.

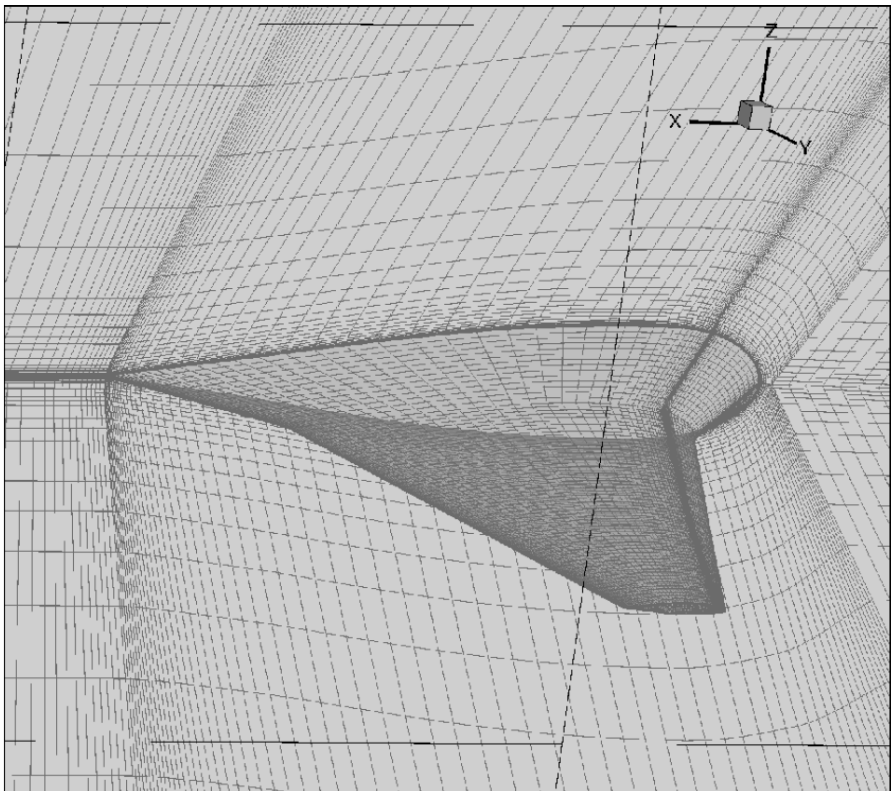

Fig. 5.7: Grid generated for 3d iced wing [61].

The grid generated (see Fig. 5.7 with a horn ice shape were then simulated in SU2 software and the aerodynamic coefficients obtained for lift and drag are shown in Fig. 5.8.

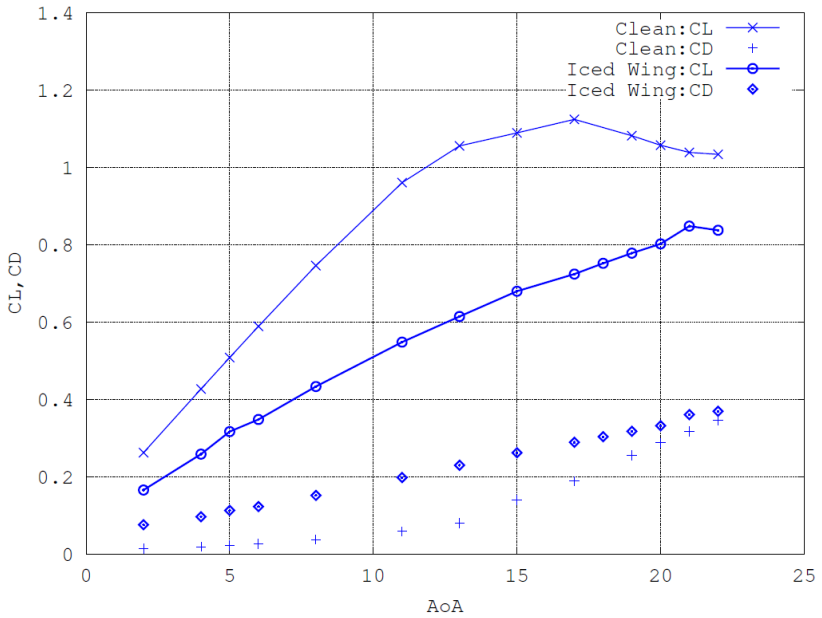

Fig. 5.8: Aerodynamic coefficients obtained for clean and iced 3D wing [61].

The results clearly indicate that the clean wing has a much higher lift coefficient and a much lower drag coefficient for almost all the angle of attacks when compared to the Iced wing. The flow separation that happens at $\alpha = 11$ degrees very close to the root of the wing at y = 3.6526m is shown in Fig. 5.9.

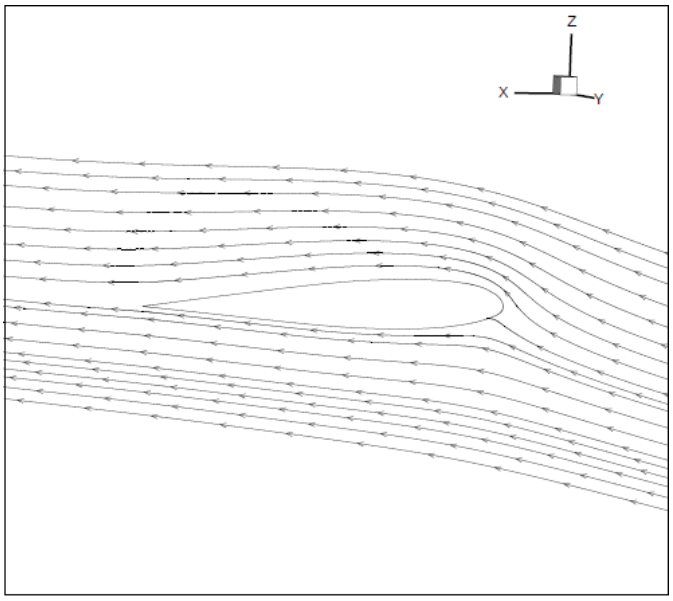

(a) Clean wing

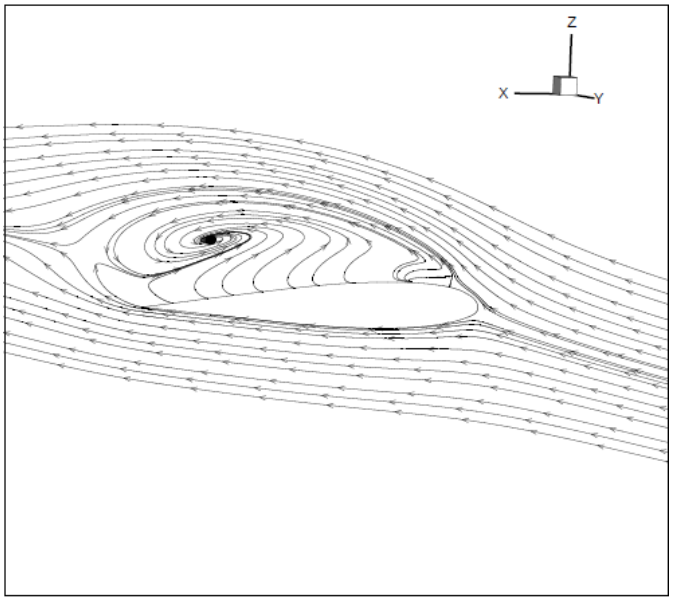

(b) Iced wing

Fig. 5.9: visualization of flow streamlines at y = 3.6526m and $\alpha = 11$ degrees [61].

5.1 Analysis of NACA 4412 airfoil with ice accretion using XFOIL and ANSYS Fluent

Initially, XFoil is used to evaluate the aerodynamic perfomance of clean and iced airfoils. XFoil [59] is a panel method to evaluate aerodynamic perfomance and is extensively used for quick design and testing of airfoils.

The icing shapes installed on NACA 4412, an asymmetric airfoil, are shown in Fig. 5.10.The icing shapes used are installed with respect to the commonly found ice shapes on leading edge of wings [56].

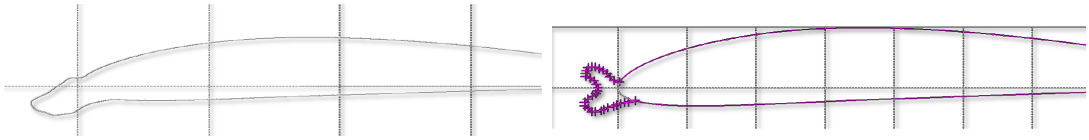

Fig. 5.10: Icing shape 1 (top) and icing shape 2(bottom) installed on NACA 4412 airfoil.

Fig. 5.11 shows the results using XFoil software for NACA 4412 airfoil with leading edge ice accretion shape 1 and 2 (see Fig. 5.10). The clean airfoil has a maximum lift coefficient of ≈ 1.6. The airfoil with Icing shape 1 also has the same maxmimum lift coefficient however it should be noted that the C_{L_α}, i.e. slope of the lift coefficient is a bit lower than the clean airfoil and the stall is more abrupt than for the clean airfoil. For icing shape 2 the airfoil is shown to stall at around 8 degrees and the maximum lift coefficient $C_{L_{max}}$ is ≈ 1.00 which is 60 percent lower than $C_{L_{max}}$ for the clean airfoil.

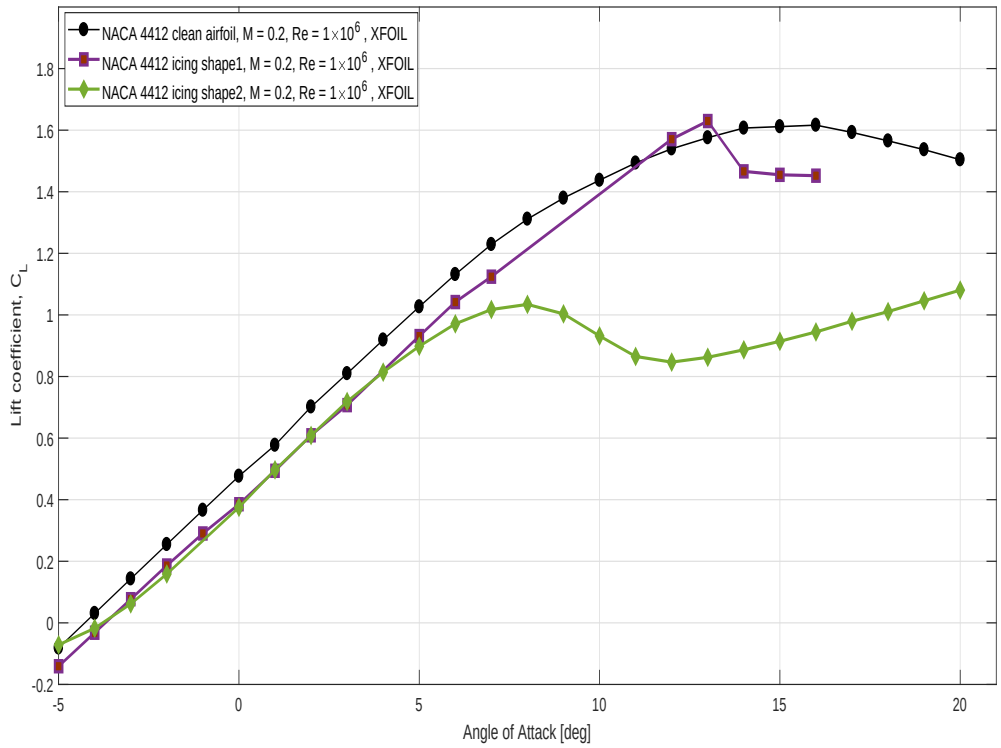

Fig. 5.11: XFoil results for NACA 4412 airfoil in clean and iced condition.

The analysis using XFoil is a reasonable method to get a quick estimate of lift, drag and moment values. However, for more accuracy and a more realistic understanding of physics of flow past ice accreted airfoils CFD is a better alternative. The Fig. 5.12 shows the comparison of results between XFoil and ANSYS Fluent for icing shape 1 installed on NACA 4412 airfoil.

The results from fluent matches with that of XFoil with in a reasonable range. The analysis in XFoil showed that there is a loss of lift coefficient slope and an earlier stall for the iced airfoil with ice shape 1. The results in ANSYS fluent shows a further loss in maximum lift coefficient from 1.6 to 1.4.

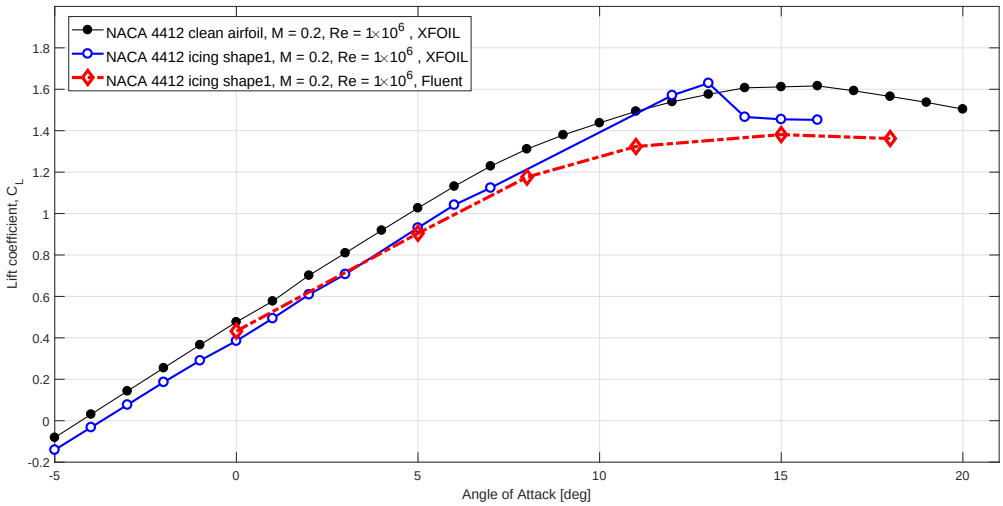

Fig. 5.12: Fluent vs. XFoil results for NACA 4412 airfoil in clean and iced condition.

5.2 Analysis of icing in Boeing-737 wing cross-sections using CFD methods

The cross sections of the Boeing 737 wing are obtained from available public domain data and plotted in ICEM CFD. The resulting airfoils starting from root to outboard superimposed on each other are shown in Fig. 5.13. Then the commonly observed horn icing shape is installed on all airfoils to analyze the aerodynamics performance using ANSYS fluent [60]. The icing shape (horn) installed on the root airfoil is shown in Fig. 5.14. The grid consisted of 50,000 elements with Y+ being less than 1 thus enabling high resolution in the boundary layer that can capture the Reynolds effects and any separation that is bound to happen.

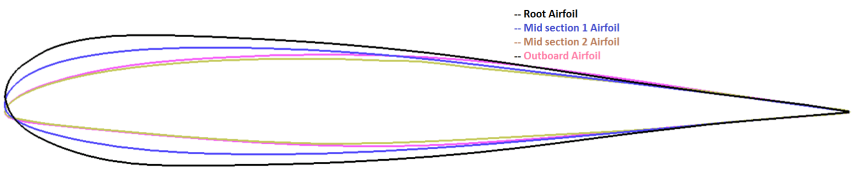

Fig. 5.13: Superimposed Airfoil cross sections of Boeing 737 wing.

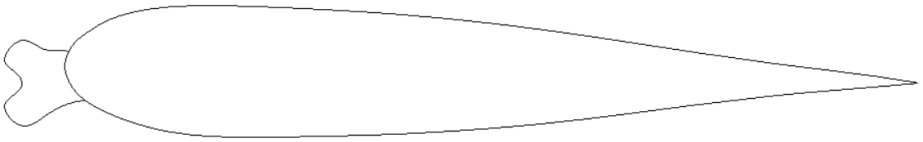

Fig. 5.14: Horn ice shape installed on Boeing 737 root airfoil .

The results acquired are shown in Fig. 5.18. The most degradation in aerodynamic perfomance in terms of loss of lift was for the root and the outboard airfoil.

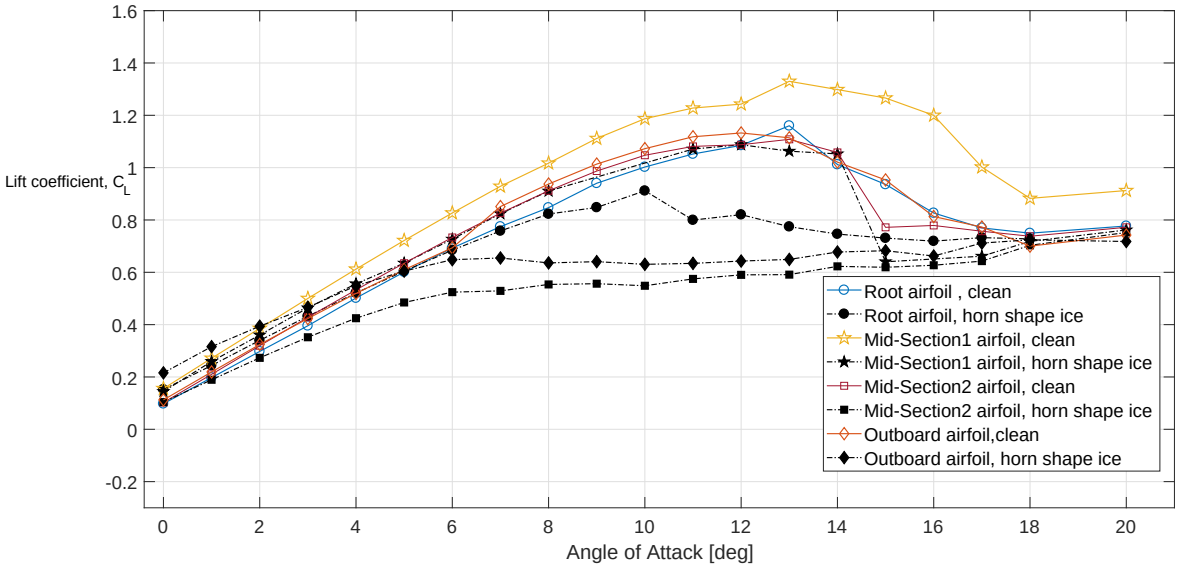

Fig. 5.15: Results for clean and iced conditions with horn ice shape for $Re = 15 \times 10^6$ and $M = 0.3$ using Shear Stress Transport(SST) model.

5.3 Analysis of 3D Boeing 737 wing with non-symmetric ice distribution

The analysis of the Boeing 737 wing body with one wing clean and ice deposited on the other wing is carried out using ANSYS fluent software. The grids are generated using unstructured tetrahedral mesher in ICEM CFD software.

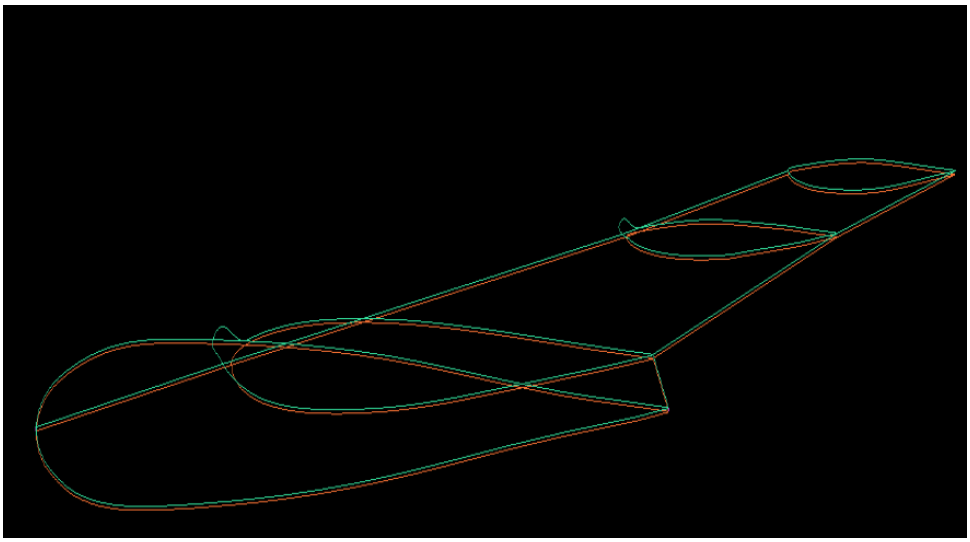

Fig. 5.16: B-737 3D clean wing(orange) and iced wing (green).

The results show that the clean right wing has a much higher maximum lift coefficient of about 1.12 while the wing with ice shape installed has a maximum lift of only 0.9.

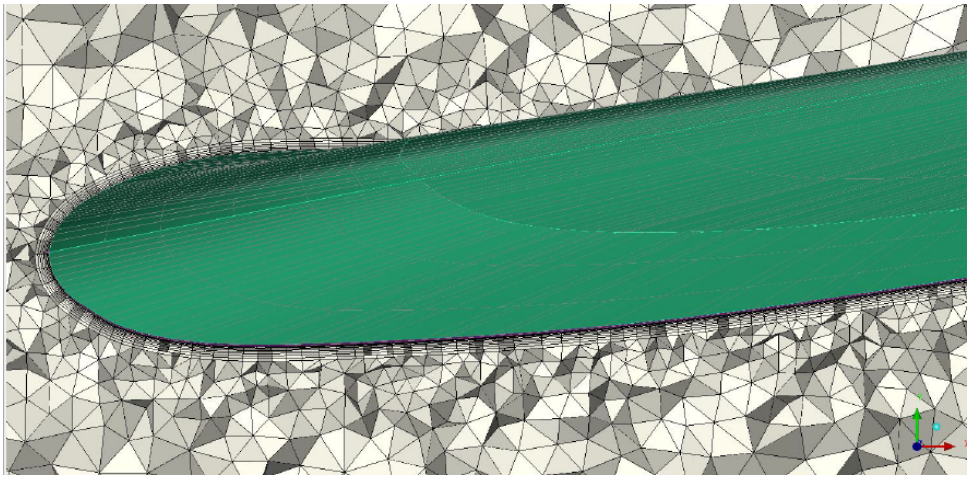

Fig. 5.17: cross section view of the generated grid for the B737 wing.

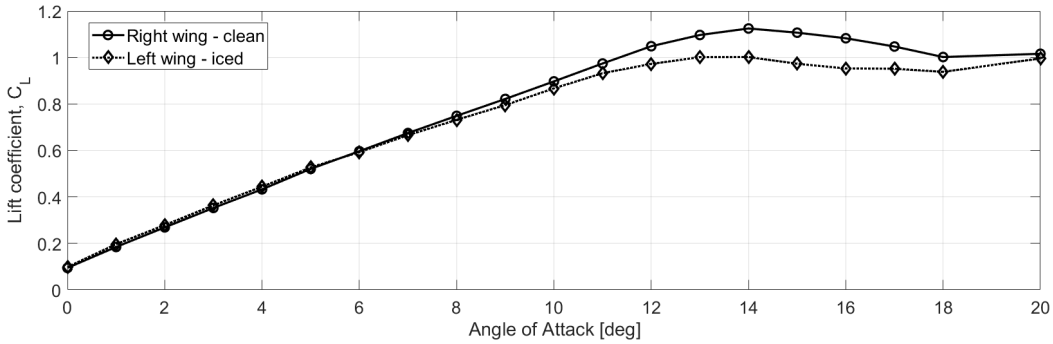

Fig. 5.18: CFD results for the 3D wings in clean and iced conditions at $Re = 15 \times 10^6$ and $M = 0.3$ using Shear Stress Transport(SST) model.

5.4 Phenomenological model for ice accretion

Phenomenological model 4.2 presented in Chapter 4 can be modified for ice accretion considering quasi-steady conditions with no hysteresis, as follows:

$$C_L = k_d C_{L_{\alpha_{att}}} g(\alpha) + C_{L_{\alpha_{det}}}[1 - g(\alpha)] \tag{5.1}$$

where:

$C_{L_{\alpha_{att}}}$	=	lift coefficient slope of attached flow regimes
$C_{L_{\alpha_{det}}}$	=	lift coefficient slope of fully separated flow regimes
$g(\alpha)$	=	flow transition function
k_d	=	degradation factor due to ice accretion in the lift slope for attached flow regimes

The function $g(\alpha)$ varies from 0 to 1, where 0 indicates fully separated flow condition. The degradation factor k_d is calculated from various experimental and simulation data. The illustration of the model (5.1) is presented in Fig.5.19.

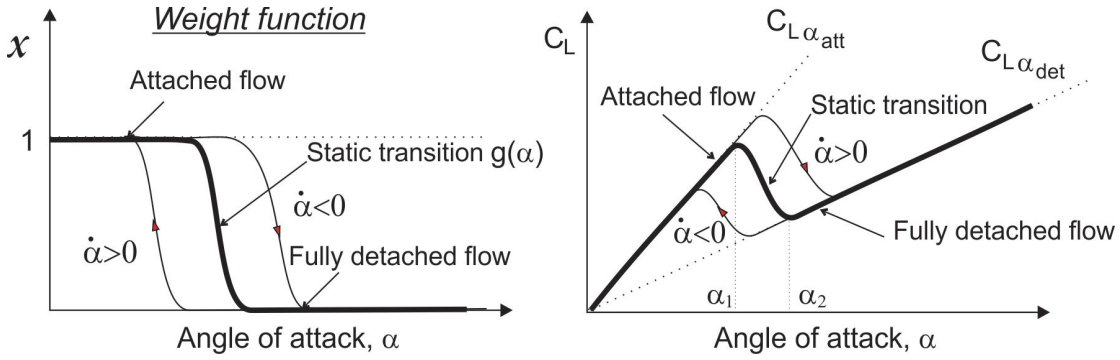

Fig. 5.19: Phenomenological modelling of ice accretion effect on the lift coefficient.

Delays in flow separation and in flow reattachment will also take place during intensive manoeuvres with high rate of change in angle of attack. To take this into account model (5.1) can be upgraded to the following form:

$$
\begin{aligned}
C_L &= k_d C_{L_{\alpha_{att}}} x + C_{L_{\alpha_{det}}}(1-x) \\
\tau_1 \frac{dx}{dt} + x &= g(\alpha - \tau_2 \dot{\alpha})
\end{aligned}
\tag{5.2}
$$

where dynamic variable x describing weight function in dynamic transitions of stall region with varying angle of attack $\alpha(t)$. Fig.5.19 shows changes of variable x at $\dot{\alpha} > 0$ and $\dot{\alpha} < 0$ and the associated variations of the lift coefficient. The presented mechanism generates so called dynamic hysteresis phenomenon. Tuning parameters in quasi-steady model 5.1 and dynamic model 5.2 allows the model to capture variety of aerodynamic responses observed in experiments and CFD simulations. Such kind of modelling is the most convenient approach for building flight simulation models covering separated flow conditions.

5.5 Concluding Remarks on Ice Accretion Effect

The phenomenon of ice accretion has been well investigated in flight and wind tunnels for various temperatures and atmospheric conditions showing types of ice shapes and their location. In this chapter, CFD simulations were used to evaluate the effect of ice accretion on aerodynamic characteristics with the objective to formulate a simple phenomenological model for application in flight simulations.

It is shown that even for 2-D airfoils the horn, rime or glaze shaped ice causes a drop in the maximum lift coefficient and leads to earlier stall. The simulation results show that the horn shaped ice accretion causes most degradation of the aerodynamic performance of an airfoil, namely the reduction in the lift force slope (see Fig. 5.11). The analysis using SST turbulence model for Boeing 737 aircraft with right wing in clean condition and the left wing iced demonstrates that the clean wing has a much higher maximum lift coefficient and stalls much later than the iced wing (see Fig. 5.18).

A simple phenomenological model for evaluation of ice accretion effect on aerodynamic performance has been proposed in this chapter.

Chapter 6

Ground Effect Aerodynamcis

According to statistics of fatal accidents worldwide for the commercial jet fleet during the period $2006 - 2015$ presented by Boeing Company Ltd the number of fatalities during landing due to Abnormal Runway Contact (ARC) and Runway Excursion (RE) holds is second place to that of controlled flight into terrain (CFIT) after the Loss-of-Control in Flight (LOC-I) [1]. Approach and landing accident reduction (ALAR) is the primary goal of the Flight Safety Foundation (FSF) [2]. It is noted that a better knowledge of flight dynamics in close proximity to the ground can provide increased understanding of the various crosswind handling techniques to increase safety during a crosswind landing [2].

Aircraft aerodynamic characteristics and dynamic behavior are subjected to changes in proximity to the ground during landing approach and take-off flight [62]. An increase in the lift force, reduction in the amount of induced drag and onset of the pitch down moment requires control actions from the pilot for re trimming the aircraft. The above mentioned aerodynamic changes due to ground effect in the aircraft longitudinal dynamics and control are well recognized. Special wind tunnel techniques are used for evaluation of the ground effect in the longitudinal aerodynamic characteristics [63]. An analytical study of the ground effect on the airplane longitudinal stability can be found, for example, in paper [64].

During crosswind landing and take-off the aircraft lateral-directional dynamics can be excited. Aircraft can be approaching and landing with side slip and nonzero bank angle; this requires leveling aircraft in close proximity to the runway. Therefore the effect of closeness to the ground on the lateral-directional aerodynamic characteristics in such situations should be seriously evaluated. The lateral-directional airplane dynamics due to ground effect have been under studied in the aeronautical literature and not introduced in the flight simulation practice.

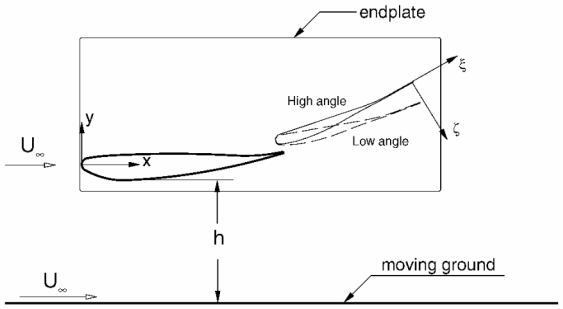

Fig. 6.1: Schematic for double element racing car wing in ground effect from [65].

One of the prior mentioned phenomena causing loss of control in flight is ground effect during departure and landing. In ground effect, the lift coefficient C_L increases and the C_D decreases due to the increased pressure on pressure side of the wing in close proximity to the ground/runway. There are many wind tunnel results and computational simulation results proving the changes in aerodynamic coefficients for a flight in ground effect aerodynamics.

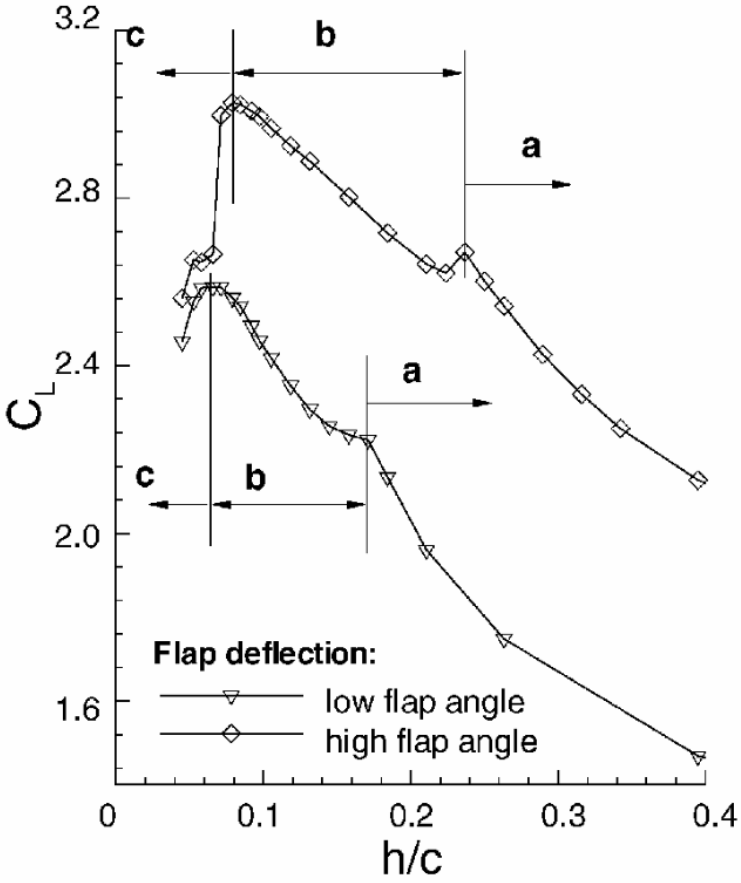

Fig. 6.2: C_L results for double element wing in ground effect from [65].

The ground effect in the case of a cambered, double element wing was studied

experimentally in [65]. The idea behind the experimental setup is shown in Fig.6.1. The results indicate a significant increase in the lift coefficient as the h/c (height from ground to chord length of airfoil ratio) decreases. Furthermore, at high flap angle the lift coefficient C_L increases as shown in Fig. 6.2.

In another research work, aerodynamic investigation of RAE 2822 airfoil in ground effect using computational methods was carried out in [66]. The work in [66] was done using CFD methods at different h/c ratios and different turbulence models and showed that realizable k-ϵ gave most accurate results. Usually, the maximum L/D ratio is obtained in the medium angle of attack region.

Apart from analysis of ground effect in normal conditions, in [67] numerical analysis of banked wing in ground effect was considered. The work in [67] shows that for a wing in banking and ground effect, the descending side produces more lift and less drag. This leads to a righting moment and adverse yaw moment. But for the same considered case, when a delta wing was used, less right moment and yaw moment was generated.

There have also been studies in which dynamic motion of the aerodynamic body in ground effect was considered [39, 40]. The effect of ground on flapping insect wings in forward-flight at a Reynolds number of 150 was studied using Lattice Boltzmann and immerse boundary methods for different frequencies. The results for the mentioned analysis in terms of instantaneous vorticity contours from [39] are shown in Fig. 6.3.

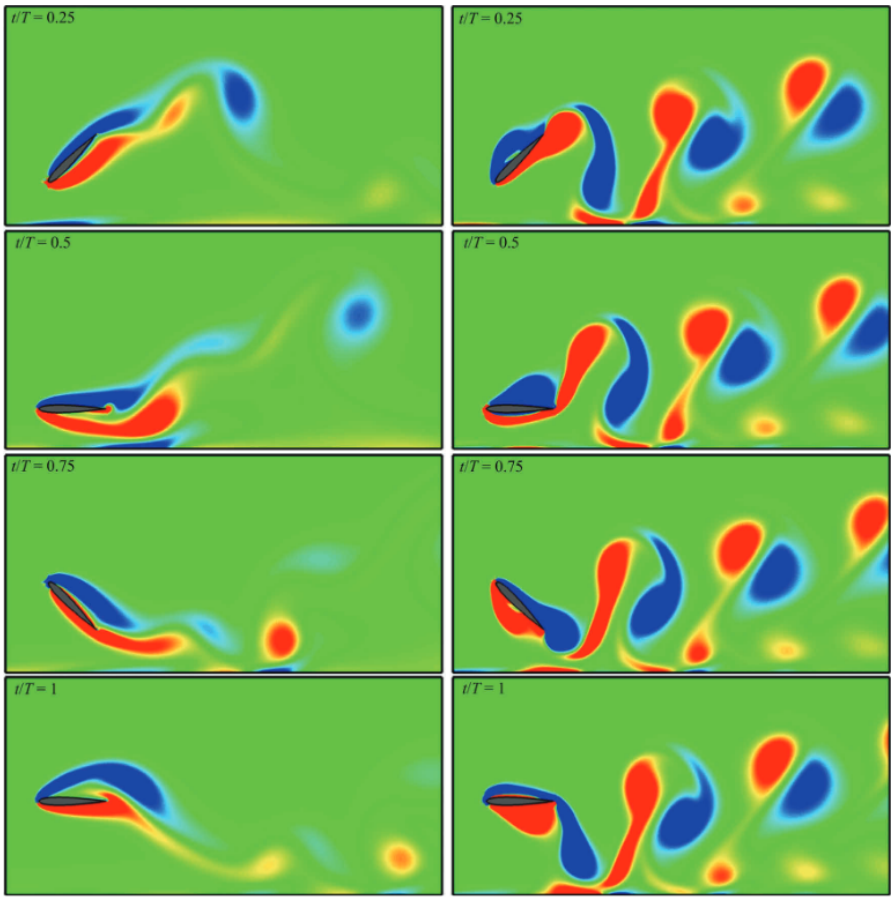

Fig. 6.3: Instantaneous vorticity contours for a flapping insect wing from [39].

The previous mentioned research mostly belongs to the subsonic regime of flight. In [68] a detailed review of significant achievements in ground effect aerodynamics in sub/trans/super/hyper sonic regions was presented. The results in the case of ground effect for compressible flows are shown in Fig. 6.4. The C_p differences when tested with a steady state incompressible solver and unsteady compressible with $\delta t = 0.0024s$ are also presented and seem to be significantly different (see Fig. 6.4).

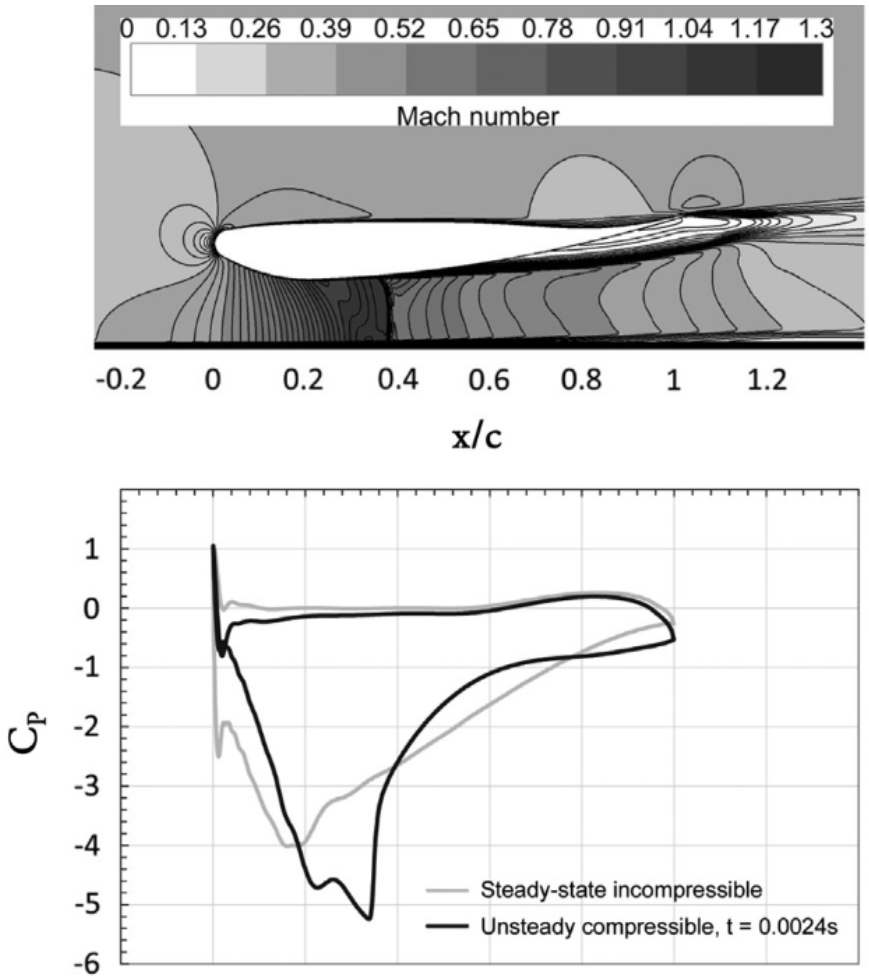

Fig. 6.4: Compressible ground effect aerodynamics from [68].

The ground effect aerodynamics in an airfoil following heaving and pitching trajectory is presented in [69]. The simultaneous pitching and heaving trajectory is shown in Fig. 6.5.

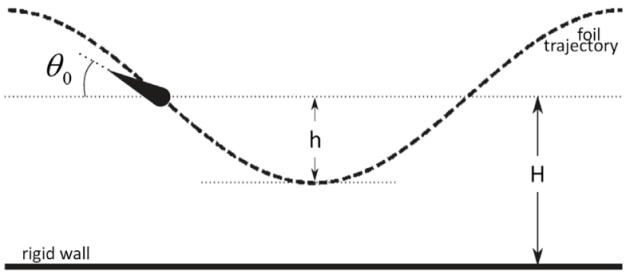

Fig. 6.5: *Heaving pitching foil in ground effect from [69].*

In [69] the effect of wall proximity on propulsive flapping foil was considered.

The motion accompanies a sinusoidal heave and angle of attack. The factors that were varied was the maximum angle of attack, the distance from ground/wall and the Strouhal number. The effect of distance of wall away from the foil had a huge impact on the measured mean lift and thrust value.

Apart from force coefficients in the case of ground effect there have been some studies analyzing the stability of aircraft in ground effect such as the work in [64]. In this study, for an aircraft in ground effect, the longitudinal stability was analyzed and discussed.

However, it is still noted that much more wind tunnel, computational and analytical models needs to be carried out to study the ground effect aerodynamics in the case of extreme cross winds, roll-yaw-pitch derivatives, etc. Therefore, a need for more computational and experimental tests still exists. In wind tunnel analysis, the techniques and capabilities such as used in Filton Low speed wind tunnel [63] are favored.

6.1 NACA 4412 airfoil with Flap in close proximity to ground

In this section, the computational analysis of a cambered airfoil NACA 4412 in close proximity to the ground is carried out using OpenFOAM software. The analysis consists of 1) static non-moving airfoil in varying height/chord ratio from the ground and 2) dynamic-moving airfoil in varying height/chord ratio from the ground. The grid generated for the simulation is made up of two fluid domains such that the circular region can rotate if desired (see Fig. 6.6). The grid consisted of 45,000 elements with Y+ being less than 1 near walls of the airfoil and the ground.

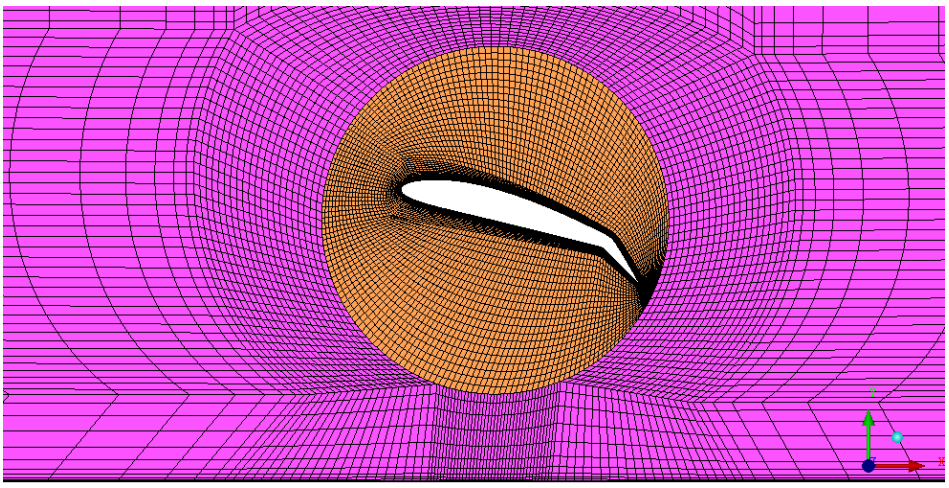

Fig. 6.6: Generated grid for simulations of static and dynamic hysteresis in ground effect.

Such a grid allows rigorous dynamic moving mesh methods and is favored for these kind of simulations. Furthermore, the inbuilt codes in OpenFOAM for cyclic

patching and data transfer between the walls of two fluid domains allows smooth data transfer thus keeping the integrity of the true solution.

The simulation was carried out using the SA turbulence model and transient simple (unsteady) algorithm with or without the dynamic mesh solver depending if the case was static or dynamic. The results for static tests as shown in Fig. 6.7 demonstrates that the lift coefficient increases with the decrease of height/chord ratio. Furthermore, the results for simulation in which there was no ground effect matches well with experimental results.

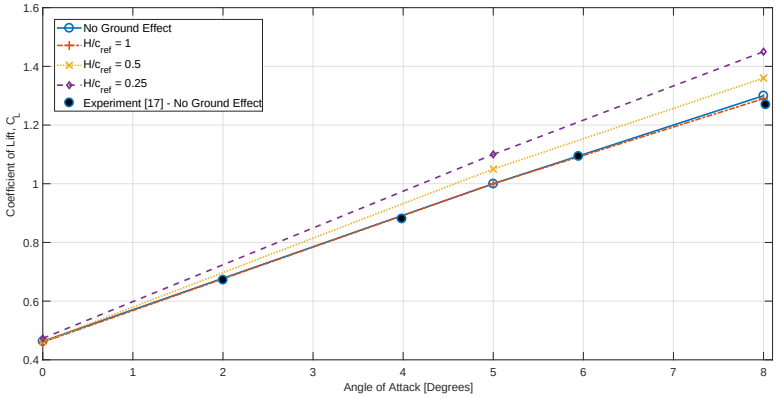

Fig. 6.7: Lift coefficient C_L against α at $Re = 6 \times 10^6$ for NACA 4412 airfoil in Ground Effect.

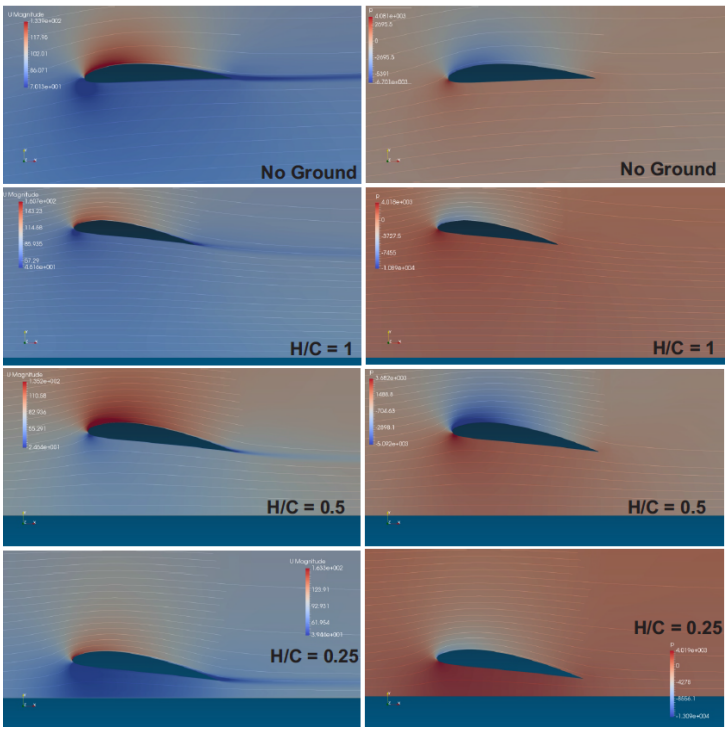

Fig. 6.8: Visualization of streamlines superimposed on velocity (left) and pressure(right) contours for NACA 4412 airfoil.

The simulation visualization with streamlines of the solution superimposed on velocity and pressure contours are shown in Fig. 6.8. The increase of pressure on the suction side of the airfoil is clearly shown to increase with decrease of height to chord ratio.

In Fig. 6.9 the dynamic loop analysis results are shown for the NACA 4412 airfoil with Flap r No-Flap and altering height/chord ratios. It can be seen that the flap increases the lift coefficient as one would expect from classical results. But more interestingly, it is evident that the decrease of h/c ratio from 2 to 1 leads to an enormous increase of lift coefficient and also widens the dynamic hysteresis loop.

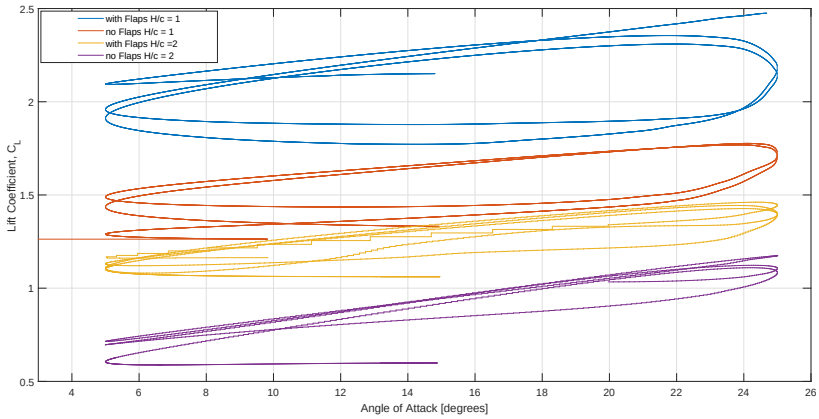

Fig. 6.9: Dynamic loops at reduced frequency of $k = 0.2$ for lift coefficient C_L against α at $Re = 6 \times 10^6$ NACA 4412 airfoil w/o flaps in Ground Effect.

6.2 Ground Effect Analysis of Common Research Model(CRM-NASA)

The ground effect in the CRM aerodynamic forces and moments dependencies has been identified in the CFD simulations and the obtained aerodynamic data were applied for stability and controllability analysis in the lateral-directional airplane motion. The performed dynamic analysis for a typical transport airliner showed transformation of the airplane lateral-directional modes of motion. For example, the roll subsidence and spiral eigenvalues in close proximity to the ground are merging creating the oscillatory Roll-Spiral mode with quite significant frequency. This transformation of the lateral-directional dynamics introduced in piloted simulation may affect the flight simulator motion-cueing and handling quality characteristics. The major factor of the performed ground effect dynamic analysis was the introduction of the rolling and yawing moments dependencies on the airplane bank angle, which was equivalent to the "aerodynamic banking stiffness". The airplane responses to ailerons and rudder control inputs also change in close proximity to the ground. The formulation of the computational framework and simulation results for CRM ground effect aerodynamics are presented in section 6.2.1. Section

6.2.2 discusses the results of dynamic analysis of the lateral-directional motion and the 6-DOF simulations of the full scale flight simulation model in close proximity to the ground.

6.2.1 CFD simulation of ground effect aerodynamics

For evaluation of the ground effect aerodynamics in this study the Common Research Model (CRM) geometry of a generic airliner was selected. This geometry of CRM in wing-body-horizontal tail configuration is available on the NASA repository for Drag Prediction Workshop [70]. The geometry is then modified to include the ONERA vertical fin available at [71]. The reference area for CRM model, shown in Fig.6.10, is $S_{ref} = 383.7m^2$ and $C_{ref} = 7m$, the wing has an aspect ratio of $AR = 9.0$. The modified geometry of CRM model is shown in Fig. 6.10.

Fig. 6.10: Full configuration of the Common Research Model (CRM).

Grid generation

The build topology of the CRM model has been checked and corrected to ensure air tightness on the model surfaces. After this procedure a hexahedral type of mesh was generated for the full model. A structured mapped blocking approach with appropriate splits and inclusion of O-grids was used to better capture the boundary layer regions on the airplane surfaces. Different views of the grids generated are shown in Fig. 6.11, 6.12 and 6.13.

The blocks initially generated, were transformed through rotations and translations to generate hexahedral unstructured meshes according to flight conditions, i.e. airplane attitude and closeness to the ground. The boundary conditions on the ground were implemented as a moving wall with direction and velocity magnitude of incoming flow and were resolved with inclusion of H-grid layers with appropriate wall distance (Y+$\leq$ 1).

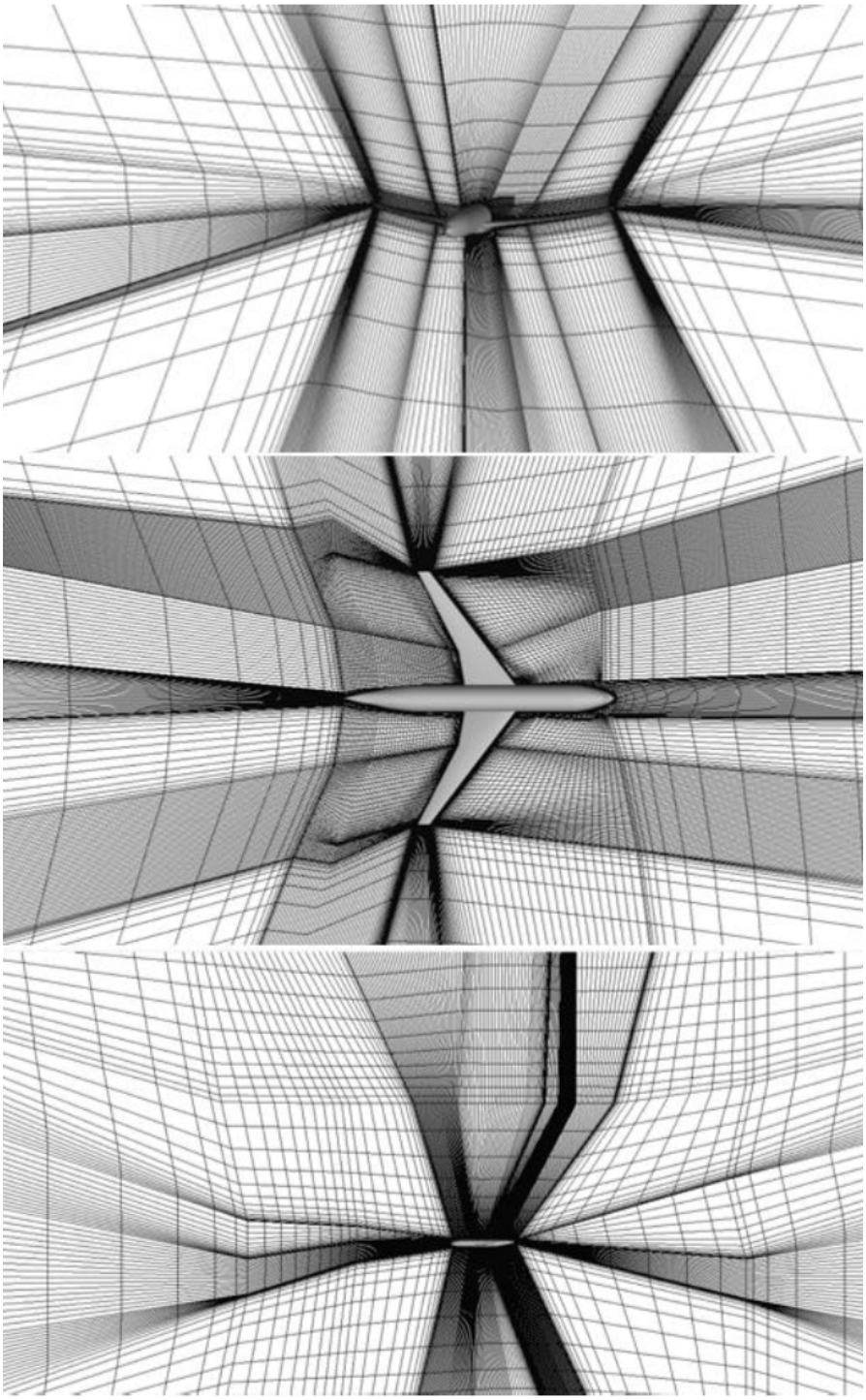

Fig. 6.11: Slice view for the grids far away from ground, front top and side view.

The initial meshes were generated for different altitudes above the ground $h = 4\bar{c}$, $h = 2\bar{c}$, $h = 1\bar{c}$, and $h = 0.5\bar{c}$. At each altitude h the grid was adapted for a number of different angle of attack settings $\alpha = 4, 8, 12°$. At altitude $h = 0.5\bar{c}$ additionally a number of bank angle settings was considered $\phi = 4, 8, 12°$ with additional adaptation of the grid. Fig. 6.13 shows different CRM attitudes at $h = 0.5\bar{c}$ (different colors are used to highlight different aerodynamic surfaces of

the model). The blue mesh in the bottom represents the ground.

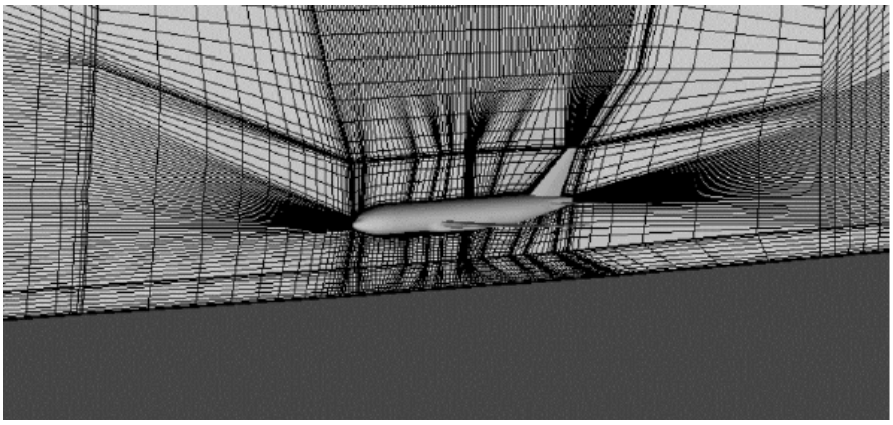

Fig. 6.12: Slice view of symmetry plane of the grid for $h/c = 1$, close proximity to ground.

The numerical simulations were carried out within reasonable accuracy of a grid between coarse to medium, i.e. 10million cells for a full configuration. This seems suitable for our purpose here to evaluate ground effect.

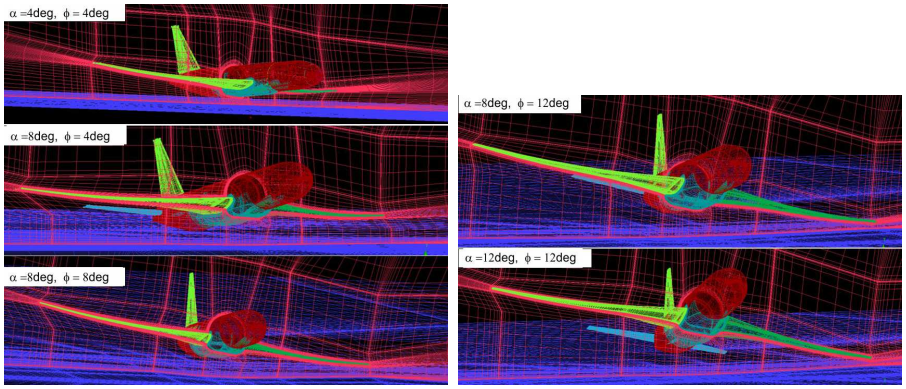

Fig. 6.13: Generated meshes and flight settings at different α and ϕ for $h = 0.5\bar{c}$.

Governing equations and boundary conditions

The Navier-Stokes equations governing incompressible fluid flow are:

$$\nabla \cdot u = 0 \tag{6.1}$$

$$\frac{\partial u}{\partial t} + (u \cdot \nabla)u - \nu \nabla^2 u = -\nabla p/\rho \tag{6.2}$$

For the Reynolds numbers typical for industrial applications, the computational resources required for a Direct Numerical Simulation (DNS) of equations (6.1),(6.2) are exceeding the currently available technical capabilities. The effect of turbulence is normally simplified by solving the Reynolds-averaged Navier-Stokes (RANS) equations, which are the time averaged approximation of equations

(6.1),(6.2). The averaging of fluctuating velocities generates additional terms, known as the Reynolds stresses. To describe these stresses the additional empirical equations, generally differential ones, are required to close the computational model. The majority of RANS models are based on the concept of an eddy viscosity, equivalent to the kinematic viscosity of the fluid, that describes the turbulent mixing or the diffusion of momentum. For closure, the turbulence k-ω SST formulation is used which is commonly used in computational aerodynamic simulations[17]:

$$\frac{\partial \rho k}{\partial t} + \frac{\partial u_j k}{\partial x_j} = G - \beta^\star \rho \omega k + \frac{\partial}{\partial x_j}\left[(\mu + \sigma_k v_t)\frac{\partial k}{\partial t}\right] \tag{6.3}$$

$$\frac{\partial \rho \omega}{\partial t} + \frac{\partial u_j \omega}{\partial x_j} = \frac{\gamma}{\nu_t} G - \beta \rho \omega^2 + \frac{\partial}{\partial x_j}\left[(v + \sigma_\omega v_t)\frac{\partial \omega}{\partial t}\right] + D \tag{6.4}$$

where turbulent viscosity is defined as:

$$v_t = \frac{\rho a_1 k}{max(a_1 \omega, \Omega F_2)} \tag{6.5}$$

Solver and numerical settings

The ground effect aerodynamics was simulated using the steady-state solver for the Reynolds Averaged Navier-Stokes (RANS) equations closed by the k-ω SST model for turbulence. Under relaxation is applied for solution of steady RANS equations to increase convergence stability. Second order discretization schemes were used to solve momentum and pressure equations. All scalar variables are solved with the first order accuracy. The residuals for all the equations are allowed to reach a satisfactory convergence of $1/10000^{th}$ of the initial values.

Simulation results

In close proximity to the ground the airplane wing tip vortices are modified giving a reduced downwash contribution. This leads to increase in the lift force, reduction in the amount of induced drag, onset of the pitching down moment. For illustration purposes, Fig. 6.16 shows a pressure distribution on the CRM surfaces, the ground and in a far field cross-section at flight with altitude $h = 0.5\bar{c}$, angle of attack $\alpha = 8^\circ$ and bank angle $\phi = 4^\circ$. Note, the wing closer to the ground has a much weaker tip vortex than a similar vortex on the upper wing, which appears to be slightly elliptical. There is also zones with increased pressure on the ground under the wing and horizontal tail.

Transformations of the wing tip vortices in ground effect produce changes in the aerodynamic forces and moments acting on the aircraft. Fig.6.19 presents simulated dependencies for the lift, drag and also for the pitching, rolling and yawing moment coefficients. The ground effect increments in the aerodynamic loads increase with increase of the magnitude of the lift and strengthening the wing tip vortices and downwash outside of the ground. For example, at $\alpha = 8^\circ$ and zero bank angle $\phi = 0$ the increase in the lift coefficient is $\triangle C_L = 0.08$, which

is equivalent to increase on 11.2% (see Fig.6.19, top left plot). Further increase in the lift coefficient takes place at bank angle $\phi = 12°$ - $\triangle C_L = 0.217$, which is equivalent to increase on 28.7% (see Fig.6.19, top right plot). The drag coefficient at bank angle $\phi = 12°$ decreases, $\triangle C_D = -0.013$, this is equivalent to decrease on 11.8% (see Fig.6.19, top right plot).

The contours and streamlines of velocity and pressure for various flight attitudes are shown in Fig. 6.14, 6.15, 6.16 and 6.17.

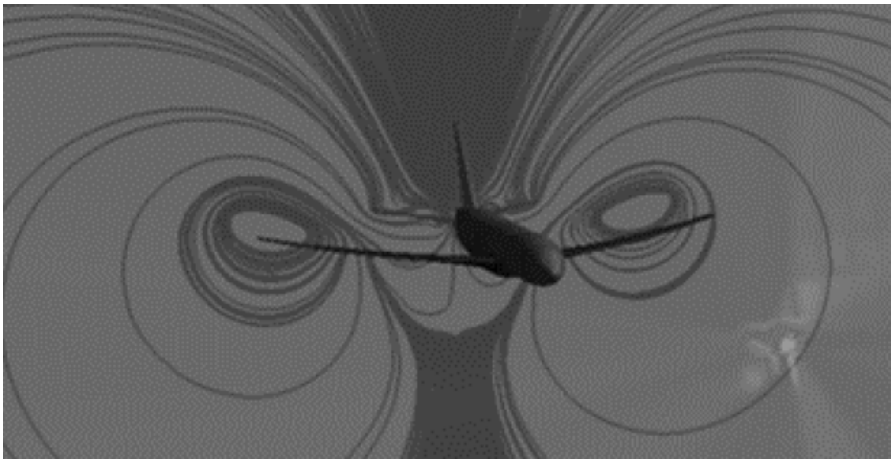

Fig. 6.14: Streamlines showing vortices's behind the aircraft for no ground effect, $\alpha = 0°$ and $\phi = 0°$.

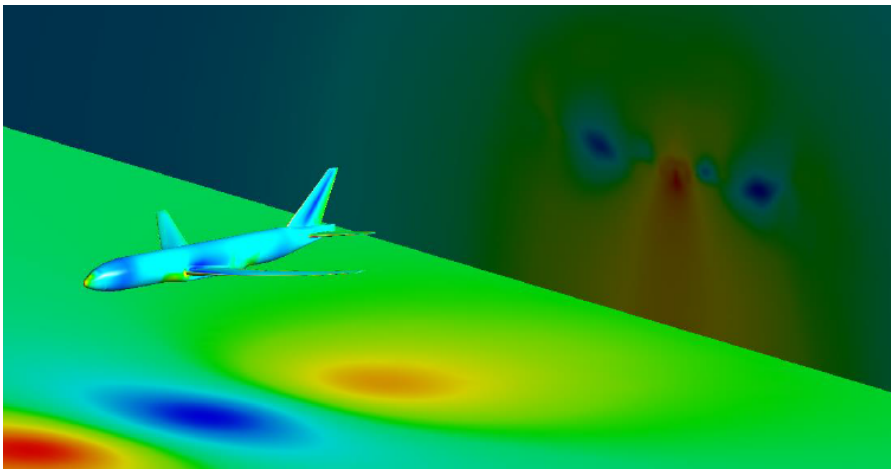

Fig. 6.15: Pressure contours showing vortices's behind the aircraft for $h = 1\bar{c}$ $\alpha = 0°$ and $\phi = 0°$.

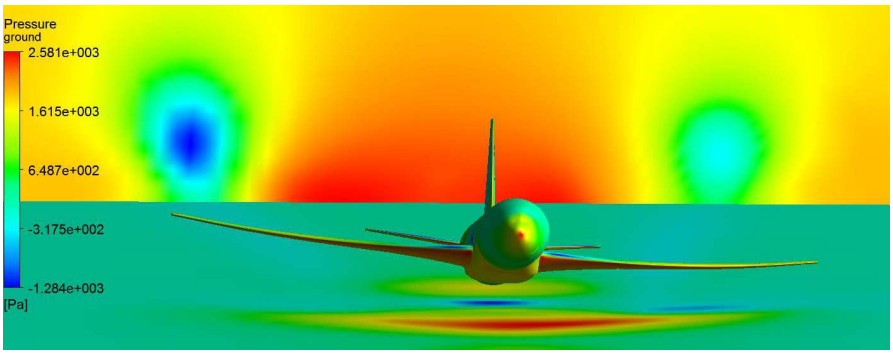

Fig. 6.16: Pressure distribution on CRM model and inserted plane behind aircraft at $h = 0.5\bar{c}$, $\alpha = 8°$ and $\phi = 4°$.

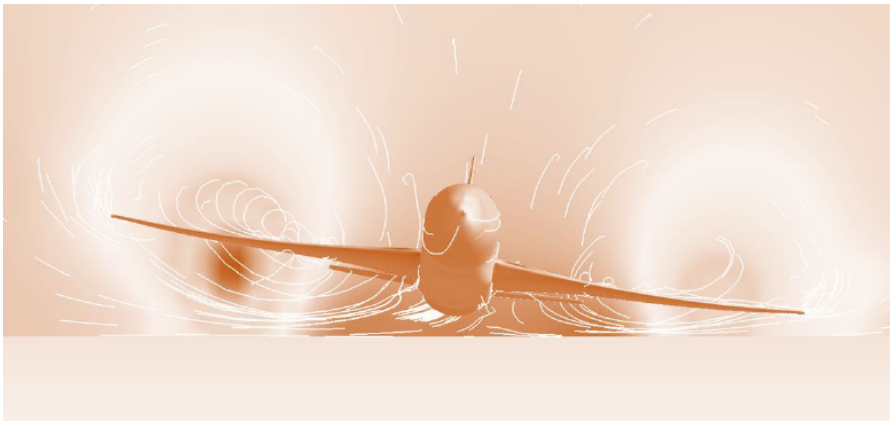

Fig. 6.17: streamlines imposed on pressure contours for CRM model and inserted plane behind aircraft at $h = 0.5\bar{c}$, $\alpha = 8°$ and $\phi = 8°$.

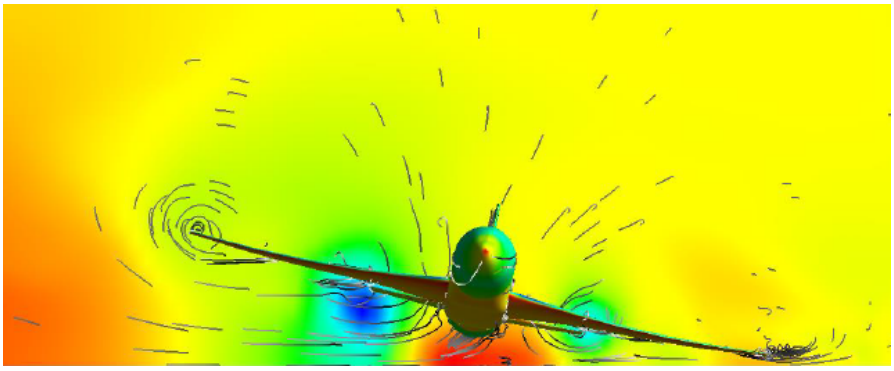

Fig. 6.18: streamlines imposed on pressure contours for CRM model and inserted plane behind aircraft at $h = 0.5\bar{c}$, $\alpha = 8°$ and $\phi = 12°$.

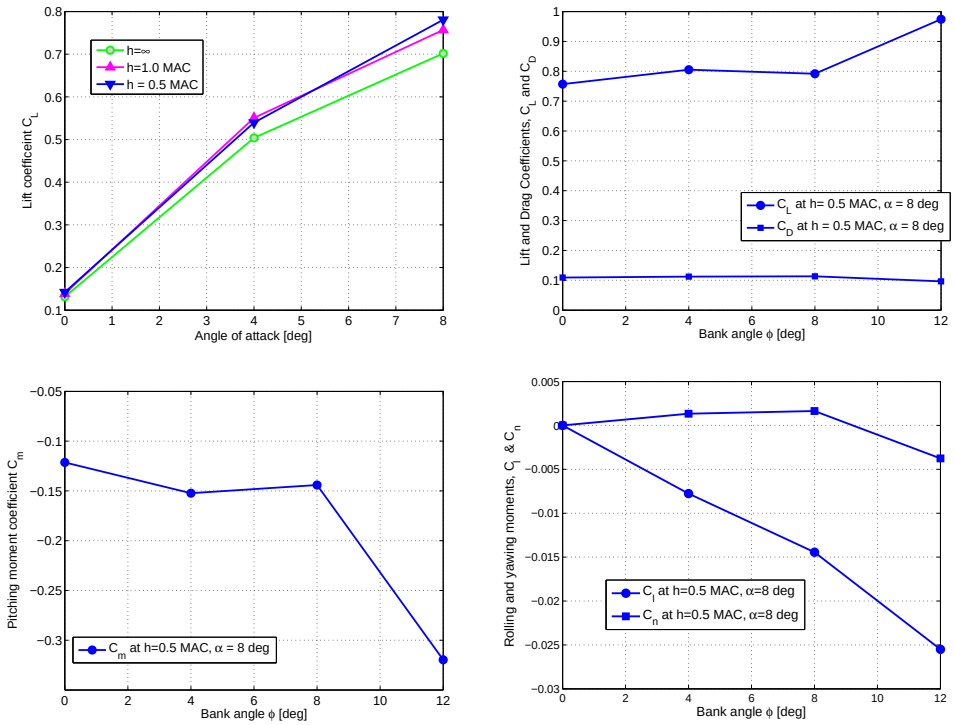

Fig. 6.19: Effect of bank angle on aerodynamic coefficients C_L, C_D, C_m, C_l, C_n at $h = 0.5\bar{c}$, $\alpha = 8°$.

The aerodynamic moments are also affected by the bank angle in close proximity to the ground. There is a significant pitching down effect at $\phi = 12°$, i.e. $\triangle C_m = -0.198$ (see Fig.6.19, bottom left plot). The most important for our objectives are the rolling and yawing moment dependencies on bank angle, shown in Fig.6.19, bottom right plot. The rolling moment coefficient C_l proportionally decreases with increase of bank angle ϕ, which is acting in a way as a stiff spring. The yawing moment coefficient increases with increase of bank angle until $\phi = 8°$, but decreases with a change of sign at $\phi = 12°$ (see Fig.6.19, bottom right plot).

High lift configuration

The ground effect in aerodynamic characteristics is proportional to the lift force. For CRM configuration we considered a high angle of attack runway approach. An aircraft normally approach landing with deployed leading and trailing edge flaps, which produce a high lift at low angles of attack. In this section preliminary set up for a high lift configuration is presented, which is described below.

Geometry A hybrid model is constructed by combining the Wing Body configuration (F11) provided in the 2nd AIAA High Lift Prediction workshop[72] and the General Transport Model (GTM) provided in Open VSP Hangar [73]. This is successfully done by trimming the Vertical and Horizontal stabilizers along with fuselage rear end at roughly 3/4 from the nose. The Geometry is then also simplified for CFD by cleaning up in terms of topology. Surfaces are further simplified

and merged together to automate the ease of blocking with caution such that the authenticity of the model is not lost and the geometry is not violated.

The reference area for this model is $419,130$ mm^2 for the half model and the Mean Aerodynamic chord length of $347.09mm$ is at quarter chord along span. The flaps are deflected down at 32 degrees and the slats are deflected at 26.5 degrees.

preliminary results The grid for this particular configuration is structured using Hexa-8 and quad-4 elements. The hexa elements are ideally 8 node elements in 3D space, and 2D quads are 4 node elements. Such a grid is made using blocking and mapping the blocks to the model interested. The current mesh contains more than 1500 blocks and hence for complex full flight configurations such as F-11 high lift aircraft, it is difficult to maintain mesh quality in terms of orthogonality, skewness and aspect ratio for such a mesh. This becomes more of a problem when specially applied to the small gaps in between the flaps, slats and the main wing as we need to resolve the boundary layer for each of them separately but also maintain connectivity in mesh such that they are resolved as one structure as well.

However, as seen in Fig. 6.20 and 6.21, the special blocking allows us to control the boundary layer from flaps, slats and wing without having them collapse each other. This is one of the main advantages of using a structured blocking approach for such configurations along with other benefits such as reduction in cell count, higher quality meshes and more flexible and solvable by matrix solvers as the nodes are in a much regulated order.

The grid generation also follows the guide lines given by the High Lift Prediction Workshop [72]. A coarse mesh according to [72] should have the wall spacing of $Y+ = 1$ and is $y = 0.00055mm$. With the increase in mesh size a proportional decrease in wall distance y, should be brought. It is also advised that at least the first 2 layers in boundary should have a constant cell spacing. A minimum of at least 4 cells is recommended in the trailing edge for a coarse mesh and the boundary growth are to be at the ratio of ¡ 1.25. The spacings should be roughly 0.1% of the span wise and chord wise local lengths of parallel to the direction of grid. Furthermore, as common practice indicates, the far field is at least 100 C_{ref} away from the body in every direction. The grids are intended for the landing conditions of $Re = 15.1$ million and the same grids are recommended to be used for lower Reynolds tests as well.

The preliminary results in Fig. 6.22 shows that the ground effect has a huge impact on the lift coefficient of the DLR F11 model. The increase in lift due to the close proximity to ground runway for F11 model is roughly 20 percent for $\alpha = 0$ degrees.

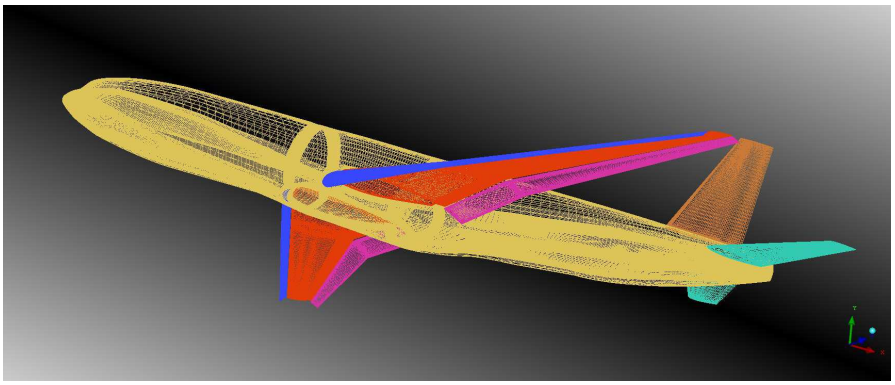

Fig. 6.20: Isometric wireframe view of the surface Grid F11-GTM model.

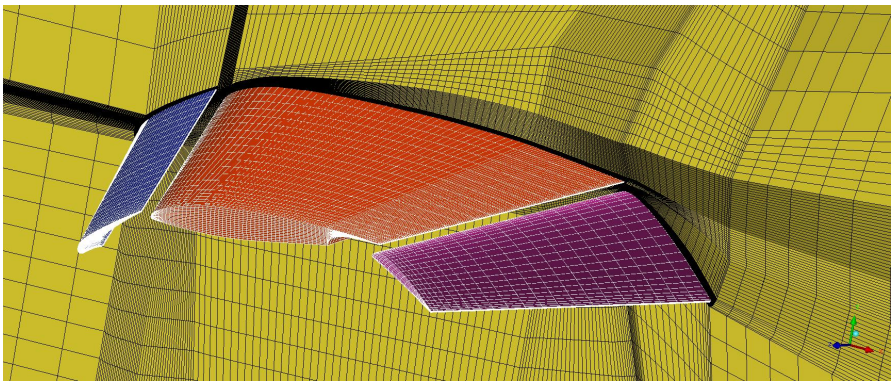

Fig. 6.21: Scan plane cut through volume mesh for F11-GTM model.

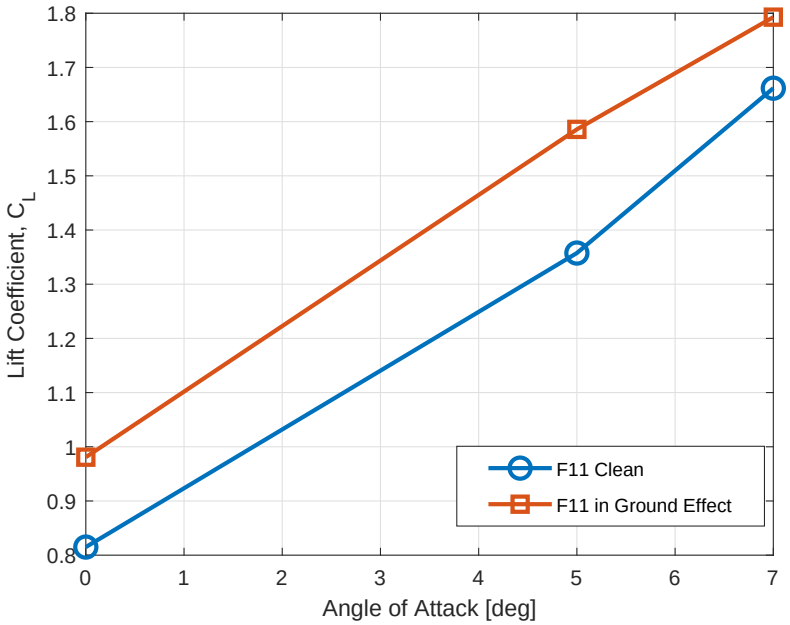

Fig. 6.22: Simulation results for lift coefficient, F11-GTM model.

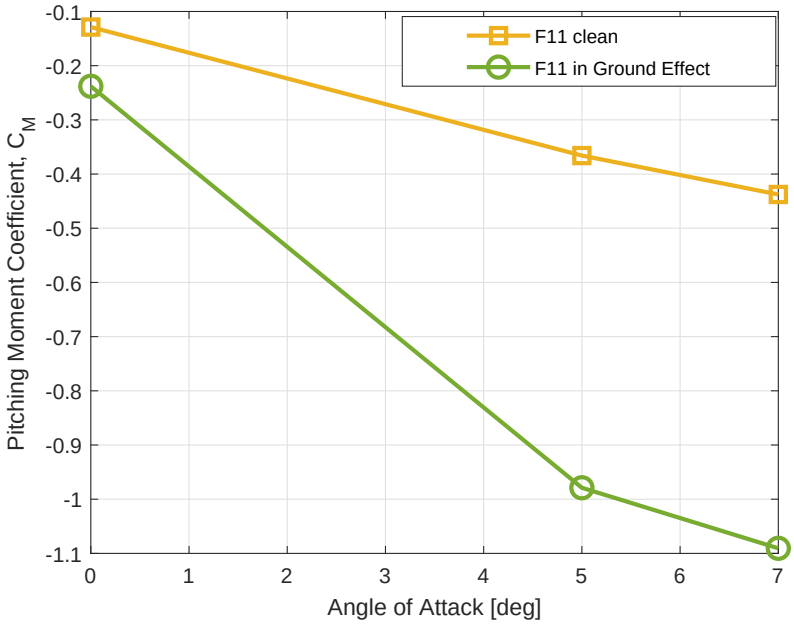

Fig. 6.23: Simulation results for Pitching moment, F11-GTM model.

6.2.2 Airplane lateral-directional dynamics in close proximity to the ground

The obtained in CFD simulations dependencies for the aerodynamic coefficients, presented in the previous section, have been used for modification of the full flight simulation model of a typical transport aircraft for conducting 6-DOF simulations in a level trimmed flight in close proximity to the ground. Trim and linearization procedures have been applied to evaluate aircraft stability conditions and small amplitude modes of motion in the longitudinal and lateral-directional motion. Additionally, the impact of ground proximity on stability of the lateral-direction dynamics is addressed in this section by the analysis of the linearized lateral-directional equations eigenvalues.

Lateral-directional equations

For evaluation of the airplane lateral-directional dynamics in close proximity to the ground the stability-axis lateral-directional equations are considered in the following vector-matrix form.

$$\begin{vmatrix} \dot{r} \\ \dot{\beta} \\ \dot{p} \\ \dot{\phi} \end{vmatrix} = \begin{bmatrix} N_r & N_\beta & N_p & N_\phi \\ -1 & \bar{Y}_\beta & 0 & \frac{g}{V} \\ L_r & L_\beta & L_p & L_\phi \\ 0 & 0 & 1 & 0 \end{bmatrix} \begin{vmatrix} r \\ \beta \\ p \\ \phi \end{vmatrix} + \begin{bmatrix} N_{\delta_a} & N_{\delta_r} \\ 0 & 0 \\ L_{\delta_a} & L_{\delta_r} \\ 0 & 0 \end{bmatrix} \begin{vmatrix} \delta_a \\ \delta_r \end{vmatrix} \tag{6.6}$$

The new terms in the state matrix of equations (6.6) are $N_\phi = C_{n_\phi}(\bar{h})\frac{\rho V^2 Sb}{2I_{zz}}$ and $L_\phi = C_{l_\phi}(\bar{h})\frac{\rho V^2 Sb}{2I_{xx}}$. They represent the rolling and yawing accelerations induced by bank angle ϕ. The ground effect in this case is equivalent to a kind of "aerodynamic roll stiffness", which will tend to level the airplane above the runway.

In flight away from the ground, when $N_\phi = L_\phi = 0$, the lateral-directional modes are defined by the Roll-Dutch complex-conjugate eigenvalues $\lambda_{DR} = -\zeta \pm \omega_n\sqrt{(}1-\zeta^2)$, the roll subsidence eigenvalue λ_R and the spiral mode eigenvalue λ_S. It is reasonable to represent the ground effect on the eigenvalues in the form of a root-loci with a parameter connected with variation of the reduced flight altitude $\bar{h} = h/\bar{c}$.

Oscillatory Roll-Spiral mode in lateral-directional dynamics

The lateral-directional characteristic equation with account of ground effect can be represented in the following form:

$$(s-\lambda_S)(s-\lambda_R)(s^2+2\zeta\omega_n+\omega_n^2)_{DR} - L_\phi(s^2+a_1 s+a_0)_{GE} = 0 \tag{6.7}$$

where

$$\begin{aligned} a_1 &= \frac{N_\phi}{L_\phi}L_r - N_r - \bar{Y}_\beta \\ a_0 &= N_\beta - \frac{N_\phi}{L_\phi}L_\beta + \left(N_r - \frac{N_\phi}{L_\phi}L_r\right)\bar{Y}_\beta \end{aligned} \tag{6.8}$$

Parameter L_ϕ varies from zero value in flight with no ground effect ($\bar{h} = \infty$) to its maximum value in close proximity to the ground ($\bar{h} = 0.5 \div 1.0$). The N_ϕ/L_ϕ ratio in expressions a_1 and a_2 (6.8) has a weak dependence on reduced altitude $\bar{h}$. So, with increase of parameter $|L_\phi|$ the eigenvalues will move on the complex plane from their initial values $\lambda_{DR} = -\zeta \pm \omega_n\sqrt{(}1-\zeta^2)$,$\lambda_R$ and λ_S towards the values defined by zeros z_1, z_2 of the second order polynomial equation $s^2 + a_1 s + a_0 = 0$ and one pair of eigenvalues will migrate to infinity. The location of zeros z_1 and z_2 depends on lateral directional coefficients in the expressions for a_1 and a_0 (6.8). These zeros can be located in the left half of the complex plane, being a complex-conjugate pair, or move to the right unstable half of the complex plane creating an opportunity for onset of oscillatory instability due to ground effect, when $a_1 < 0$. There is also a possibility for onset of aperiodical instability due to ground effect if $a_0 < 0$.

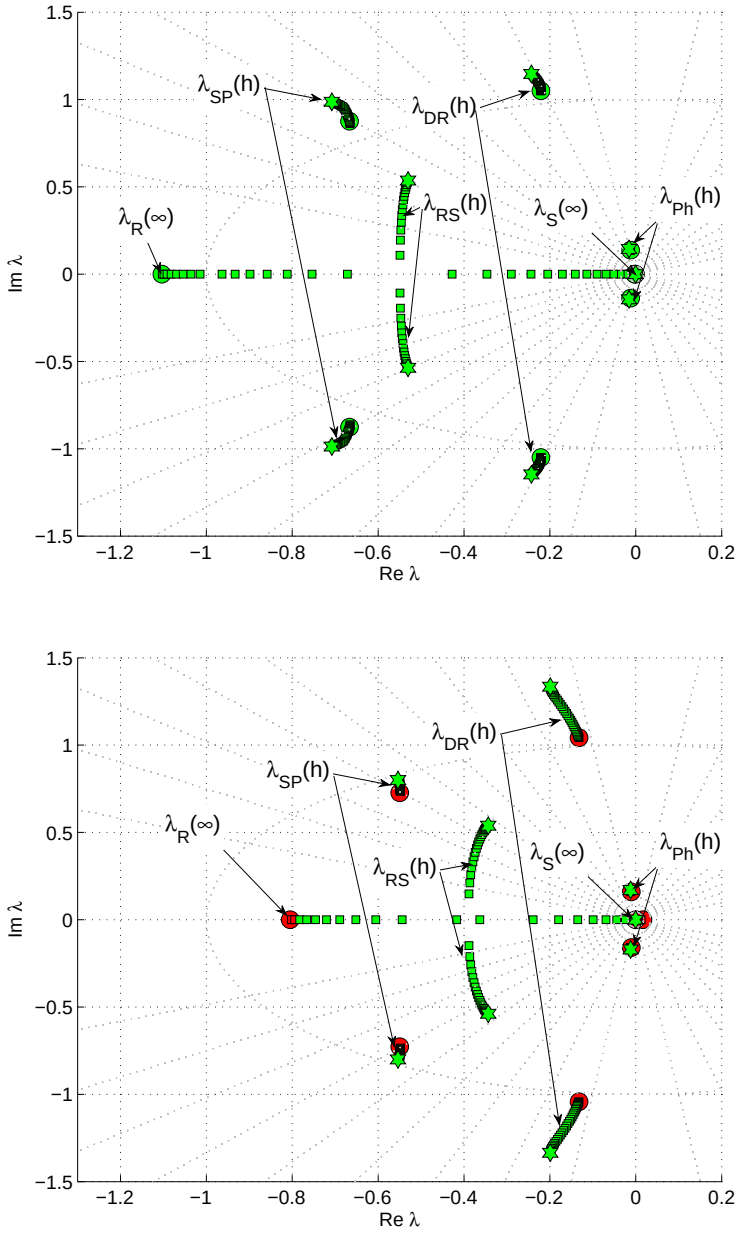

Fig. 6.24: Root-loci of eigenvalues of the longitudinal and lateral-directional dynamics modes at different altitudes above the runway $h = 4.0\bar{c}$, $h = 2.5\bar{c}$ and $h = 1.0\bar{c}$, top plot - $\alpha = 3°$ and bottom plot - $\alpha = 8°$.

Table 6.1: Eigenvalues of Longitudinal and Lateral-Directional Dynamics Modes at $\alpha = 8°$.

Ground Effect	**Short period (SP)**	**Phugoid (Ph)**	**Roll (R)**	**Spiral (S)**	**Dutch Roll (DR)**
$h(\infty)$	$0.549 \pm 0.742i$	$-0.012 \pm 0.17i$	-0.8	-0.008	$-0.133 \pm 1.048i$
$h = 0.5\bar{c}$	$-0.554 \pm 0.8i$	$-0.012 \pm 0.17i$	$-0.344 + 0.538i$	$-0.344 - 0.538i$	$-0.2 \pm 1.335i$

[a]Roll and Spiral modes are merged in oscillatory Roll-Spiral (RS) mode

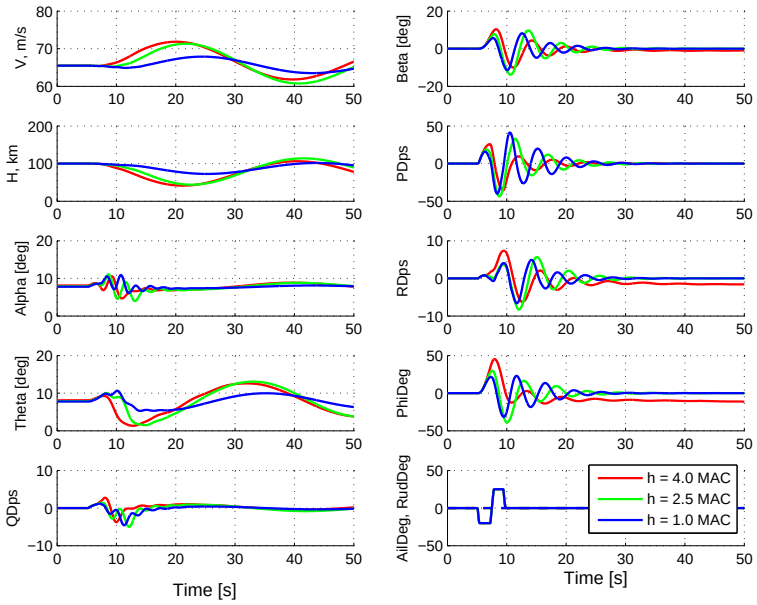

Fig. 6.25: Airplane responses to doublet aileron control input $\delta_a = \pm 25^0$ at different altitudes above the runway obtained in 6-DOF simulation.

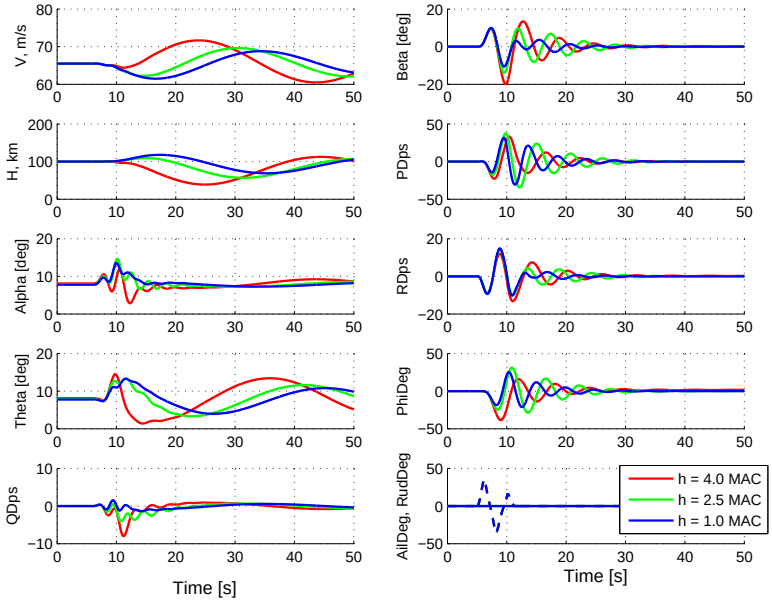

Fig. 6.26: Airplane responses to doublet rudder control input $\delta_r = \pm 35^0$ at different altitudes above the runway obtained in 6-DOF simulation.

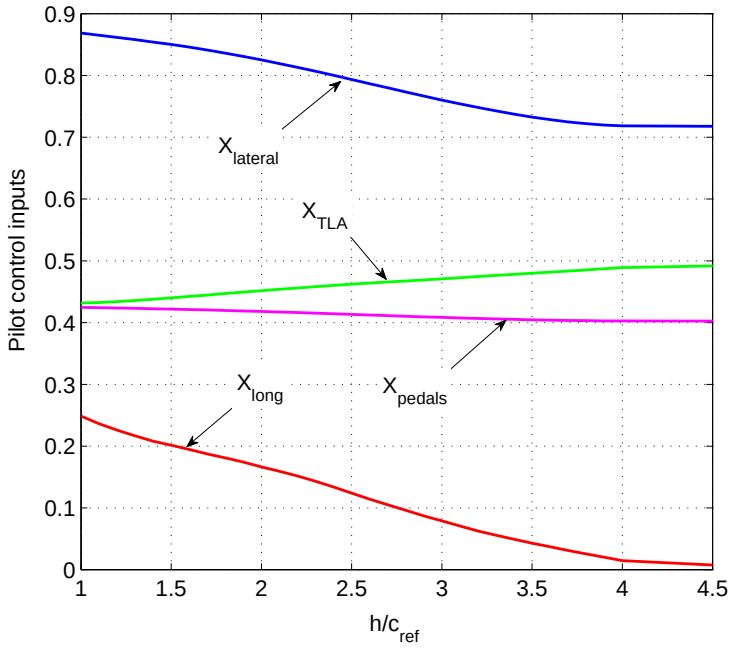

Fig. 6.27: Trim control inputs required in landing approach with nonzero sideslip and bank angles ($\alpha = 8°$, $\beta = 10°$, $\phi = 4°$).

A full flight simulation model of a typical transport aircraft has been modified taking into account the aerodynamic dependencies presented in the previous section for the 6-DOF flight simulations in a level trimmed flight in close proximity to the ground. The eigenvalues of the linearised equations of motion are presented in Fig. 6.24 with variation of parameter $\bar{h}$. The eigenvalues root-loci shows significant transformation of the lateral-directional modes of motion.

The roll subsidence and spiral eigenvalues in close proximity to the ground are merging creating the oscillatory Roll-Spiral mode with quite significant frequency $\omega_{RS} = 0.538 rad/s$ (see Fig.6.24(bottom plot $\alpha = 8°$)). Along with this change, the Dutch-roll eigenvalues increase frequency from the level of $\omega_D = 1.05 rad/s$ to $\omega_D = 1.34 rad/s$.

There is very little change in the short-period longitudinal eigenvalues, λ_{SP} and practically no change in the longitudinal phugoid mode, λ_{Ph}. In Table 6.1 the eigenvalues for the lateral-directional motion modes for flight at $h = \infty$ and $h = 1.0\bar{c}$ are presented for clarity showing a substantial transformation of the lateral-directional dynamics.

The new factor introduced in the performed eigenvalues analysis was the rolling and yawing moments depending on the airplane bank angle, which was equivalent to the "aerodynamic banking stiffness". This "aerodynamic stiffness" is strongly affecting the airplane controllability in close proximity to the ground. The air-

plane responses to aileron and rudder control inputs obtained in the 6-DOF flight simulation are shown in Figs.6.25 and 6.26, respectively. The airplane responses to pilot control inputs change in amplitudes and frequencies at low reduced altitudes $\bar{h} = h/\bar{c}$. This may lead to changes in handling qualities at low altitudes with effect on crosswind landing and onset of pilot induced oscillations.

In crosswind approach-and-landing the aircraft should fly with some nonzero sideslip angle to compensate side-wind. To fly a straight line along the runway the aircraft at the same time should have some non-zero side slip and bank angles. Fig.6.27 shows the required control pilot inputs in trim flight with steady side slip $\beta = 10°$, $\alpha = 8°$ and $\phi = 4°$. The control inputs are normalized with respect to maximum deflections. One can see that during landing significant re-trimming is required in the longitudinal and lateral control channels and thrust control, and less sensitivity is shown in the directional channel.

The presented dynamic analysis of the lateral-directional motion modes and controllability during approach-and-landing shows the importance of the ground effect for the improved realism of piloted simulation and estimation of critical crosswinds. The introduced aerodynamic modelling allows improved pilot training on various types of flight simulators.

Chapter 7

Concluding Remarks and Future Work

7.1 Summary of Research

For the purpose of adequate aerodynamic modelling in the extended flight envelope and in the close proximity to the ground, an in-depth understanding of separated flow physics along with reliable aerodynamic data must be acquired from both experiment and computations.

The major emphasis in this Thesis was made on:

1. Computational prediction of 2D aerodynamic static hysteresis in the stall region at low and moderately high Reynolds numbers.
2. Analysis of ice accretion effect on stall aerodynamics in order to formulate a simple phenomenological model for application in flight simulation.
3. Prediction of the aerodynamic forces, moments and stability of aircraft asymmetric attitudes in the close proximity to the ground.

The following conclusions summarize investigation of aerodynamic static hysteresis with bistable separated flow structures at high angle of attack using CFD methods:

- The bottom branch of static aerodynamic hysteresis represents fully separated flow with separation point placed on the leading edge of an airfoil. The flow on this branch is unsteady with periodical shedding of large vortices. The top branch of static aerodynamic hysteresis is formed by separated flow regimes with separation point on the upper surface changing its position with angle of attack.

- CFD simulations of the static aerodynamic hysteresis using the URANS formulation are very sensitive to the choice of turbulence model for closure, as each of the available models was proposed and parametrically tuned for specific flow conditions. One can't expect that a chosen model will work effectively for prediction of static aerodynamic hysteresis comprising various separated flow structures.

- Well established turbulence models, the Baldwin-Lomax (BL), Spalart-Allmaras (SA), Shear Stress Transport (SST), have been investigated and compared with objective of accurate prediction of the bottom branch in terms of its closeness to experimental data.

- The computational procedure was proposed to capture aerodynamic static hysteresis more systematically based on keeping memory from previous step's flow field parameters. It was noticed that the method of keeping pre-history of the flow parameters plays an important role in maintaining stability of the static hysteresis loops. It was shown that a more preferable method is to change the vector components of velocity in both forward and backward loop from previous flow field step, rather than rotating the grid to achieve the desired angle of attack.

- The SA turbulence model produced the best results. With no modifications, the existing SA model captures static aerodynamic hysteresis for the NACA 0018 airfoil at Re = 300,000 and Re = 700,000 reasonably well. To improve accuracy and reach a better match with experimental data, the turbulent diffusion coefficient, σ_t, in the SA model was modified within justifiable limits, which gave positive outcome.

- The proposed modification of the Baldwin-Lomax model eliminates the difficulties of divergence and instability of the original BL model at high angles of attack. This allows the modified BL model to be used initially for prediction of static aerodynamic hysteresis phenomenon due to its simplicity and cost effectiveness.

- Predictions of the aerodynamic loads for the TsAGI-9140 airfoil at moderately high Reynolds number of 5 millions demonstrated existence of aerodynamic static hysteresis loops similar to the experimental results. The obtained simulation results show that bistable separated flow regimes can be computationally captured at moderately high Reynolds number flow conditions.

The effect of ice accretion on stall aerodynamics has been addressed and the following conclusions can be made:

- The horn, rime or glaze shaped ice causes a drop in the maximum lift coefficient and leads to earlier stall.

- The simulation results show that the horn shaped ice causes most degradation of the aerodynamic performance of an airfoil, namely the reduction in the lift force slope.

- A simple phenomenological model for application in flight simulations was proposed to evaluate the effect of ice accretion on aerodynamic characteristics.

Aerodynamic forces and moments acting on an airplane in the close proximity to the ground has been investigated using CFD simulations at various attitude angles (θ, ϕ) with the following conclusions:

- Large amplitude oscillations of the NACA 4412 airfoil with and without flap deflection covering the stall region revealed significant dynamic hysteresis loops with averaged values of the lift coefficient which were strongly affected by flap deflection and the closeness to the ground.
- The Common Research Model (CRM) aircraft configuration with a bank angle in close proximity to the ground generates significant rolling and yawing moments which should be considered in flight simulation.
- The performed analysis shows that the lateral-directional modes of motion are significantly transformed via merging the roll-subsidence and spiral eigenvalues, which forms the second oscillatory roll-spiral mode with potential to affect the pilot handling qualities in landing with cross wind conditions.

7.2 Future Work

The conducted research in investigation of static aerodynamic hysteresis needs to be extended to address prediction of bistable separated flow structures in three dimensional space with additional inclusion of ice accretion shapes. The ground effect aerodynamics should be further investigated considering representative high lift aircraft configurations with estimation of unsteady aerodynamic derivatives. The future research scope can be summarized as follows:

- Testing transitional turbulence models such as k-kl-ω to improve prediction of the top branch of static hysteresis.
- Investigation of static aerodynamic hysteresis using finite aspect ratio NACA 0018 and TsAGI 9140 wings using URANS, Detached or Large Eddy Simulations.
- Tuning of eddy viscosity turbulence model parameters such as diffusion and dissipation coefficients for post stall regime with fully separated flow conditions.
- Investigate effect of compressibility, intensity of incoming flow turbulence and aircraft model vibration on prediction of static aerodynamic hysteresis.
- Analysis of the ground effect aerodynamics using the high lift configuration DLR-F11 with additional inclusion of unsteady aerodynamic derivatives and cross-wind conditions.
- Expand research in ice accretion aerodynamics considering asymmetric ice distribution and search for bistable separated flow structures using the Common Research Model (CRM).

7.3 Contributions

- The numerical simulation and capture of aerodynamic static hysteresis phenomena is a complicated phenomena which lacks attentions and research. In this thesis, the framework of capturing static hysteresis, it's sensitivity to computational setup and turbulence models have been brought forward.

- Several source codes have been developed in the open source CFD code OpenFOAM which can be used to capture static hysteresis in static and slow dynamic movement methods so that other researchers can benefit from testing these source codes in OpenFOAM. This includes the source code for fixed angle of attack change solver, prescribed alpha change solver, hystersisFoam and GMRES/BicG stable matrix solver(refer to Chapter 3 for more details).

- The analysis of TsAGi-9140 airfoil at high Reynolds number of 5 million proves that static stall hysteresis is very different to laminar bubble associated hysteresis, thus proving that static hysteresis is not limited to laminar bubble existence, omitting the common misinterpretation that aerodynamic static hysteresis can only exist as low Reynolds numbers.

- Two phenomenological models have been brought forward (both derived from the original Goman-Khrabrov, i.e. G-K model) which can be used to identify aerodynamic parameters in static stall hysteresis and in the case of ice-accretion.

- The data generated in Ground Effect Aerodynamics (in Chapter 6) was used to develop flight simulation model for the AMST flight simulator which proved to be working very well according to pilot reviews.

Bibliography

[1] Boeing. Statistical summary of commercial jet airplane accidents. world wide operations 1959-2015.

[2] Flight Safety Foundation. Approach-and-landing accident reduction (alar) briefing note: 8.7 - crosswind landing, 2000.

[3] Alexander N Khrabrov BI Soemarwoto NB Abramov, MG Goman. Aerodynamic modeling for poststall flight simulation of a transport airplane. *Journal of Aircraft*, http://dx.doi.org/10.2514/1.C034790:1–14, 2019.

[4] Sanjay Mittal and Priyank Saxena. Hysteresis in flow past a naca 0012 airfoi. *Computational Methods in Applied Mechanical Engineering*, 191:2179–2189, 2002.

[5] OpenFOAM. The open source computational fuid dynamics toolbox. http://www.openfoam.com/, (last accessed 8 June 2017).

[6] David G. Hull. *Fundamentals of Airplane Flight Mechanics*. Springer, 2007.

[7] Roberto A. Bunge. *Aircraft Flight Dynamics*. Stanford University, 2015.

[8] J.H. Ferziger and M.Peric. *Computational Methods for Fluid Dynamics, 3rd Edition*. Springer, 2002.

[9] https://www.phy.ornl.gov/csep/pde/node3.html. Classification of linear pdes in two independent variables. online, (last accessed 1 March 2018).

[10] http://how.gi.alaska.edu/ao/sim/chapters/chap3.pdf. Classification of pde and related properties. online, (last accessed 1 March 2018).

[11] Abdusamad A.Salih. Finite element method. online, (last accessed 3 March 2018).

[12] NASA. https://turbmodels.larc.nasa.gov/index.html, 2018.

[13] Smith A.M.O. and Cebeci.T. Numerical solution of the turbulent boundary layer equations. Dac 33735, Douglas Aircraft Division, 1967.

[14] Barbara Sakowski, Douglas Darling, Robert L. Roach, and Allan van de Wall. Evaluation and application of the baldwin-lomax turbulence model in two-dimensional, unsteady, compressible boundary layers with and without separation in engine inlets, https://ntrs.nasa.gov/archive/nasa/casi.ntrs.nasa.gov/19930000899.pdf, (last accessed 11 Dec 2017).

[15] Spalart P. R. and Allmaras S. R. A one-equation turbulence model for aerodynamic flows. Technical Report No. 1, pp. 5-21, Recherche Aerospatiale, 1994.

[16] Chien K.-Y. Predictions of channel and boundary-layer flows with a low-reynolds-number turbulence model. 20(1):33–38, 1982.

[17] Menter F. R. Improved two-equation k-ω turbulence models for aerodynamic flows. TM 103975, NACA, October 1992.

[18] B.Caruelle and F.Ducros. Detached-eddy simulations of attached and detached boundary layers. *International Journal of Computational Fluid Dynamics*, 17(6):433–451, December 2003.

[19] Spalart P. R., Jou W-H., Strelets M., and Allmaras S. R. comments on the feasibility of les for wings and on a hybrid rans/les approach. pages 4–8, 1997.

[20] Hrvoje Jasak. Error analysis and estimation for the finite volume method with application to fluid flows.

[21] Dmitry Ignatyev and Alexander Khrabrov. Experimental study and neural network modeling of aerodynamic characteristics of canard aircraft at high angles of attack. *aerospace*, 2018.

[22] Argyris G. Panaras. Turbulence modeling of flows with extensive crossflow separation. *Aerospace*, 2:461–481, 2015.

[23] Marco Baragona. Unsteady charecteristics of laminar separation bubbles.

[24] G.P.Svischev. Investigation of a low drag airfoil with different leading edge modifications for increase of maximum lift force. Technical report, TsAGI's Proceedings, 1946.

[25] Thomas J. M. The influence of laminar separation bubble on low reynolds number airfoil hysteresis. *Wind Engineering*, 22(9), September 1985.

[26] Zifeng Yang, Hirofumi Igarashi, Mathew Martin, and Hui Hu. An experimental investigation on aerodynamic hysteresis of a low-reynolds number airfoil. Aiaa-2008-0315, 46th AIAA Aerospace Sciences Meeting and Exhibit, Jan 7-10, 2008, Reno, Nevada, 2009.

[27] W. A. Timmer. Two-dimensional low-reynolds number wind tunnel results for airfoil naca 0018. *Wind Engineering*, 32(6):525–537, 2008.

[28] Jon A. H. Effects of freestream turbulence on the performance characteristics of an airfoil. *AIAA Journal*, 29(9), 1991.

[29] M. Mizoguchi, Y. Kajikawa, and H. Itoh. Static stall hysteresis of low-aspect-ratio wings. http://dx.doi.org/10.2514.6.2014-2014, 32nd AIAA Applied Aerodynamics Conference, AIAA AVIATION FORUM, AIAA Paper, 2014.

[30] J.F. Marchman III, V. Sumantran, and C.G Schafer. Acoustic and turbulence influences on stall hystersis. *AIAA Journal*, 50.

[31] Rahman M .R, A. T. Hasan, and M. I. Labib. Numerical investigation of aerodynamic hysteresis for transonic flow over a supercrticial airfoil. *Procedia Engineering*, 105:368–374, 2015.

[32] Lance W. T. Semi-empirical prediction of airfoil hysteresis. *aerospace*, 2016.

[33] Dirk M.Luchtenburg, Clarence W. Rowley, Mark W. Lohry, Luigi Martienelli, and Robert F. Stengel. Identification of unsteady aerodynamic models for a generic wide-body aircraft at high angles of attack. *Journal of Aircraft*, 2014.

[34] Mohdi Goreyshir and Russel M. Cummings. Challenges in the aerodynamic modelling of an oscillating and translating airfoil at large incidence angles. *Aerospace Science and Technology*, 28:176–190, 2013.

[35] David R. Williams, Florian Reisner, David Greenblatt, and Christoph Strangfeld. Hanns Muller-Vahl. Modeling lift hysteresis with a modified goman-khrabrov model on pitching airfoils. Aiaa-2015-2631, 45th AIAA Fluid Dynamics Conference, June 2015.

[36] Shengyi Wang, Derek B. Ingham, Lin Ma, Mohamed Pourkashanian, and Zhi Tao. Numerical investigations on dynamic stall of low reynolds number flow around oscillating airfoils. *Computers and Fluids*, 39(9):1529–1541, 2010.

[37] Leon O.Chua and Keith.A.Stromsmoe. Mathematical model for dynamic hysteresis loops. *International Journal of Engineering Science*, 9(5):435–450, 1971.

[38] N. D. Ham. Aerodynamic loading on a two-dimensional airfoil during dynamic stall. *AIAA*, 6(10):1927–1934, 1968.

[39] Jei Wu, Chang Shu, Ning Zhao, and Weiwei Yan. Fluid dynamics of flapping wing insect in ground effect. *Joural if Bionic Engineering*, 11:52–60, 2014.

[40] Jei Wu, , and Ning Zhao. Ground effect on flapping wing. *Procedia Engineering*, 67:295–302, 2013.

[41] Thomas L, Norizham A R, and Grigioris D. Vortex lattice simulations of attached and separated flows around flapping wings. *aerospace*, 2017.

[42] N. B. Abramov, M.G. Goman, A Khrabrov, and B.I. Soemarwoto. Aerodynamic modeling for post-stall flight simulation of a transport airplane. *Journal of Aircraft*, 2018.

[43] M.Sereez, N.B.Abramov, M.G.Goman, and A. Khrabrov. Computational simulation of stall aerodynamics at low reynolds number. Conference paper, Applied Aerodynamics Conference, July 2016.

[44] M Goman and A Khrabrov. State-space representation of aerodynamic characteristics of an aircraft at high angles of attack. *Journal of Aircraft*, 31(5): 1109–1115, 1983.

[45] N. B. Abramov, M. G. Goman, A. N. Khrabrov, and K. A. Kolinko. Simple wings unsteady aerodynamics at high angles of attack: Experimental and modelling results. Conference paper, AIAA-99-4013, 1999.

[46] G.P.Svischev. Investigation of a low drag airfoil with different leading edge modifications for increase of maximum lift force. Technical report, TsAGI's Proceedings, 1946.

[47] Z.Gong, S.A.Estrada, M.H.Lowenberg, S.A. Neild, and M.G. Goman. Experimental investigation of aerodynamic hysteresis using a 5-dof wind tunnel manoeuvre rig. *Journal of Aircraft*, 2018.

[48] Fries T.P. and Matthies H.G. A review of petrov - galerkin stabilization approaches and an extension to meshfree methods. http://citeseerx.ist.psu.edu, 2004.

[49] Brooks A.N., Hughes, and T.J.R. Streamline-upwind-petrov-galerkin formulations for convection dominated flows with particular emphasis on the incompressible navier-stokes equations. *Computational Methods in Applied Mech. Engineering*, 32:199–259, 1982.

[50] Harry J. G and Kenneth B. Tests of n.a.c.a. 0009, 0012, and 0018 airfoils in the full-scale tunnel. Technical report, N.A.C.A. Report No. 647, 1938.

[51] Menter F. R. Zonal two equation k-ω turbulence models for aerodynamic flows. Conference paper, AIAA, 1993.

[52] Pasquale D.Di, , Roma A., and Garett S.J. A selective review of cfd transition models. conference, 39th AIAA Fluid Dynamics Conference, June 2009.

[53] Patankar S.V and Spalding D.B. A calculation procedure for heat, mass and momentum transfer in three dimensional parabolic flows. *IInternational Journal of heat and mass transfer*, 15(10):1787–1806, October 1972.

[54] B.S. Baldwin and H. Lomax. Thin layer approximation and algebraic model for separated turbulent flows. Conference paper, 16th AIAA Aerospace Meeting, 1978.

[55] M.Sereez, N.B.Abramov, and M.G.Goman. Computational ground effect aerodynamics and airplane stability analysis during take-off and landing. Eucass conference paper, 7th European Conference for Aeronautics and Space sciences, July 2017.

[56] Masoud Mirzaei, Mohammad A. Ardekani, and Mehdi Doosttalab. Numerical and experimental study of flow field characteristics of an iced airfoil. *Journal of Aerospace and Technology*, 13:267–276, 2009.

[57] Harold E.Addy Jr. Ice accretions and icing effects for modern airfoils.

[58] Andy P. Broeren, Sam Lee, Gautam H. Shah, and Patrick C. Murphy. Aerodynamic effects of simulated ice accretion n a generic transport. 2012.

[59] http://web.mit.edu/drela/Public/web/xfoil/. Xfoil, (last accessed 2 June 2017).

[60] http://www.ansys.com/products/fluids/ansys-fluent, (last accessed 8 June 2017).

[61] Jian Ming Liu. The study on adaptive cartesian grid methods for compressible flow and their applications.

[62] Erjie Cui and Xin Zhang. Ground effect aerodynamics. In *Encyclopedia of Aerospace Engineering*, pages 245–256, 2010.

[63] Meredith C.W.Evans. Ground effect testing capabilities in the Filton $12' \times 10'$ low speed wind tunnel. *22nd International Congress of the Aeronautical Sciences, Harrogate, UK*, Paper ICAS-373, 27 Aug - 1 Sept 2000.

[64] R.W.Staufenbiel and U.-J.Schlichting. Stability of airplanes in ground effect. *Journal of Aircraft*, 25(4):289–294, April 1988.

[65] X. Zhang and J. Zerihan. Edge vortices of a double-element wing in ground effect. *Journal of Aircraft*, 41:1127–1137, 2004.

[66] Shaowei Li, Danjie Zhou, Yuanjing Zhang, and Qiulin Qu. Aerodynamic investigation of rae2822 airfoil in ground effect. *Procedia Engineering*, 126: 174–178, 2015.

[67] Qing Jia, Wei Yang, and Zhigang Yang. Numerical study on aerodynamics of a banked wing in ground effect. *Int J. Naval Architecture and Ocean Engineering*, 8:209–217, 2016.

[68] G. Doig. Transonic and supersonic ground effect aerodynamics. *Procedia Engineering*, 69:1–282, 2014.

[69] Amin Mivehchi, Jason Dahl, and Stephen Licht. Heaving and pitching oscillating foil propulsion in ground effect. *Journal of Fluids and Structures*, 63: 174–187, 2016.

[70] https://aiaa-dpw.larc.nasa.gov/Workshop5/DPW5 geom.html, (last accessed 8 June 2017).

[71] https://commonresearchmodel.larc.nasa.gov/geometry/vertical-tail geometry, (last accessed 8 June 2017).

[72] 2nd AIAA CFD High Lift Prediction Workshop. https://hiliftpw.larc.nasa.gov/workshop2, (last accessed 20 Nov 2017).

[73] OpenVSP sofware and Hangar. http://hangar.openvsp.org/ or http://openvsp.org/, (last accessed 22 Nov 2017).

Chapter 8

Appendix

8.1 Source codes that are frequently used in OpenFOAM

laplacianFoam directory contents of solver
solvers/basic/LaplacianFoam
- Make
- createFields.H
- laplacianFoam.C
- write.H

a) **Make Directory**
The make directory includes the compiling instructions such as libraries to which the solver is linked to, name of the solver and directory to place it.
laplacianFoam.C

```
1) Make\files
EXE = $(FOAM_APPBIN)/laplacianFoam


2) Make\options
EXE_INC = \
-I$(LIB_SRC)/finiteVolume/lnInclude \
-I$(LIB_SRC)/meshTools/lnInclude
{\tiny
EXE_LIBS = \
-lfiniteVolume \
-lmeshTools
```

The first part 1) make/files says the name off the application (laplacianFoam) and where the solver is going to be compiled to (FOAM APPBIN = Open FOAM's application bin).

The second part 2) make/options instructs the compiler to include two libraries in the linking procedure namely the finite Volume and the mesh tools

libraries.

b) **createFields.H** createFields.H is used to create the objects/fields necessary to be read, evaluated and written at the end of simulation. In laplacianFoam a volume field (with boundary patches) is written for Temperature(T), a transport properties field (for kinematic visosity and density inclusion/specification) and another scalar value for diffusivity (DT) is created in the createFields file. This file can be modified to specify any other fields to be manipulated at the time of simulation.

```
Info<< "Reading field T\n" << endl;{\tiny

volScalarField T
(
IOobject
(
"T",
runTime.timeName(),
mesh,
IOobject::MUST_READ,
IOobject::AUTO_WRITE
),
mesh
);


Info<< "Reading transportProperties\n" << endl;

IOdictionary transportProperties
(
IOobject
(
"transportProperties",
runTime.constant(),
mesh,
IOobject::MUST_READ_IF_MODIFIED,
IOobject::NO_WRITE
)
);


Info<< "Reading diffusivity DT\n" << endl;

dimensionedScalar DT
```

```
(
transportProperties.lookup("DT")
);
```

c) **laplacianFoam.C** laplacianFoam.C is the main source file in this solver. It instructs the solver to solve an equation for the derivative of time ddt(T) and the laplacian evaluation of Diffusivity and Temperature i.e. laplacian (DT,T). At the end of solving the equation the output is written using the header file write.H.

```
#include "fvCFD.H"
#include "simpleControl.H"



int main(int argc, char *argv[])
{
#include "setRootCase.H"

#include "createTime.H"
#include "createMesh.H"

simpleControl simple(mesh);

#include "createFields.H"


Info<< "\nCalculating temperature distribution\n" << endl;

while (simple.loop())
{
Info<< "Time = " << runTime.timeName() << nl << endl;

while (simple.correctNonOrthogonal())
{
solve
(
fvm::ddt(T) - fvm::laplacian(DT, T)
);
}

#include "write.H"

Info<< "ExecutionTime = " << runTime.elapsedCpuTime() << " s"
<< "  ClockTime = " << runTime.elapsedClockTime() << " s"
<< nl << endl;
}
```

```
Info<< "End\n" << endl;

return 0;
}
```

d) **write.H** write. H file indicates to the application to write the gradient of temperature grad(T) as an output along with Grad(Tx), Grad(Ty) and Grad (Tz) i.e. the gradient of temperature in every direction.

```
if (runTime.writeTime())
{
volVectorField gradT(fvc::grad(T));

volScalarField gradTx
(
IOobject
(
"gradTx",
runTime.timeName(),
mesh,
IOobject::NO_READ,
IOobject::AUTO_WRITE
),
gradT.component(vector::X)
);

volScalarField gradTy
(
IOobject
(
"gradTy",
runTime.timeName(),
mesh,
IOobject::NO_READ,
IOobject::AUTO_WRITE
),
gradT.component(vector::Y)
);

volScalarField gradTz
(
IOobject
(
"gradTz",
runTime.timeName(),
mesh,
IOobject::NO_READ,
```

```
IOobject::AUTO_WRITE
),
gradT.component(vector::Z)
);


runTime.write();
}
```

scalarTransportFoam The scalarTransportFoam is another basic solver which solves the PDE systems for the transport of a scalar variable with respect to time.*fvm::ddt(T)* indicates to take the time derivative of Temperature(T) *fvm::laplacian(DT,T)* indidcates to take the laplacian of Diffusivity(DT) and Temperature(T). Teqn.relax() is used to under-relax the equation so that the solution is stable in time marching.

```
Application
scalarTransportFoam
Description
Solves the steady or transient transport equation for a passive scalar.

#include "fvCFD.H"
#include "fvOptions.H"
#include "simpleControl.H"



int main(int argc, char *argv[])
{
#include "setRootCase.H"
#include "createTime.H"
#include "createMesh.H"

simpleControl simple(mesh);

#include "createFields.H"
#include "createFvOptions.H"


Info<< "\nCalculating scalar transport\n" << endl;

#include "CourantNo.H"

while (simple.loop())
{
Info<< "Time = " << runTime.timeName() << nl << endl;
```

```
while (simple.correctNonOrthogonal())
{
fvScalarMatrix TEqn
(
fvm::ddt(T)
+ fvm::div(phi, T)
- fvm::laplacian(DT, T)
==
fvOptions(T)
);

TEqn.relax();
fvOptions.constrain(TEqn);
TEqn.solve();
fvOptions.correct(T);
}

runTime.write();
}

Info<< "End\n" << endl;

return 0;
}
```

simpleFoam simpleFoam is the solver used in OpenFOAM for analysis of incompressible navier stokes equations with turbulence effects.

it consists of 3 files simpleFoam.C , uEqn.H and pEqn.H. The solver is based on the SIMPLE(Semi - Implicit Pressure linked Equations) algorithm. The concept is briefly summarised below.

1) Velocity Equation is built by taking the Divergence of Velocity Fluxes at Cell Centers (Fluxes are referred as "phi" in OpenFOAM) and the effect of Divergence of Deviatoric turbulent Reynold Stresses on Velocity is added.

2) The Velocity Equation is solved against the pressure gradient from previous time step or against the guessed pressure if the simulation started from time zero.

3) Velocity is under-relaxed to improve stability of solution.

4) The velocity Equation in Matrix form can be broken down into it's diagonal and off- diagonal components. The terms involving diagonal elements are stored in uEqn.A() and the terms involving off-diagonal elements are stored in uEqn.H(). The inverse of uEqn.A() is denoted as rAU. The product of uEqn.H() and rAU is denoted as H/A or HbyA. The flux of HbyA is then "phiHbyA".

5) The Pressure Equation is constructed which relates that the Lapacian of (rAU) and pressure that is equal to the divergence of phiHbyA. The equation gets solved to find pressure p.

6) The flux is corrected by subtracting the flux from pressure Equation.

7) The pressure is under relaxed to improve convergence and stability.

8) The velocity is corrected by subtracting the product of rAU and gradient of pressure from H/A or HbyA.

9) The next iteration starts and 1-8 is repeated. *simpleFoam.C*

```
while (simple.loop())
{
Info<< "Time = " << runTime.timeName() << nl << endl;

// --- Pressure-velocity SIMPLE corrector
{
#include "UEqn.H"
#include "pEqn.H"
}

laminarTransport.correct();
turbulence->correct();
```

UEqn.H

```
// Momentum predictor

MRF.correctBoundaryVelocity(U);

tmp<fvVectorMatrix> tUEqn
(
fvm::div(phi, U)
+ MRF.DDt(U)
+ turbulence->divDevReff(U)
==
fvOptions(U)
);
fvVectorMatrix& UEqn = tUEqn.ref();

UEqn.relax();

fvOptions.constrain(UEqn);

if (simple.momentumPredictor())
{
solve(UEqn == -fvc::grad(p));

fvOptions.correct(U);
}
```

pEqn.H

```
{
volScalarField rAU(1.0/UEqn.A());
volVectorField HbyA(constrainHbyA(rAU*UEqn.H(), U, p));
```

```
surfaceScalarField phiHbyA("phiHbyA", fvc::flux(HbyA));
MRF.makeRelative(phiHbyA);
adjustPhi(phiHbyA, U, p);

tmp<volScalarField> rAtU(rAU);

if (simple.consistent())
{
rAtU = 1.0/(1.0/rAU - UEqn.H1());
phiHbyA +=
fvc::interpolate(rAtU() - rAU)*fvc::snGrad(p)*mesh.magSf();
HbyA -= (rAU - rAtU())*fvc::grad(p);
}

tUEqn.clear();

// Update the pressure BCs to ensure flux consistency
constrainPressure(p, U, phiHbyA, rAtU(), MRF);

// Non-orthogonal pressure corrector loop
while (simple.correctNonOrthogonal())
{
fvScalarMatrix pEqn
(
fvm::laplacian(rAtU(), p) == fvc::div(phiHbyA)
);

pEqn.setReference(pRefCell, pRefValue);

pEqn.solve();

if (simple.finalNonOrthogonalIter())
{
phi = phiHbyA - pEqn.flux();
}
}

#include "continuityErrs.H"

// Explicitly relax pressure for momentum corrector
p.relax();
// Momentum corrector
U = HbyA - rAtU()*fvc::grad(p);
U.correctBoundaryConditions();
fvOptions.correct(U);
```